Indirect NMR detection via proton of nuclei subject to large anisotropic interactions, such as 14N, 195Pt, and 35Cl, using the T-HMQC sequence

Racha Bayzou, Julien Trebosc, Ivan Hung, Zhehong Gan, Olivier Lafon, Jean-Paul Amoureux

To cite this version:

Racha Bayzou, Julien Trebosc, Ivan Hung, Zhehong Gan, Olivier Lafon, et al.. Indirect NMR detection via proton of nuclei subject to large anisotropic interactions, such as 14N, 195Pt, and 35Cl, using the T-HMQC sequence. The Journal of Chemical Physics, 2022, 156 (6), pp.064202. 10.1063/5.0082700 . hal-04138261

HAL Id: hal-04138261
https://hal.univ-lille.fr/hal-04138261v1

Submitted on 22 Jun 2023

HAL is a multi-disciplinary open access archive for the deposit and dissemination of scientific research documents, whether they are published or not. The documents may come from teaching and research institutions in France or abroad, or from public or private research centers.

L'archive ouverte pluridisciplinaire **HAL**, est destinée au dépôt et à la diffusion de documents scientifiques de niveau recherche, publiés ou non, émanant des établissements d'enseignement et de recherche français ou étrangers, des laboratoires publics ou privés.

Indirect NMR detection via proton of nuclei subject to large anisotropic interactions, such as ^{14}N, ^{195}Pt and ^{35}Cl, using the T-HMQC sequence

Racha Bayzou,[1] Julien Trébosc,[1,2] Ivan Hung,[3] Zhehong Gan,[3] Olivier Lafon,[1,*] Jean-Paul Amoureux,[1,4,5,*]

[1] Univ. Lille, CNRS, Centrale Lille, Univ. Artois, UMR 8181 – UCCS – Unité de Catalyse et Chimie du Solide, 59000 Lille, France.
[2] Univ. Lille, CNRS, INRAE, Centrale Lille, Univ. Artois, FR 2638 – IMEC – Fédération Chevreul, 59000 Lille, France.
[3] National High Magnetic Field Laboratory, 1800 East Paul Dirac Drive, Tallahassee, Florida, 32310, USA.
[4] Riken NMR Science and Development Division, Yokohama-shi, 230-0045 Kanagawa, Japan.
[5] Bruker Biospin, 34 rue de l'industrie, 67166 Wissembourg, France.

Corresponding authors. Olivier Lafon olivier.lafon@univ-lille.fr
Jean-Paul Amoureux jean-paul.amoureux@univ-lille.fr

Abstract. Recently, the T-HMQC sequence using the TRAPDOR (transfer of population in double resonance) recoupling has been introduced for the indirect proton detection of quadrupolar nuclei with spin $I = 1$ (^{14}N) or 3/2 (^{35}Cl) in solids at fast MAS. The sequence is simple as it only uses four rectangular pulses, and exhibits low t_1-noise because the recoupling pulses are applied to the indirectly detected isotope, I. We demonstrate that this sequence is applicable for the proton detection of spin-1/2 nuclei subject to large chemical shift anisotropy (CSA), such as ^{195}Pt. We also report the proton detection of double-quantum (2Q) coherences of ^{14}N nuclei using this sequence. This 2Q version is more robust to the adjustment of the magic angle and the instabilities of the MAS frequencies than its parent single-quantum (1Q) version since the 2Q coherences are not broadened by the first-order quadrupole interaction. In practice, compared to the T-HMQC 1Q sequence applied to ^{14}N nuclei, the 2Q variant benefits from a slightly higher resolution and comparable sensitivity. In this article, we derive for the first time the Hamiltonian that describes the spin dynamics during the TRAPDOR recoupling. This Hamiltonian demonstrates the importance of the adiabaticity parameter as well as the role of third-order terms in the effective Hamiltonian. The effects of offsets, radio-frequency field and recoupling time on the efficiency of the T-HMQC sequence are analyzed numerically as well as with experimental proton detection of ^{195}Pt nuclei in a mixture of cis- and transplatin and that of ^{14}N and ^{35}Cl isotopes in L-histidine·HCl.

I. Introduction

Solid-state nuclear magnetic resonance (NMR) provides unique insights into the atomic-level structure and dynamics of solids, including membrane proteins, pharmaceuticals and advanced materials [1]. However, NMR spectra of some isotopes in solids can feature broad powder patterns with breadths ranging from hundreds of kilohertz to tens of megahertz [2,3]. For instance, the NMR spectra of paramagnetic or conductive solids are broadened by the hyperfine interactions between unpaired or conduction electrons and nuclei [4]. In addition, over 74% of the NMR-active isotopes have a spin quantum number $I \geq 1$ and are subject to the quadrupole interactions, which widen their powder spectra, often over several megahertz [5]. Furthermore, the electron cloud of spin-1/2 nuclei with high atomic numbers, such as ^{119}Sn, ^{195}Pt, ^{199}Hg or ^{207}Pb, are highly anisotropic, which lead to wide powder patterns broadened by large chemical shift anisotropy (CSA) [3].

These isotopes subject to large anisotropic NMR interactions have been first analyzed with direct detection, *i.e.* their signals were recorded during the acquisition period. However, the direct detection of wide spectra is plagued by several difficulties, such as the experimental dead time. For these isotopes, a major challenge is the lack of sensitivity since these large anisotropic interactions spread the total integrated intensity over a broad spectral width. Several techniques have been proposed to enhance the sensitivity of wide spectra, including (i) the acquisition of multiple echoes using the CPMG (Carr-Purcell Meiboom-Gill) sequence or its variant for half-integer spin quadrupolar nuclei, called QCPMG (quadrupolar CPMG) [6–8], (ii) the transfer of polarization from protons to the detected isotope using broadband cross-polarization (CP) [3,9,10], which can be combined with dynamic nuclear polarization (DNP) in order to enhance further the sensitivity [11,12], and (iii) for half-integer spin quadrupolar nuclei, the irradiation of the satellite transitions (STs) in order to enhance the signal of the central transition (CT) between energy levels $m_I = \pm 1/2$ [13]. The excitation bandwidth of (Q)CPMG and CP can be improved by the use of adiabatic pulses [9,10,14–16]. Another difficulty is that the breadth of the NMR spectrum can exceed the detection bandwidth of the probe or the excitation bandwidth of the radio-frequency (rf) pulse, thus requiring a piecewise acquisition called VOCS (variable offset cumulative spectrum) [17].

More recently, the indirect detection of wide spectra via one spin-1/2 nucleus, such as ^{1}H or ^{13}C, has been proposed. In these experiments, the frequencies of the isotope subject to large anisotropic interactions are encoded during the indirect evolution period, t_1. This approach has been first demonstrated for the observation of ^{14}N nuclei in solids [18–20]. This nitrogen isotope is the most abundant with a natural abundance $NA = 99.64\%$. However, because of its integer spin value, $I = 1$, all its single-quantum (1Q) transitions are broadened by the first-order quadrupole interaction (H_{Q1}), and ^{14}N powder patterns with a width of up to 10.5 MHz have been reported [21]. ^{14}N 1Q or double-quantum (2Q) coherences can be indirectly detected using two-dimensional (2D) hetero-nuclear correlation (HETCOR) sequences, such as HMQC or HSQC (hetero-nuclear multiple- or single-quantum coherence), with coherence transfers mediated by either residual dipolar splitting, which is the sum of J-coupling and second-order quadrupole–dipole cross-terms) [18–20,22,23], or dipolar interactions [24,25]. In the latter approach, called D-HMQC or D-HSQC, the dipolar interactions between the spy spins and the ^{14}N isotope are reintroduced under magic-angle spinning (MAS) by applying a hetero-nuclear dipolar recoupling sequence to the spy spins. In the case of proton detection, denoted ^{1}H-{^{14}N} hereafter, ^{1}H-^{14}N dipolar couplings are generally reintroduced by applying the symmetry-based SR4_1^2 recoupling, which also suppresses the contribution of ^{1}H-^{1}H dipolar interactions to the first-order average Hamiltonian and offers tolerance to rf inhomogeneity [26]. The HMQC sequence is more sensitive than the HSQC one [23,27]. The indirect detection of ^{14}N 1Q coherences requires a very stable spinning precisely at the magic angle, $\beta_{\text{RL}} \approx 54.736°$, in order to average out H_{Q1}. Conversely, the ^{14}N 2Q coherences between energy levels $m_I = \pm 1$ are not broadened by H_{Q1} and hence, their indirect detection does not require a precise adjustment and a high stability of the magic angle and the spinning frequency, ν_{R} [18]. Nevertheless, the indirect detection of ^{14}N 2Q coherences is usually less efficient than that of 1Q ones [25,28–30].

A challenge for the indirect detection of ^{14}N nuclei using HMQC or HSQC sequences is that the ^{14}N rf-amplitude is limited to a few tens of kilohertz, which is two orders of magnitude lower than the ^{14}N H_{Q1} interaction. Various schemes applied at the ^{14}N Larmor frequency have been proposed for the excitation and the reconversion of ^{14}N 1Q and 2Q coherences. They include hard pulses using high rf-power [19], sideband selective long pulses (SLP) [20,28], trains of short rotor-synchronized DANTE (delays alternating with nutation for tailored excitation) pulses [31,32], or low-power rotor-synchronized symmetry-based sequences, including XiX (X inverse X) pulse trains [30,33,34]. We notably showed that SLP are advantageous because they are efficient, robust and easy to set up [30]. The overtone irradiation and detection at twice the ^{14}N Larmor frequency with rectangular, composite or adiabatic pulses has also been employed in HMQC experiments, but is less effective than irradiation at the ^{14}N Larmor frequency [29,35–38].

Nevertheless, an important limitation of the ^{1}H-{^{14}N} D-HMQC sequence (Fig.1a) using coherence transfers mediated by dipolar couplings is the important t_1-noise, appearing as spurious streaks along the indirect dimension, F_1. This noise reduces the sensitivity and can mask true cross peaks of low intensity, thus hampering a reliable interpretation of the 2D spectra [39,40]. This t_1-noise mostly stems from the random fluctuations of the MAS frequency [40]. The SR4_1^2 recoupling reintroduces the ^{1}H CSA, besides the ^{1}H-^{14}N dipolar interaction, and is non-γ-encoded. Because of the instabilities, the defocusing and refocusing periods of the D-HMQC sequence are not always perfectly rotor-synchronized, and hence the amplitude of the recoupled ^{1}H CSA differs between these two delays, which results in its imperfect refocusing and hence in a variation in signal amplitude from scan to scan. Owing to these variations, the uncorrelated signal is not perfectly cancelled by the phase cycling, which leads to t_1-noise. Different approaches have been proposed to reduce this limitation. It has been demonstrated that short recycle delays decrease the t_1-noise, which is coherent and hence proportional to the signal amplitude [41]. The t_1-noise in the *D*-HMQC or *D*-HSQC spectra using the $SR4_1^2$ recoupling can also be decreased by inserting two simultaneous π-pulses on ^{1}H and indirect channels in the middle of the defocusing and refocusing periods in order to refocus the ^{1}H CSA [40]. These variants have been called TONE (t_1-noise eliminated) *D*-HMQC or *D*-HSQC sequences. However, an efficient inversion of the ^{14}N magnetization using short pulses requires a high rf-power that is not compatible with the specifications of most NMR probes [33,42–46], and the TONE approach has not been reported so far for the indirect detection of ^{14}N nuclei via protons. The t_1-noise of ^{1}H-{^{14}N} *D*-HMQC 2D spectra can also be reduced by employing a γ-encoded scheme, such as the rotary resonance recoupling (R^3), which is more tolerant to MAS frequency fluctuations because the desynchronization of the defocusing and refocusing periods does not change the amplitude of the recoupled interactions, but only their phase [24,47]. Nevertheless, the R^3 scheme is sensitive to rf-inhomogeneity, notably for protons subject to small CSA.

Alternatively, the ^{1}H-^{14}N dipolar interactions can be reintroduced in HMQC experiments by applying two long identical pulses on the ^{14}N channel [48–51], like in the TRAPDOR (transfer of population in double resonance) experiment [52–54]. This combination of the TRAPDOR and HMQC schemes has been called T-HMQC [51]. These long pulses also excite and reconvert the ^{14}N coherences evolving during the t_1 period. As these long pulses are applied to the ^{14}N channel, they do not reintroduce the ^{1}H CSA, and hence the T-HMQC 2D spectra do not feature any t_1-noise [51]. To the best of our knowledge, this scheme has so far been applied for the indirect detection of ^{14}N 1Q coherences, but not of their 2Q ones.

The NMR signal of ^{14}N isotope can also be detected via protons under MAS using the double cross-polarization sequence [51,55,56]. Nevertheless, this sequence requires a careful optimization of the rf-fields on ^{1}H and ^{14}N channels during the CP transfer in order to fulfill the Hartmann-Hahn condition [55], while avoiding the R^3 ones [51].

Half-integer spin quadrupolar nuclei, including ^{17}O, ^{23}Na, ^{25}Mg, ^{27}Al, ^{35}Cl, ^{43}Ca and ^{71}Ga, have also been indirectly detected by protons [27,57–61]. This indirect detection has been achieved using either the *D*-HMQC sequence [57–61] and its TONE variant [40], or more recently the magnetization transfers between half-integer quadrupolar nuclei and protons using the through-space refocused INEPT (*D*-RINEPT) scheme [61]. It has notably been demonstrated that the *D*-HMQC sequence allows the indirect detection of the 1Q-CT and 1Q-ST coherences of ^{35}Cl nucleus [58], which is a spin-3/2 isotope with low gyromagnetic ratio ($\gamma_{35\text{Cl}}/\gamma_{1\text{H}} = 0.098$) and high natural abundance (*NA* = 75.77%). More recently, the T-HMQC experiment has been employed for the indirect detection via protons of either the 1Q (1Q-CT and 1Q-ST) and triple-quantum (3Q) coherences of ^{35}Cl nuclei or the 2Q-ST ones between energy levels $m_I = \pm3/2$ and $\mp1/2$ of this quadrupolar isotope [62]. The detection of 1Q-ST and 2Q-ST requires a very stable spinning (within a few Hz) precisely at the magic angle (within a few milli-degrees) in order to average H_{Q1}. These requirements are called STMAS specifications[63–66]. When they are met, the indirect detection of the 2Q-ST can improve the resolution by a factor of up to 18 over that of the 1Q-CT.

D-HMQC experiments with ^{1}H detection and its TONE variants have also been applied for the indirect detection of ^{195}Pt nuclei in solids [59,67–70]. ^{195}Pt is a spin-1/2 isotope with a moderate gyromagnetic ratio ($\gamma_{195\text{Pt}}/\gamma_{1\text{H}} \approx 0.215$) and natural abundance (*NA* = 33%). ^{195}Pt CSA can exceed 7000 ppm, leading to spectral breadths larger than 500 kHz at 9.4 T [71]. Therefore, the excitation of ^{195}Pt nuclei using rf-amplitudes of tens of kilohertz is challenging. This excitation has been performed using various schemes, including hard pulses, SLP and DANTE trains [68]. SLP is notably suitable for large CSA. The MAS sideband manifold of ^{195}Pt nuclei can also be recorded using rotor-asynchronous t_1-increment in a constant-time *D*-HMQC sequence [59] or preferably its arbitrary dwell time variant [70,72]. The ^{1}H signal can also be correlated with the ^{195}Pt center-band by combining the *D*-HMQC sequence with the adiabatic magic-angle turning scheme [67,70]. Nevertheless, the acquisition of two *D*-HMQC 2D spectra with different spinning speeds using rotor-synchronized t_1-increments is sufficient to determine the isotropic chemical shifts of ^{195}Pt nuclei [68].

We demonstrate herein the indirect detection of 2Q ^{14}N coherences via protons using the T-HMQC sequence. We show for the first time that the T-HMQC experiment can be applied for the indirect observation of spin-1/2 nuclei, such as ^{195}Pt, subject to large CSA. We also analyze the efficiency of the ^{1}H-{I} T-HMQC sequence for I = ^{14}N, ^{35}Cl and ^{195}Pt isotopes as function of offset, recoupling time and rf-amplitude using spin dynamics simulations. The ^{1}H-{^{14}N} and ^{1}H-{^{35}Cl} T-HMQC experiments are carried out on L-histidine·HCl, whereas the ^{1}H-{^{195}Pt} ones are performed on a mixture of *cis*- and *trans*-dichlorodiamineplatinum(II) (also called cisplatin and transplatin).

II. Pulse sequence and theory

II-1. *Pulse sequence*

The ^{1}H-{I} T-HMQC pulse sequence is displayed on Fig.1b. It consists of a rotor-synchronized spin-echo on the ^{1}H channel, i.e. the interval between the centers of the π/2 and π pulses and that between the center of the π-pulse and the beginning of the acquisition period, t_2, are equal to an integer multiple of rotor periods, mT_R. Two long rectangular pulses of identical length, τ_{mix}, and rf-strength, ν_1, are applied on the I channel during each echo delay and are separated by the t_1 evolution period. This pair of long pulses reintroduces the ^{1}H-I dipolar coupling under MAS and also creates and reconverts the I coherences evolving during the t_1 period in order to encode their frequency.

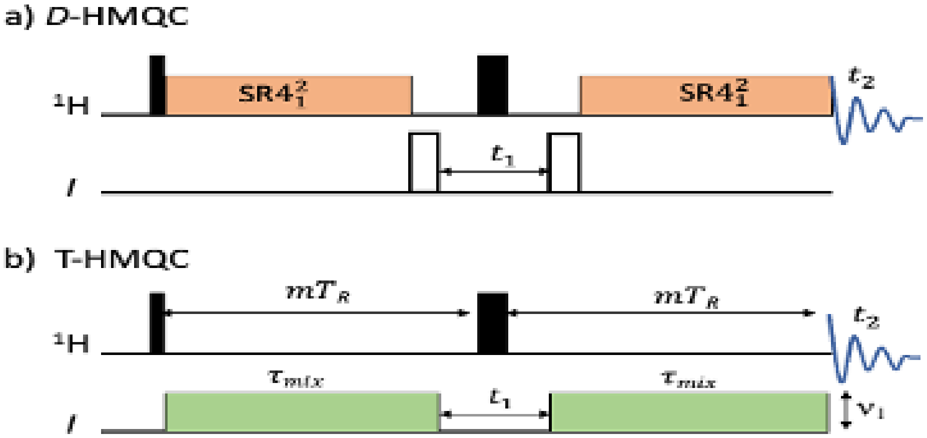

Fig.1. ^{1}H-{I} (a) D-HMQC and (b) T-HMQC pulse sequences. The ^{1}H-I dipolar couplings are reintroduced by applying either the $SR4_1^2$ recoupling on the ^{1}H channel with D-HMQC or two long identical pulses on the I channel with T-HMQC.

The phase cycling of one of these I pulses, allows selecting the coherence order during t_1. In the following, we will label the coherences according to their coherence order either followed by ST when they are subject to H_{Q1} (e.g. 1Q-ST and 2Q-ST), or without ST in other cases (e.g. 1Q-CT and 3Q for I = 3/2).

A two-step phase cycle selects simultaneously all coherences with odd order of the I isotope. This means that only the ±1Q coherences can then be detected for ^{195}Pt and ^{14}N isotopes owing to the limited sizes of their density matrices stemming from their small spin values: I = ½ and 1, respectively, whereas this phase cycling selects simultaneously 1Q-CT, 1Q-ST and 3Q for I = 3/2.

Conversely, a four-step phase cycle selects the ±2Q coherences, and notably the 2Q-ST for I = 3/2 [62]. For this spin value, the second-order quadrupolar (H_{Q2}) broadening of the 2Q-ST in hertz is 9-fold smaller than that of 1Q-CT, whereas the differences in chemical shifts for the former coherences are twice larger than for the latter [67]. Overall, the spectral resolution is hence improved by a factor of 18 by selecting the 2Q-ST, instead of 1Q-CT during t_1 period. However, the 2Q-ST are broadened by H_{Q1}, and hence this phase selection requires STMAS specifications to cancel this broadening. For I = 1, the 1Q and 2Q coherences lead to the same resolution provided they only evolve under the isotropic chemical shift and H_{Q2} interactions. However, the 1Q coherences are also subject to H_{Q1}, which is only refocused under STMAS specifications. Conversely, the 2Q coherences are immune to H_{Q1} and does not require these stringent settings.

A six-step phase cycle selects the ±3Q coherences during t_1. For $I = 3/2$, the 3Q coherences are not broadened by H_{Q1} and hence, their indirect detection does not require STMAS specifications.

II-2. *Effective TRAPDOR Hamiltonian for I = 1/2*

We consider a rectangular pulse of phase x applied under MAS to the ^{195}Pt nucleus with a carrier frequency resonant with its n^{th}-order sideband related to CSA. We neglect the off-resonance counter-rotating circular component of the linearly modulated rf-field. In the rotating frame, $\mathcal{R}$, revolving around the z-axis of the laboratory frame at $\delta_{\text{iso}}^{I}\omega_{I}^{0}$, where δ_{iso}^{I} and ω_{I}^{0} denote respectively the isotropic chemical shift and the Larmor angular frequency, the Hamiltonian of an isolated pair S = ^{1}H and I = ^{195}Pt can be expressed as

$$H^{\mathcal{R}} = \omega_{\text{CSA},I}(t)I_z + 2\omega_{\text{D},IS}(t)I_zS_z + \omega_1 R_z(n\omega_{\text{R}}t)I_xR_z(-n\omega_{\text{R}}t) \tag{1}$$

where $R_Z(\theta) = \exp(-i\theta I_z)$ is the operator for the rotation of the ^{195}Pt spin through an angle θ around the z-axis, $\omega_{\text{R}} = 2\pi\nu_{\text{R}}$ is the angular MAS frequency, $\omega_{\text{CSA},I}(t)$ is the instantaneous angular frequency of the ^{195}Pt CSA, $\omega_{\text{D},IS}(t)$ is the instantaneous angular dipolar coupling frequency, and $\omega_1 = 2\pi\nu_1$ is the amplitude of the rf-field.

The ^{195}Pt CSA is usually much larger than the ^{1}H-^{195}Pt dipolar coupling. Its MAS-modulated offset can be removed by a transformation into the jolting frame, $\mathcal{J}$ [73]:

$$H^{\mathcal{J}} = R_z\left[-\Phi_{\text{CSA},I}(t)\right]H^{\mathcal{R}}R_z\left[\Phi_{\text{CSA},I}(t)\right] - \omega_{\text{CSA},I}(t)I_z \tag{2}$$

where

$$\Phi_{\text{CSA},I}(t) = \int_0^t \omega_{\text{CSA},I}(t')\,\mathrm{d}t' \tag{3}$$

is the phase related to the evolution under ^{195}Pt CSA. MAS modulates the ^{195}Pt CSA and ^{1}H-^{195}Pt dipolar interaction at the frequency ω_{R}. Hence, the Hamiltonian $H^{\mathcal{J}}$ can be expressed as [33]

$$H^{\mathcal{J}} = \sum_{p=-\infty}^{+\infty}\left[2\omega_p^{D,IS}I_zS_z + h_p^{\text{rf}}\right]\exp\left(ip\omega_{\text{R}}t\right) \tag{4}$$

where the complex amplitudes of the components of the ^{1}H-^{195}Pt dipolar interaction are equal to [74]

$$\omega_{\pm1}^{D,IS} = \mp\frac{1}{2\sqrt{2}}b_{IS}\sin\left(2\beta_{PR}^{D,IS}\right)\exp\left[\mp i\left(\gamma_{PR}^{D,IS} + \alpha_{RL}^{0}\right)\right], \tag{5}$$

$$\omega_{\pm2}^{D,IS} = \frac{1}{4}b_{IS}\sin^2\left(\beta_{PR}^{D,IS}\right)\exp\left[\mp i2\left(\gamma_{PR}^{D,IS} + \alpha_{RL}^{0}\right)\right], \tag{6}$$

whereas the other components are null. In Eqs. 5 and 6, b_{IS} is the dipolar coupling in rad.s^{-1}, {0, $\beta_{PR}^{D,IS}$, $\gamma_{PR}^{D,IS}$} Euler angles relate the I-S inter-nuclear direction to the MAS rotor-fixed frame and α_{RL}^{0} denotes the rotor angular position at the beginning of the pulse. The Floquet coefficients of the rf Hamiltonian have the following expression [33]

$$h_p^{\text{rf}} = \frac{\omega_1}{2}\left[A_{n-p}\exp\left(-i\phi_{n-p}\right)I_- + A_{n+p}\exp\left(i\phi_{n+p}\right)I_+\right] \tag{7}$$

where $A_{n\pm p}$ and $\phi_{n\pm p}$ are the amplitude and the phase of the $(n \pm p)^{\text{th}}$-order sidebands of the crystallite and $I_\pm$ denotes the ladder operators of the ^{195}Pt nucleus. The first-order effective Hamiltonian corresponds to the time-independent term $p = 0$ in Eq. 4 and is equal to the Floquet coefficient h_0^{rf}:

$$H_{\text{eff}}^{(1)} = h_0^{\text{rf}} = \omega_1 A_n R_z(-\phi_n)I_xR_z(\phi_n), \tag{8}$$

which is identical to the Hamiltonian of a rectangular pulse applied to the ^{195}Pt nucleus with amplitude $\omega_1 A_{\text{n}}$ and phase ϕ_n. The scaling down of the rf-field by A_{n} stems from the fact that it rotates the magnetization only during a fraction of the pulse since the modulation of CSA by MAS produces a rapid change of the offset. The ratio A_{n} and the phase ϕ_n depend on the orientation of the CSA tensor in the rotor frame. This dependence results in a distribution of the rf-strength and a spread of its direction between the crystallites of a powder.

For large rf-amplitude, higher order terms of the rf Hamiltonian must be included. The second-order effective rf Hamiltonian is equal to [33,75]

$$H_{\text{eff,rf}\times\text{rf}}^{(2)} = \frac{\omega_1^2}{\omega_R}\sum_{p\neq0}\frac{A_{n+p}^2 - A_{n-p}^2}{p}I_z \tag{9}$$

This constant term represent a Bloch-Siegert shift [76,77], which does not depend on the phases of the rf-pulse and the spinning sidebands (ϕ_n). Its magnitude increases with ω_1^2/ω_R and the asymmetry of the sideband intensities about the irradiated sideband.

As seen in Eqs. 8 and 9, neither $H_{\mathrm{eff}}^{(1)}$ nor $H_{\mathrm{eff,rf\times rf}}^{(2)}$ depend on b_{IS} and account for the reintroduction of ^{1}H-^{195}Pt dipolar coupling by the long pulse, even if, as shown below, these terms do not commute with the recoupled ^{1}H-^{195}Pt dipolar interaction and affect the ^{1}H-^{195}Pt coherence transfer during the TRAPDOR pulses by modifying the quantization axis. On the contrary, the ^{1}H-^{195}Pt dipolar interaction contributes to the second-order effective Hamiltonian via the following term

$$H_{\mathrm{eff},IS\times\mathrm{rf}}^{(2)} = -\frac{1}{2}\sum_{p\neq 0}\frac{\left[2\omega_{-p}^{D,IS}I_zS_z, h_p^{\mathrm{rf}}\right]+\left[h_{-p}^{\mathrm{rf}}, 2\omega_p^{D,IS}I_zS_z\right]}{p\omega_R}. \tag{10}$$

By substituting Eq. 7 into Eq. 10, this Hamiltonian can be written as

$$H_{\mathrm{eff},IS\times\mathrm{rf}}^{(2)} = \frac{\omega_1}{2\omega_R}\sum_{\substack{p=-2\\ p\neq 0}}^{2}\operatorname{sign}(p)\,\omega_p^{D,IS}\left[-A_{n+p}\exp\left(-i\phi_{n+p}\right)I_- + A_{n-p}\exp\left(i\phi_{n-p}\right)I_+\right]S_z. \tag{11}$$

This equation shows that the rectangular pulse, resonant with the n^{th}-order sideband of ^{195}Pt nucleus, reintroduces the hetero-nuclear dipolar coupling and converts the ^{1}H 1Q coherences into ^{1}H-^{195}Pt multiple-quantum coherences evolving during the t_1 period of the T-HMQC sequence.

Eq. 11 shows that the amplitude of the $H_{\mathrm{eff},IS\times\mathrm{rf}}^{(2)}$ term governing the ^{1}H-^{195}Pt coherence transfer depends on the $\omega_1 A_{n+p} b_{IS}/\omega_R$ ratios, with $p = \pm 1$ and ± 2. The A_k amplitudes satisfy the normalization conditions [78]:

$$\sum_{k=-\infty}^{+\infty} A_k^2 = 1. \tag{12}$$

Let us call CSA the full width of the static powder pattern:

$$\mathrm{CSA} = \delta_{\mathrm{aniso}}^{I}\omega_I^0(3+\eta_{\mathrm{CSA}})/2, \tag{13}$$

where $\delta_{\mathrm{aniso}}^{I}$ and η_{CSA} denote the anisotropic chemical deshielding constant and the shielding asymmetry parameter of ^{195}Pt nucleus. The number of spinning sidebands with significant intensities is approximately equal to CSA/ω_R and hence, in average

$$A_k \approx \sqrt{\frac{\omega_R}{CSA}}. \tag{14}$$

Therefore, the norm of $H_{\mathrm{eff},IS\times\mathrm{rf}}^{(2)}$ is approximately proportional to

$$\left\|H_{\mathrm{eff},IS\times\mathrm{rf}}^{(2)}\right\| \propto \sqrt{\alpha}\,b_{IS} \tag{15}$$

where the adiabaticity parameter, α, is given by

$$\alpha = \frac{\omega_1^2}{\omega_R CSA}. \tag{16}$$

For ν_1 = 186 and ν_R = 62.5 kHz, corresponding to the experimental conditions used in section IV.2, and $\delta_{\mathrm{aniso}}^{I}\omega_I^0/(2\pi)$ = 1.02 MHz and η_{CSA} = 0.03 (CSA = 1.55 MHz), which are the CSA parameters of ^{195}Pt nucleus in cisplatin [59], we have $\alpha \approx 0.36$. Therefore, the build-up of the T-HMQC signal, which is proportional to $\sqrt{\alpha}$ (Eq. 15), is accelerated at higher rf-field, whereas it is slowed down at larger CSA and MAS frequency.

Furthermore, the magnitude of $H_{\mathrm{eff}}^{(1)} = h_0^{\mathrm{rf}}$ is much larger than that of $H_{\mathrm{eff},IS\times\mathrm{rf}}^{(2)}$. In the interaction frame of h_0^{rf}, the effective Hamiltonian is equal to

$$H^{h0}(t) = \exp\left(ih_0^{\mathrm{rf}}t\right)\left(H_{\mathrm{eff,rf\times rf}}^{(2)} + H_{\mathrm{eff},IS\times\mathrm{rf}}^{(2)}\right)\exp\left(-ih_0^{\mathrm{rf}}t\right). \tag{17}$$

The terms of $H_{\mathrm{eff,rf\times rf}}^{(2)} + H_{\mathrm{eff},IS\times\mathrm{rf}}^{(2)}$ which do not commute with h_0^{rf}, oscillate rapidly and are averaged out by the rf-field. Therefore, the recoupling of the ^{1}H-^{195}Pt dipolar interaction is governed by the projection of $H_{\mathrm{eff},IS\times\mathrm{rf}}^{(2)}$ onto $h_0^{\mathrm{rf}}S_z$:

$$H_{\mathrm{eff},IS\times\mathrm{rf}}^{(2),h0} = \frac{\mathrm{Tr}\left(S_z h_0^{\mathrm{rf},\dagger} H_{\mathrm{eff},IS\times\mathrm{rf}}^{(2)}\right)}{\mathrm{Tr}\left(S_z h_0^{\mathrm{rf},\dagger} h_0 S_z\right)} h_0^{\mathrm{rf}} S_z. \tag{18}$$

where $h_0^{\mathrm{rf},\dagger}$ denotes the Hermitian adjoint of h_0^{rf} and Tr(B) denotes the trace of the matrix B. The magnitude of this term (i) is proportional to $\sqrt{\alpha}$, and (ii) depends on the sideband intensities, $A_{n\pm p}$, and phases, $\phi_{n\pm p}$, with $p = \pm 1$ or ± 2.

II-3. *Effective TRAPDOR Hamiltonian for I = 1*

We now consider the case of the ^{1}H-{^{14}N} T-HMQC pulse sequence. Two rectangular pulses of phase *x* are applied under MAS to the ^{14}N nucleus with a carrier frequency resonant with the *n*th and –*n*th order sidebands of the transitions between energy levels +1 ↔ 0 and 0 ↔ −1, respectively. In the case of an isolated spin pair, *S* = ^{1}H and *I* = ^{14}N, the Hamiltonian in the $\mathcal{R}$ rotating frame is equal to

$$H^{\mathcal{R}}(t) = \omega_{\mathrm{Q},I}(t)Q_z + 2\omega_{\mathrm{D},IS}(t)I_zS_z + \omega_1 R_z(n\omega_{\mathrm{R}}t)I_xR_z(-n\omega_{\mathrm{R}}t) \tag{19}$$

where $Q_z = I_z^2 - I(I+1)\mathbf{1}_I/3$ is the quadrupolar order, $\mathbf{1}_I$ is the identity matrix of size $2I+1 = 3$ and $\omega_{\mathrm{Q},I}(\mathrm{t})$ is the instantaneous H_{Q1} interaction. In Eq. 19, we disregarded the CSA and the anisotropic part of H_{Q2}, since they are usually smaller than the MAS frequency. Furthermore, the isotropic part of H_{Q2}, also called QIS (quadrupolar-induced shift), $\omega_{\mathrm{QIS}}^{I}$, is included in the frequency offset of the ^{14}N nucleus and the $\mathcal{R}$ frame revolves around the z-axis of the laboratory frame at the angular frequency, $\delta_{\mathrm{iso}}^{I}\omega_I^0 + \omega_{\mathrm{QIS}}^{I}$.

As H_{Q1} of ^{14}N nucleus is usually much larger than the ^{1}H-^{14}N dipolar coupling, the Hamiltonian is transformed into the quadrupolar jolting frame, $\mathcal{J}$, in order to remove its modulation by MAS

$$H^{\mathcal{J}}(t) = \exp\left[i\Phi_{\mathrm{Q},I}(t)Q_z\right]H^{\mathcal{R}}\exp\left[-i\Phi_{\mathrm{Q},I}(t)Q_z\right] - \omega_{\mathrm{Q},I}(t)Q_z \tag{20}$$

where

$$\Phi_{\mathrm{Q},I}(t) = \int_0^t \omega_{\mathrm{Q},I}(t')\,\mathrm{d}t' \tag{21}$$

is the phase evolution under H_{Q1}. Owing to the periodicity of the MAS rotation, the Hamiltonian $H^{\mathcal{J}}$ can be written as in Eq. 4 [33], in which the Floquet coefficients of the rf Hamiltonian are given by

$$h_p^{\mathrm{rf}} = \sqrt{\frac{1}{2}}\omega_1\begin{bmatrix} A_{n-p}\exp(-i\phi_{n-p})I_-^{(+1,0)} + A_{n+p}\exp(i\phi_{n+p})I_+^{(+1,0)} \\ +A_{-n+p}\exp(i\phi_{-n+p})I_-^{(0,-1)} + A_{-n-p}\exp(-i\phi_{-n-p})I_+^{(0,-1)} \end{bmatrix}. \tag{22}$$

where $I_\pm^{(+1,0)}$ and $I_\pm^{(0,-1)}$ denote the ladder operators of the transitions +1 ↔ 0 and 0 ↔ −1, respectively, and the coefficients of $I_\pm^{(\pm1,0)}$ operators are the complex conjugates of those $I_\pm^{(0,\mp1)}$.

The first-order effective Hamiltonian is the coefficient h_0^{rf}:

$$H_{\mathrm{eff}}^{(1)} = h_0^{\mathrm{rf}} = \sqrt{2}\omega_1\begin{bmatrix} A_nR_z^{(+1,0)}(-\phi_n)I_x^{(+1,0)}R_z^{(+1,0)}(\phi_n) \\ +A_{-n}R_z^{(0,-1)}(\phi_{-n})I_x^{(0,-1)}R_z^{(0,-1)}(-\phi_{-n}) \end{bmatrix} \tag{23}$$

where $R_z^{(+1,0)}(\theta) = \exp\left(-i\theta I_z^{(+1,0)}\right)$ and $R_z^{(0,-1)}(\theta) = \exp\left(-i\theta I_z^{(0,-1)}\right)$. The above Hamiltonian corresponds to two pulses of distinct amplitudes and phases applied to the transitions +1 ↔ 0 and 0 ↔ −1, respectively.

The second-order effective rf Hamiltonian comprises terms proportional to $I_z^{(+1,0)}$ and $I_z^{(0,-1)}$, representing the Bloch-Siegert shift, as well as double-quantum terms [33]. By substituting Eq.23 into Eq.10, the contribution of the ^{1}H-^{14}N dipolar interaction to the second-order effective Hamiltonian can be expressed as

$$H_{\mathrm{eff},IS\times\mathrm{rf}}^{(2)} =$$

$$\frac{\omega_1}{\sqrt{2}\omega_R}\sum_{\substack{p=-2\\p\neq0}}^{2}\mathrm{sign}(p)\omega_p^{D,IS}\begin{bmatrix} -A_{n+p}\exp(-i\phi_{n+p})I_-^{(+1,0)} + A_{n-p}\exp(i\phi_{n-p})I_+^{(+1,0)} \\ -A_{-n-p}\exp(i\phi_{-n-p})I_-^{(0,-1)} + A_{-n+p}\exp(-i\phi_{-n+p})I_+^{(0,-1)} \end{bmatrix}S_z. \tag{24}$$

As h_0^{rf} is much larger than this Hamiltonian, the evolution of the spin system can be described in the h_0^{rf} interaction frame (Eq. 17) and the transfer of coherence between ^{1}H and ^{14}N nuclei is governed by the projection of $H_{\mathrm{eff},IS\times\mathrm{rf}}^{(2)}$ onto $h_0^{\mathrm{rf}}S_z$ given by Eq. 18. This effective Hamiltonian transforms the in-phase transverse ^{1}H magnetization, S_x, into (i) a transverse ^{1}H magnetization antiphase with respect to ^{1}H-^{14}N coupling, $S_x\left(I_z^2 - \frac{2}{3}\mathbf{1}_I\right)$, as well as (ii) ^{1}H-^{14}N multiple-quantum coherences with 1Q and 2Q ^{14}N coherences.

As the full width powder pattern of a I spin nucleus is $1.5C_Q/I$ [79], in average we have

$$A_k \approx \sqrt{\frac{I\omega_R}{1.5C_Q}} \tag{25}$$

using the normalization condition of Eq. 12 and hence, Eq. 15 is still valid with the adiabaticity parameter, α, given by

$$\alpha = \frac{I\omega_1^2}{1.5\omega_R C_Q}\,. \tag{26}$$

For ^{14}N nuclei with $\nu_1 = 70$, $\nu_R = 62.5$ kHz and $C_Q = 1.18$ MHz, we have $\alpha \approx 0.04 << 1$.

In the special case, in which the centerband is irradiated ($n = 0$), the coefficients of $I_{\pm}^{(+1,0)}$ and $I_{\mp}^{(0,-1)}$ operators in Eq. 24 are opposite. As a result, $H_{\text{eff},IS\times\text{rf}}^{(2)}$ is orthogonal to h_0^{rf}, which fully decouples the ^{1}H-^{14}N dipolar interaction, and cancels the T-HMQC signal.

Furthermore, the third-order effective term between two rf Hamiltonians and the ^{1}H-^{14}N dipolar interaction, $H_{\text{eff},IS\times\text{rf}\times\text{rf}}^{(3)}$ (Eq.S1), contains products of S_z and ^{14}N 2Q operators [33]. These product operators can transform S_x into ^{1}H-^{14}N coherences involving ^{14}N 2Q coherences. As this third-order term is proportional to αb_{IS} and $\alpha \leq \sqrt{\alpha} \leq 1$, its contribution to the creation of ^{14}N 2Q coherences increases with the ^{1}H-^{14}N dipolar interaction and the length of the TRAPDOR pulses.

We considered above the irradiation of the n^{th}-order sideband. When irradiating the midpoint between two consecutive spinning sidebands, *i.e.* the frequency offset is equal to $(n + 1/2)\nu_R$, h_p^{rf} must be replaced by $h_p^{\text{rf}}\exp(i\omega_R t/2)$ in Eq. 4. Hence, the first-order Hamiltonian and the contribution of the ^{1}H-^{14}N dipolar interaction to the second-order effective Hamiltonian are time-dependent and canceled by MAS since the rf-field is modulated at a half-integer multiple of the MAS frequency, whereas the H_{Q1} and ^{1}H-^{14}N dipolar interactions are modulated at multiples of the MAS frequency. Nevertheless, the third-order effective Hamiltonian of Eq. S2 contains time-independent terms recoupling the ^{1}H-^{14}N dipolar interaction [33]. As this Hamiltonian contains products of S_z and ^{14}N 2Q operators, the irradiation at the midpoint between two consecutive spinning sidebands can transform S_x into ^{1}H-^{14}N coherences involving 2Q coherences. As the third-order term is proportional to αb_{IS} and $\alpha \leq \sqrt{\alpha} \leq 1$, the build-up of the ^{14}N 2Q coherences in T-HMQC experiments is slower at these offsets than for the irradiation of a sideband.

II-4. ***Effective TRAPDOR Hamiltonian for I = 3/2***

For the ^{1}H-{^{35}Cl} T-HMQC sequence, two rectangular pulses of phase x are applied under MAS to the ^{35}Cl channel with a carrier frequency resonant with sidebands of order n and $-n$ of the transitions 3/2 ↔ 1/2 and −1/2 ↔ −3/2, respectively. The Hamiltonian of the ^{1}H–^{35}Cl spin pair in the $\mathcal{R}$ frame is equal to

$$H^{\mathcal{R}} = \omega_{Q,I}(t)Q_z + 2\omega_{D,IS}(t)I_zS_z + \omega_1 R_z(n\omega_R t)I_x R_z(-n\omega_R t) \tag{27}$$

in which the ^{35}Cl CSA and H_{Q2} interactions are disregarded.

The STs of the ^{35}Cl nucleus 3/2 ↔ 1/2 and −1/2 ↔ −3/2 are similar to those of ^{14}N isotope: +1 ↔ 0 and 0 ↔ −1, whereas the ^{35}Cl 1Q-CT coherence does not evolve under H_{Q1} and only contributes to the centerband. By analogy with a spin $I = 1$, it can be shown that the Floquet coefficients of the rf Hamiltonian for $I = 3/2$ in the quadrupolar jolting frame are equal to

$$h_p^{\text{rf}} = \frac{\sqrt{3}}{2}\omega_1 \begin{bmatrix} A_{n-p}\exp(-i\phi_{n-p})I_-^{\left(+\frac{3}{2},+\frac{1}{2}\right)} + A_{n+p}\exp(i\phi_{n+p})I_+^{\left(+\frac{3}{2},+\frac{1}{2}\right)} \\ +A_{-n+p}\exp(i\phi_{-n+p})I_-^{\left(-\frac{1}{2},-\frac{3}{2}\right)} + A_{-n-p}\exp(-i\phi_{-n-p})I_+^{\left(-\frac{1}{2},-\frac{3}{2}\right)} \end{bmatrix} + \omega_1\delta_{n0}\delta_{p0}C_x. \tag{28}$$

where C_x is the CT SQ coherence along the x-axis, and δ_{n0} and δ_{p0} denote Kronecker delta functions [80]. Similarly by analogy with Eq. 24, the contribution of the ^{1}H-^{35}Cl dipolar interaction to the second-order effective Hamiltonian is

$$H^{(2)}_{\mathrm{eff},IS\times\mathrm{rf}} =$$

$$\frac{\sqrt{3}\omega_1}{2\omega_R}\sum_{\substack{p=-2\\p\neq 0}}^{2} \mathrm{sign}(p)\omega_p^{D,IS}\begin{bmatrix} -A_{n+p}\exp(-i\phi_{n+p})I_-^{\left(+\frac{3}{2},+\frac{1}{2}\right)} + A_{n-p}\exp(i\phi_{n-p})I_+^{\left(+\frac{3}{2},+\frac{1}{2}\right)} \\ -A_{-n-p}\exp(i\phi_{-n-p})I_-^{\left(-\frac{1}{2},-\frac{3}{2}\right)} + A_{-n+p}\exp(-i\phi_{-n+p})I_-^{\left(-\frac{1}{2},-\frac{3}{2}\right)} \\ -\frac{\mathrm{sign}(p)}{\sqrt{3}}\left(-I_-^{\left(+\frac{1}{2},-\frac{1}{2}\right)} + I_+^{\left(+\frac{1}{2},-\frac{1}{2}\right)}\right) \end{bmatrix} S_z. \qquad (29)$$

The full width of the ^{35}Cl powder pattern is C_Q [79], and the adiabaticity parameter, α, is given Eq. 26. As $H^{(1)}_{\mathrm{eff}} = h_0^{\mathrm{rf}}$ is larger than $H^{(2)}_{\mathrm{eff},IS\times\mathrm{rf}}$, it truncates this second-order Hamiltonian and the ^{1}H-^{35}Cl recoupling is governed by a Hamiltonian proportional to $h_0^{\mathrm{rf}}S_z$, which converts S_x into ^{1}H-^{35}Cl multiple-quantum coherences with 1Q-CT, 1Q-ST, 2Q-ST and 3Q. In the case of a centerband irradiation, $H^{(2)}_{\mathrm{eff},IS\times\mathrm{rf}}$ is orthogonal to h_0^{rf} and the T-HMQC signal is null. When irradiating the midpoint between two consecutive spinning sidebands, the third-order effective Hamiltonian between two rf Hamiltonians and the ^{1}H-^{35}Cl dipolar interaction in the form of Eq.S2 can transform S_x into ^{1}H-^{35}Cl multiple-quantum coherences involving 2Q-ST of ^{35}Cl isotope. Furthermore, the fourth-order effective Hamiltonian between three rf Hamiltonians and the ^{1}H-^{35}Cl dipolar interaction (not shown) can convert S_x into ^{1}H-^{35}Cl coherences with 1Q-CT, 1Q-ST and 3Q, for $\nu_{\mathrm{off}} = (n + 1/3)\nu_R$.

II-5. *Expression of the* T-*HMQC signal*

For a ^{1}H-{I} T-HMQC sequence, the phase cycling selects during t_1 the coherence order of spin I, q_I, and the NMR signal is proportional to

$$\sum_{l,qI}\langle\left(S_x|U_{\mathrm{mix}}T^I_{l,qI}U^{-1}_{\mathrm{mix}}\right)\left(T^I_{l,qI}|U_{\mathrm{t1}}T^I_{l,qI}U^{-1}_{\mathrm{t1}}\right)\left(T^I_{l,qI}|U_{\mathrm{mix}}S_xU^{-1}_{\mathrm{mix}}\right)\rangle \qquad (30)$$

where the angular bracket denotes the powder average and the scalar product in operator space is defined by $(A|B) = \mathrm{Tr}\{A^\dagger B\}$, with $A^\dagger$ the Hermitian adjoint of A. U_{mix} denotes the propagators for the two identical TRAPDOR pulses, which are equal when τ_{mix} and t_1 are multiples of T_R. In this case, when neglecting the third-order Hamiltonians, U_{mix} is equal to

$$U_{\mathrm{mix}} = \exp\left[-i\left(H^{(2),h0}_{\mathrm{eff,rf}\times\mathrm{rf}} + H^{(2),h0}_{\mathrm{eff},IS\times\mathrm{rf}}\right)\tau_{\mathrm{mix}}\right] \qquad (31)$$

where $H^{(2),h0}_{\mathrm{eff,rf}/IS\times\mathrm{rf}}$ are the projections of $H^{(2)}_{\mathrm{eff,rf}/IS\times\mathrm{rf}}$ onto h_0^{rf} (Eq.18):

$$H^{(2),h0}_{\mathrm{eff,rf}/IS\times\mathrm{rf}} = \frac{\mathrm{Tr}\left(h_0^{\mathrm{rf},\dagger}H^{(2)}_{\mathrm{eff,rf}/IS\times\mathrm{rf}}\right)}{\mathrm{Tr}\left(h_0^{\mathrm{rf},\dagger}h_0\right)}h_0^{\mathrm{rf}}. \qquad (32)$$

In Eq. 30, U_{t1} denotes the propagator for the t_1 evolution under the isotropic chemical and quadrupolar induced shifts, and $T^I_{l,qI}$ the irreducible tensor operator of spin I, with rank $0 \le l \le 2I$, and coherence order $-l \le q_I \le +l$ [81]. The t_1 rotor-synchronization also ensures the absence of evolution under CSA, dipolar and H_{Q1} interactions of I spin and the evolution of $T^I_{l,qI}$ operator during t_1 can be written

$$\left(T^I_{l,qI}|U_{\mathrm{t1}}T^I_{l,qI}U^{-1}_{\mathrm{t1}}\right) = \exp(-iq_I\Omega_I^0 t_1) \qquad (33)$$

where Ω_I^0 denotes the angular frequency corresponding to the isotropic shift. By substituting Eq.33 into Eq. 30 and using the complex conjugation property of the scalar product and the invariance of the trace under cyclic permutation, Eq. 30 simplifies into

$$\sum_{l,qI}\exp(-iq_I\Omega_I^0 t_1)\,\langle\left|\left(T^I_{l,qI}|U_{\mathrm{mix}}S_xU^{-1}_{\mathrm{mix}}\right)\right|^2\rangle. \qquad (34)$$

As the last term of this equation is a real number, the coherence transfer during the T-HMQC sequence only modulates the amplitude of the signal, not its phase. Globally, this is due to the fact this scheme uses two identical long TRAPDOR pulses on the quadrupolar channel, symmetrical with respect to the refocusing π-pulse on the ^{1}H channel. This symmetry allows canceling the dephasings under anisotropic interaction, hence increasing the sensitivity of the method. This feature contrasts with the conventional

TRAPDOR experiment [50-52], where only one long pulse is sent on the quadrupolar channel. In this case, the dephasings under anisotropic interaction are not refocused.

III. Numerical simulations

III-1. *Simulation parameters*

All numerical simulations of the ^{1}H-{I} T-HMQC sequence were performed using the SIMPSON software for an isolated ^{1}H-I pair without ^{1}H CSA [82]. The powder average was calculated using 232 {α_{MR},β_{MR}} pairs and 74 γ_{MR} Euler angles to relate the molecular and rotor frames in the case of I = ^{195}Pt, whereas we employed only 168 {α_{MR},β_{MR}} pairs and 11 γ_{MR} angles for I = ^{14}N and ^{35}Cl. The REPULSION algorithm was employed to select the {α_{MR},β_{MR}} pairs [83], whereas the γ_{MR} angles were regularly stepped between 0° and 360°.

For I = ^{195}Pt, the dipolar coupling was equal to $|b_{1H\text{-}195Pt}|/(2\pi)$ = 2 kHz, whereas the ^{195}Pt CSA ranged from $\delta^{195\mathrm{Pt}}_{\mathrm{aniso}}\omega^0_{195\mathrm{Pt}}$ = 0 to 3 MHz and η_{CSA} was equal to 0 or 1. For I = ^{14}N, the dipolar coupling was equal to $|b_{1H\text{-}14N}|/(2\pi)$ = 1, 2 or 8 kHz, whereas the {C_Q; η_Q} values were equal to {1.18 MHz; 0.50} or {3.21 MHz; 0.32}, corresponding to the quadrupolar parameters of ^{14}N nuclei in glycine [84] or N-acetyl-L-valine (NAV) [85]. For I = ^{35}Cl, the dipolar coupling was equal to $|b_{1H\text{-}35Cl}|/(2\pi)$ = 580 Hz, whereas C_Q = 1.95 MHz and η_Q = 0.66, corresponding to the quadrupolar parameters of ^{35}Cl nuclei in L-histidine·HCl [61].

The static magnetic field was equal to B_0 = 18.8 T and the MAS frequency to 25 or 62.5 kHz. For all 1D simulations (Figs. 2-11 and S1-S3), the t_1 period was null, *i.e.* there was no window delay between the pulses on I channel in order to avoid the evolution under the isotropic shift of I nuclei. The defocusing and refocusing periods were equal to an integer number of rotor-periods: $\tau_{mix} = mT_R$. The pulses on the ^{1}H channel were simulated as ideal Dirac ones. The long rectangular pulses on the I channel were applied on-resonance with the centerband for I = ^{195}Pt and with the first spinning sideband for I = ^{14}N and ^{35}Cl, except in Figs. **2**, **5**, **8** and **11**, where we optimized the frequency offset, ν_{off}, which is defined as the difference between the carrier frequency and the sum of the isotropic chemical shift and the QIS. The transfer efficiency of the T-HMQC sequence was normalized with respect to that of a spin echo made of ideal Dirac pulses applied to the ^{1}H channel.

III-2. *^{1}H-{^{195}Pt} T-HMQC*

Figs.**2a**-**e** show the simulated efficiency of the ^{1}H-{^{195}Pt} T-HMQC sequence versus the ^{195}Pt offset for a ^{1}H-^{195}Pt spin pair. These simulations demonstrate that the T-HMQC sequence can be applied for the indirect detection of ^{195}Pt nuclei, and more generally of any spin-1/2 isotope, subject to large shielding. For CSA ranging from ca. 50 to 2000 kHz, the optimal transfer efficiency reaches ca. 20%, instead of 50% for ^{1}H-{^{195}Pt} *D*-HMQC sequence employing rf-field larger than the CSA [72]. The transfer efficiency of T-HMQC is maximal when irradiating one of the ^{195}Pt spinning sidebands (Fig.**2b**), and contrary to ^{14}N and ^{35}Cl quadrupolar nuclei (see below), there is no drop in efficiency when irradiating the centerband. As seen in Eq.11, the ^{1}H-^{195}Pt T-HMQC efficiency depends on the amplitudes of the $A_{n\pm p}$ terms, with p = ±1 and ±2, where n denotes the order of the irradiated spinning sideband, and hence is determined by the envelope of the spinning sideband manifold. For instance, the transfer efficiency profile is symmetric with respect to the centerband for η_{CSA} = 1 (Fig.**2a**,**c**,**e**) and asymmetric otherwise (Fig.**2d**). Its excitation bandwidth is comparable to the full width of the static powder pattern (Eq.13): CSA = $\delta^I_{\mathrm{aniso}}\omega^0_I(3+\eta_{\mathrm{CSA}})/2 \approx 3$, 2.25 and 0.75 MHz for {$\delta^I_{\mathrm{aniso}}\omega^0_I$ (MHz), η_{CSA}} = {1.5, 1}, {1.5, 0} and {0.375, 1}, as shown in Figs. **2c**, **2d** and **2e**, respectively. As seen in Fig.**2f**, the T-HMQC efficiency cancels out for vanishing CSA. In that case, the theoretical treatment given in section II-2 is not valid and the rf irradiation on the ^{195}Pt channel does not recouple the ^{1}H-^{195}Pt dipolar interaction.

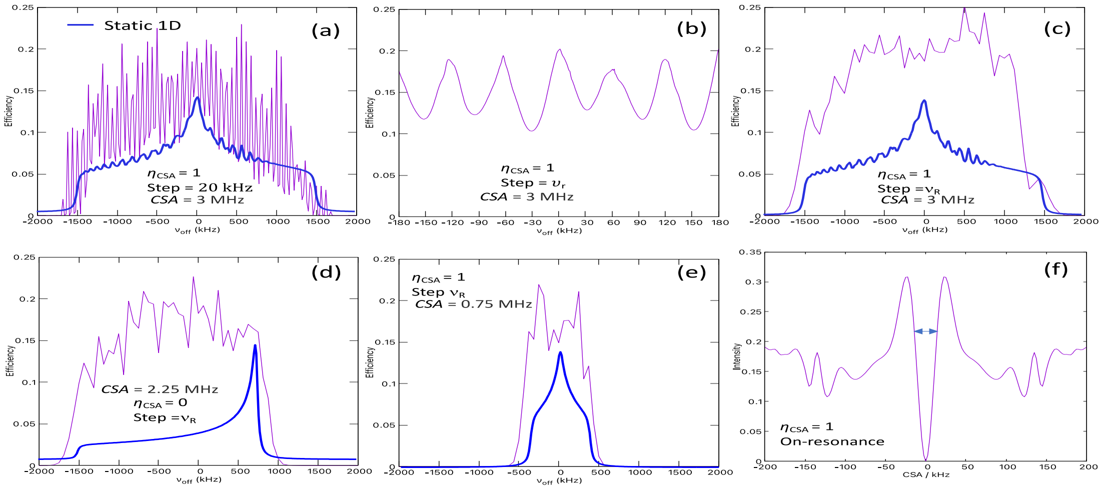

Fig.2. Simulated efficiency of the ^{1}H-{^{195}Pt} *T*-HMQC sequence as function of (a-e) offset and (f) CSA with ν_R = 62.5, ν_1 = 50 kHz and τ_{mix} = 2 ms. The panels a, c, d and e also display the 1D ^{195}Pt static spectra. Other simulation parameters are indicated on the subfigures.

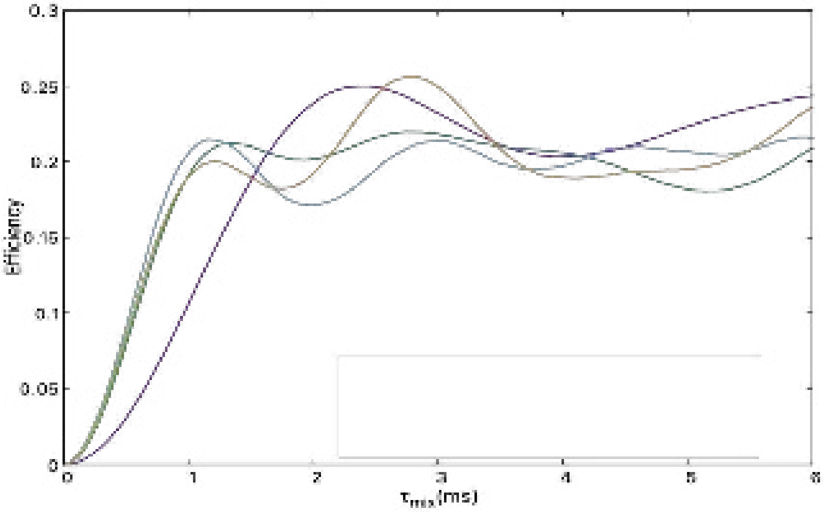

Fig.3. Simulated build-up curves of the ^{1}H-{^{195}Pt} T-HMQC sequence with η_{CSA} = 1 and {CSA (MHz), ν_R (kHz), ν_1 (kHz), α} = {3, 62.5, 50, 0.013} (purple), {3, 62.5, 100, 0.053} (green), {3, 15.625, 50, 0.053} (blue) and {0.75, 62.5, 50, 0.053} (yellow). The adiabaticity parameter α is calculated with Eqs.13 and 16.

Fig.3 displays the ^{1}H-{^{195}Pt} T-HMQC build-up curves simulated for different values of CSA, ν_R and ν_1 parameters. These simulations confirm the validity of Eqs.15 and 16, since build-up curves with identical α values exhibit the same initial slope, whereas a four-fold reduction of the α parameter decreases the initial slope by a factor 2.

Fig.4 shows the efficiency of the ^{1}H-{^{195}Pt} T-HMQC sequence as function of τ_{mix} and ν_1 parameters. These simulations show that the optimal recoupling time is inversely proportional to ν_1 in agreement with Eqs.15 and 16, which predict that the strength of the recoupled dipolar interaction is proportional to ν_1. Furthermore, for a given τ_{mix} delay, the optimal ν_1 increases with the CSA value in agreement with Eq.16 (compare Figs. 4a, 4b and 4c). These simulations show that in principle, an efficient recoupling can be achieved using long τ_{mix} delay and low ν_1 amplitude, even in the case of large ^{195}Pt CSA. Nevertheless, in practice, the ^{1}H echo signal decays with the time constant, *T*$_2$', of a few milliseconds because of residual ^{1}H-^{1}H dipolar interactions, which are not fully averaged out by MAS. As seen in Fig.4d, these losses can require the use of short τ_{mix} delay and hence high ν_1 amplitude.

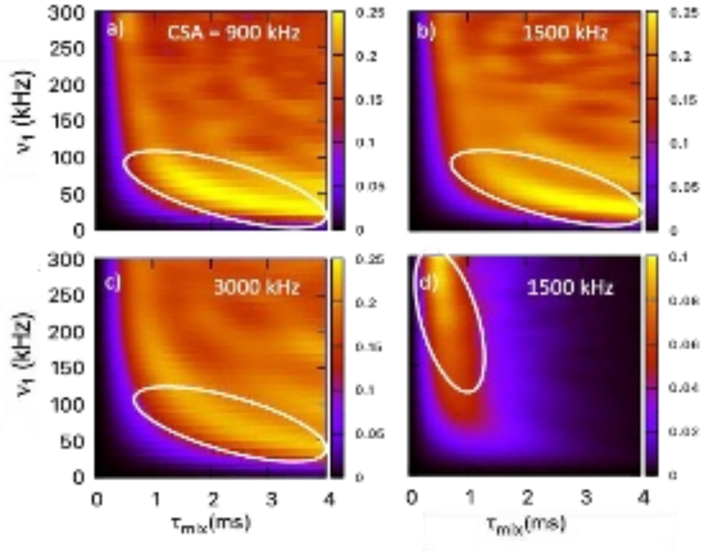

Fig.4. Simulated on-resonance efficiency of the ^{1}H-{^{195}Pt} T-HMQC sequence versus ν_1 and τ_{mix} with ν_R = 62.5 kHz and η_{CSA} = 1. The CSA values are indicated on the panels. In (d), the transfer efficiency shown in (b) has been multiplied by exp($-2\tau_{\text{mix}}/T_2$') with T_2' = 1.6 ms in order to take into account the losses due to transverse relaxation during the recoupling periods. The efficiency scale of (d) differs from that of the other panels.

III-3. *^{1}H-{^{14}N} T-HMQC*

^{14}N^{1Q}. The efficiency of the ^{1}H-{^{14}N^{1Q}} T-HMQC sequence as function of offset is shown in Fig.5. The offset profile does not strongly depend on the ^{1}H-^{14}N dipolar coupling. A major difference with respect to the simulated offset profile of the ^{1}H-{^{195}Pt} T-HMQC sequence shown in Fig.2 is the trough for the on-resonance irradiation of the centerband, which has already been reported [51]. This trough stems from the orthogonality of $H^{(2)}_{\text{eff},IS\times\text{rf}}$ and h_0^{rf}, which then fully decouples the ^{1}H-^{14}N dipolar interaction, as explained in the section II-3. When irradiating the centerband, the transfer efficiency is higher in the case of NAV than glycine. This comes from the fact the anisotropic part of the H_{Q2} interaction shifts 7.4 = $(3.21/1.18)^2$ times more the frequency of the NAV centerband, depending on the crystallite orientation. As a result, the pulses on the ^{14}N channel do not irradiate the NAV centerband of all crystallites simultaneously. The maximum transfer efficiency is approximately equal to 20%, like for ^{195}Pt nucleus. The efficiency also exhibits local minima for irradiations close to the spinning sidebands, in agreement with previously reported experimental results [51]. These local minima stem from the creation of ^{14}N 2Q coherences by the third-order Hamiltonian of Eq.S1, which is smaller than the second-order one. Therefore, its effects are more pronounced for large ^{1}H-^{14}N dipolar interactions (see Figs.5 and 8).

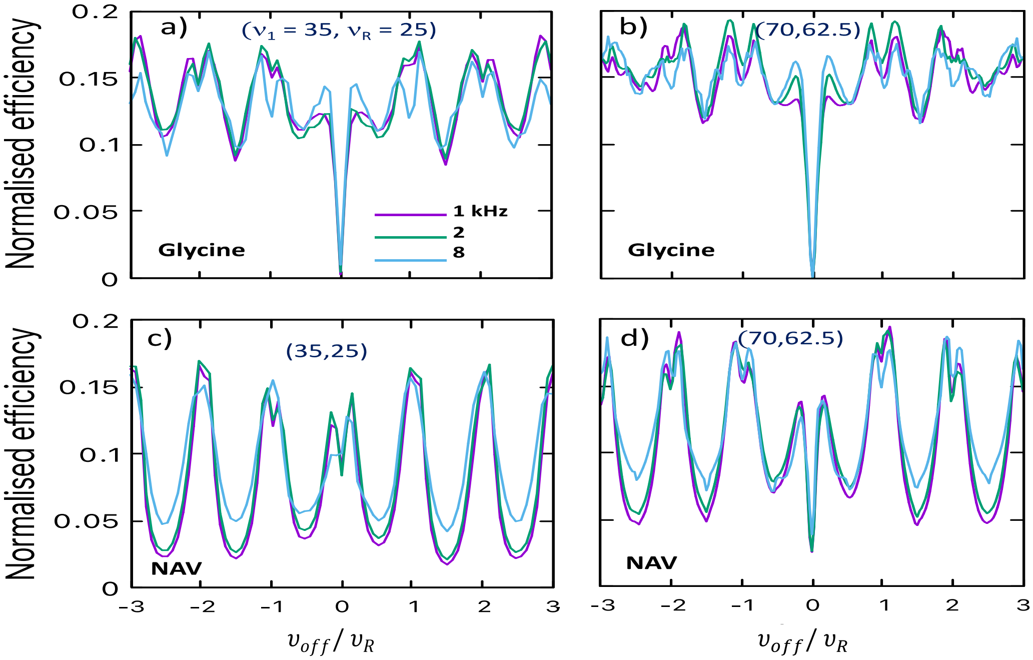

Fig.5. Simulated ^{1}H-{^{14}N^{1Q}} T-HMQC efficiency versus ν_{off} for $\tau_{\mathrm{mix}} = 2$ ms, $|b_{\mathrm{1H\text{-}14N}}|/(2\pi) = 1$, 2 and 8 kHz, and ($\nu_1$, ν_R) = (a,c) (35, 25) and (b,d) (70, 62.5) kHz.

The simulations of the ^{1}H-{^{14}N^{1Q}} T-HMQC build-up curves for different C_Q, ν_R and ν_1 values, shown in Fig.6, indicate that the initial slope increases slightly slower than $\sqrt{\alpha}$. This small discrepancy with Eq.26 stems from the interference with the third-order effective Hamiltonian of Eq.S1, which depletes the ^{1}H transverse magnetization by transforming it into ^{14}N 2Q coherences. The simulated build-up curves, shown in Fig.S1, also indicate that the initial slope of the build-up curves increases for increasing ν_1 amplitude and lower C_Q constant.

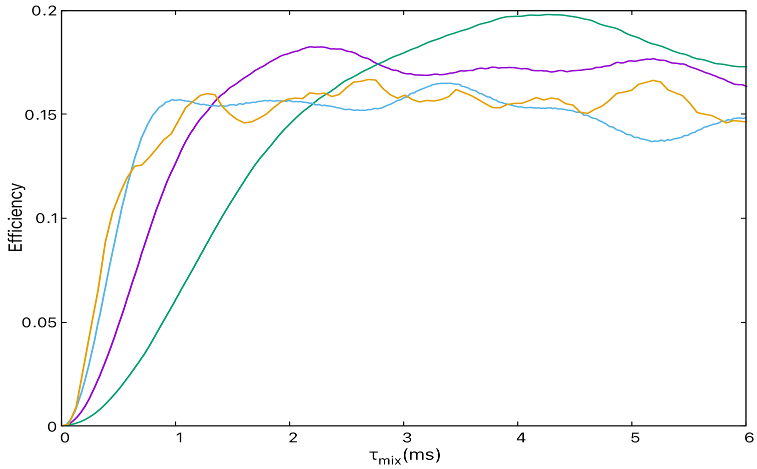

Fig.6. Simulated ^{1}H-{^{14}N^{1Q}} T-HMQC build-up curves for {C_Q (MHz), ν_R (kHz), ν_1 (kHz), α} = {3.21, 62.5, 80, 0.021} (purple), {3.21, 62.5, 40, 0.0053} (green), {0.8, 62.5, 80, 0.085} (blue) and {3.21, 15.625, 80, 0.085} (yellow). The α parameter is calculated with Eq.26 and $|b_{\mathrm{1H\text{-}14N}}|/(2\pi) = 2$ kHz and $\nu_{\mathrm{off}} = \nu_R$.

The simulations of the ^{1}H-{^{14}N^{1Q}} T-HMQC efficiency as function of τ_{mix} and ν_1, shown in Fig.7, also indicate that the optimal recoupling time is roughly inversely proportional to ν_1 in agreement with Eq. 26. Nevertheless, the short T_2' values of ^{1}H nuclei may prevent the use of long τ_{mix} period and low ν_1 amplitude, as shown for ^{195}Pt isotope. Furthermore, for a given τ_{mix} delay, large C_Q and ν_R values require the use of higher rf-field, as predicted by Eq. 26. Nevertheless, at ultra-fast MAS this requirement is offset by the possibility of using longer τ_{mix} delays, and hence smaller ν_1 values, since the T_2' constant of protons increases linearly with ν_R frequency [86].

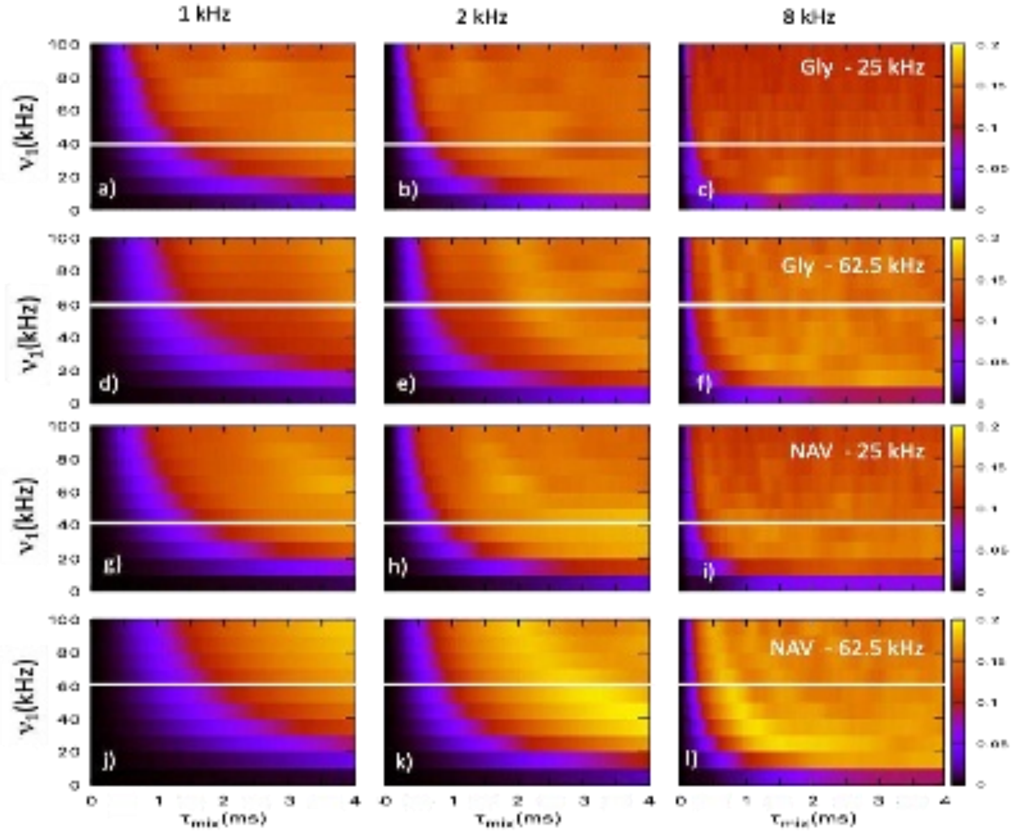

Fig.7. Simulated $^{1}\text{H-}\{^{14}\text{N}^{1Q}\}$ T-HMQC efficiency versus τ_{mix} and ν_1 for (a-f) glycine and (g-l) NAV with ν_R = 25 (a-c,g-i) or 62.5 (d-f,j-l) kHz. The $|b_{\text{1H-14N}}|/(2\pi)$ value is indicated on the top line and $\nu_{\text{off}} = \nu_R$. The horizontal white lines show the rf field that can be accessed with 3.2 (40 kHz) or 1.3 mm (60 kHz) rotors at the ^{14}N Larmor frequency and B_0 = 18.8 T.

^{14}N^{2Q}. The offset profiles of the $^{1}\text{H-}\{^{14}\text{N}^{2Q}\}$ T-HMQC sequence shown in Fig.8 (i) also exhibit a trough for the irradiation of the centerband, particularly for glycine with small H_{Q2} broadening, and (ii) local minima around the spinning sidebands are not detected. In addition, these profiles exhibit additional maxima at the midpoints between the spinning sidebands, $\nu_{\text{off}} = (n + 1/2)\nu_R$, which stem from the third-order effective Hamiltonian (Eq. S2). The build-up of the efficiency at these offsets is slower than for the irradiation at the spinning sidebands since the amplitude of the third-order term is proportional to α, instead of $\sqrt{\alpha} \geq \alpha$ for the second-order terms (compare Figs.S2a and S3).

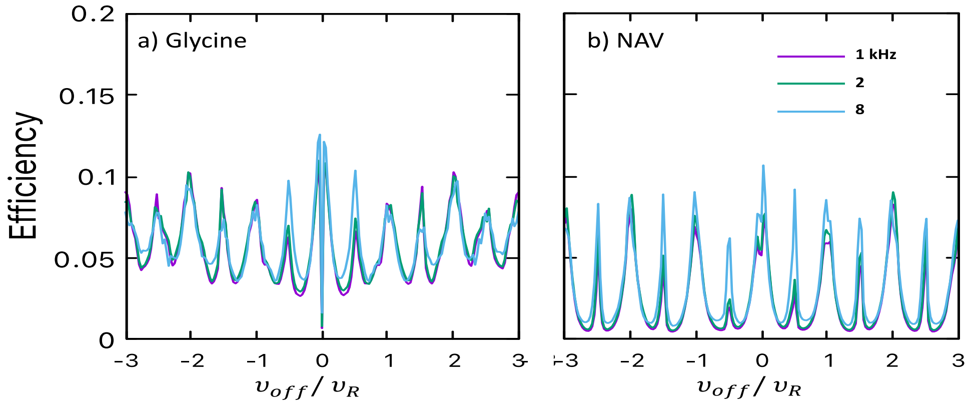

Fig.8. Simulated $^{1}\text{H-}\{^{14}\text{N}^{2Q}\}$ T-HMQC efficiency versus ν_{off} for glycine and NAV with ν_R = 62.5, ν_1 = 70 and $|b_{\text{1H-14N}}|/(2\pi)$ = 1, 2 or 8 kHz.

The initial slope of simulated build-up curves of the ^{1}H-{^{14}N^{2Q}} T-HMQC sequence (Fig.9) also increases with α, but with a slope slightly faster than $\sqrt{\alpha}$ owing to the contribution of the third-order Hamiltonian (Eq.S1) to the build-up of ^{14}N 2Q coherences. Additional simulated build-up curves shown in Fig.S2 also confirm that the initial slope increases with higher rf-field and lower C_Q constant. The simulated efficiency of the ^{1}H-{^{14}N^{2Q}} T-HMQC sequence as function of τ_{mix} delay and ν_1 amplitude, shown in Fig.10 also indicates that the optimal τ_{mix} delay is inversely proportional to ν_1, whereas the optimal rf-field increases with C_Q and ν_R values in agreement with Eq.26. These simulations also indicate that the build-up of ^{14}N 2Q coherences is slightly slower than that of 1Q ones (compare Figs.S1 and S2) and the maximal transfer efficiency is 0.1, twice lower than that of the ^{1}H-{^{14}N^{1Q}} T-HMQC sequence.

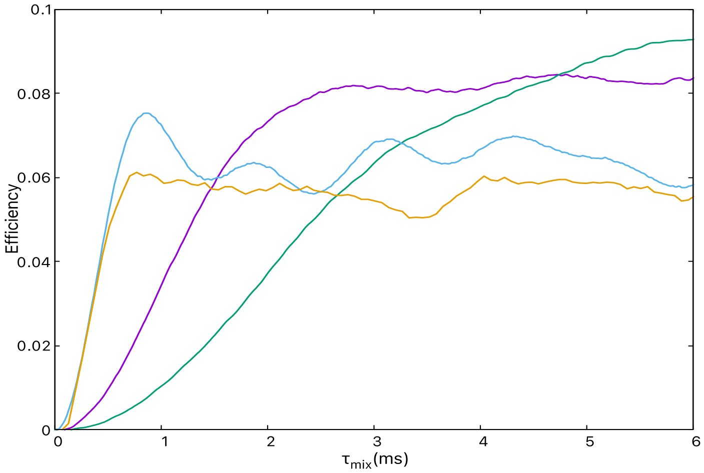

Fig.9. Simulated ^{1}H-{^{14}N^{2Q}} T-HMQC build-up curves for {C_Q (MHz), ν_R (kHz), ν_1 (kHz), α} = {3.21, 62.5, 80, 0.021} (purple), {3.21, 62.5, 40, 0053} (green), {0.8, 62.5, 80, 0.085} (blue) and {3.21, 15.625, 80, 0.085} (yellow). The α parameter is calculated with Eq.26, $|b_{1H\text{-}14N}|/(2\pi)$ = 2 kHz and $\nu_{off} = \nu_R$.

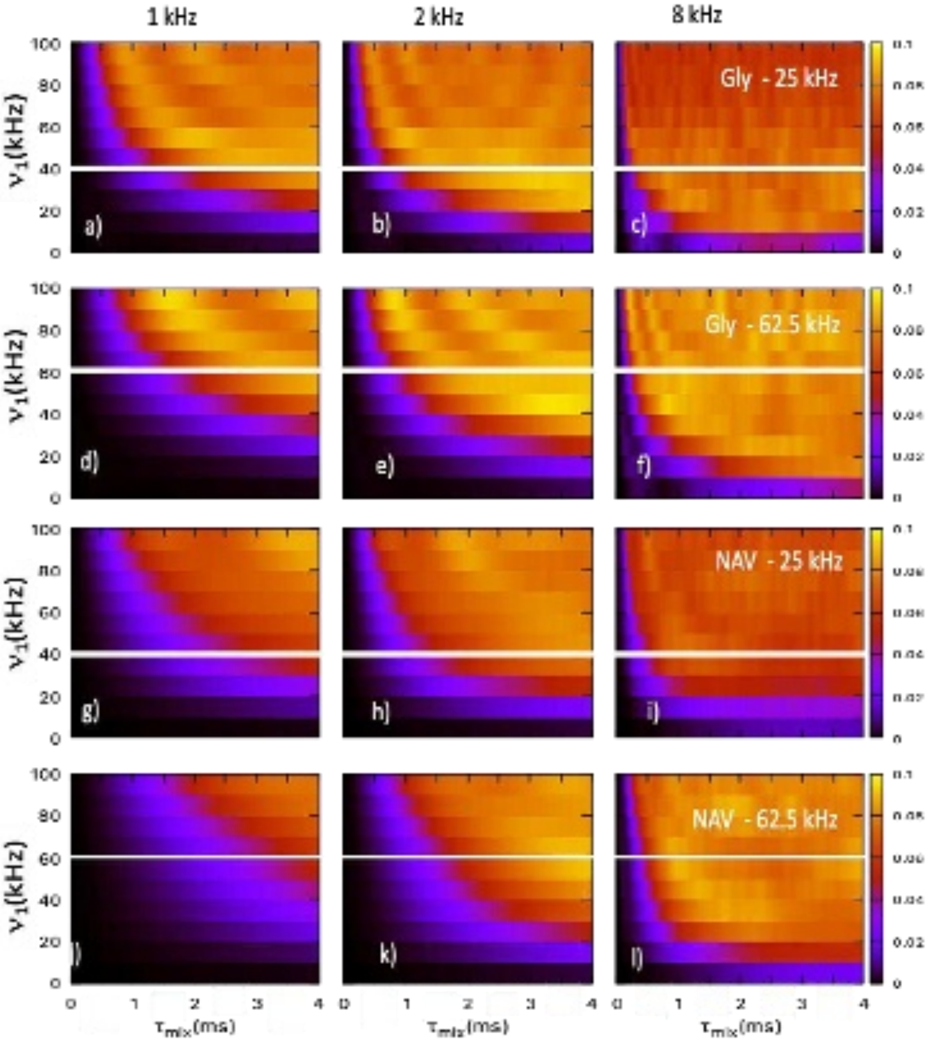

Fig.10. Simulated ^{1}H-{^{14}N^{2Q}} T-HMQC efficiency versus τ_{mix} and ν_1 for (a-f) glycine or (g-l) NAV with ν_R = 25 (a-c,g-i) or 62.5 (d-f,j-l) kHz. The $|b_{\text{1H-14N}}|/(2\pi)$ value is indicated on the first line and $\nu_{\text{off}} = \nu_R$. The horizontal white lines show the rf field that can be accessed with 3.2 (40 kHz) or 1.3 mm (60 kHz) rotors at the ^{14}N Larmor frequency and B_0 = 18.8 T.

III-4. *^{1}H-{^{35}Cl} T-HMQC*

Fig.11 shows the efficiency versus offset of the ^{1}H-{^{35}Cl} T-HMQC sequence with two-, four- and six-step phase cycling, which leads to the selection of 1Q + 3Q, 2Q, and 3Q coherences, respectively. For the sake of clarity, we will mention simultaneously these two aspects: the number of steps for the phase cycling and the corresponding selected coherence orders.

These offset profiles, like those of the ^{1}H-{^{14}N} T-HMQC experiments, exhibit a trough on-resonance owing to the orthogonality of $H^{(2)}_{\text{eff},IS\times\text{rf}}$ and h_0^{rf} in the case of centerband irradiation (section II-4), which decouples the ^{1}H-^{35}Cl dipolar interactions.

With a two-step phase cycling (1Q + 3Q: Fig.11a), local maxima are observed with offsets depending on the rf-field applied to the ^{35}Cl channel. In particular, additional maxima are observed at $\nu_{\text{off}} = \pm\nu_R/3$ for large rf-fields. They stem from the fourth-order effective Hamiltonian, which then contributes to the indirect detection of 1Q and 3Q ^{35}Cl coherences. These local maxima are also observed with a six-step phase cycling (3Q: Fig.11d), whereas the offset profile with four-step phase cycling exhibit local maxima at $\nu_{\text{off}} = \pm\nu_R/2$ (2Q: Fig.11c) since the third-order effective Hamiltonian contributes to the indirect detection of ^{35}Cl 2Q coherences. The transfer efficiencies of the ^{1}H-{^{35}Cl} T-HMQC sequence with two-, four- and six-step phase cycling are approximately equal to 15, 7 and 3%, respectively. In the case of a two-step phase cycling, the 1Q-ST signal is two to three times more intense than that of 1Q-CT, which has an intensity comparable to that of 3Q.

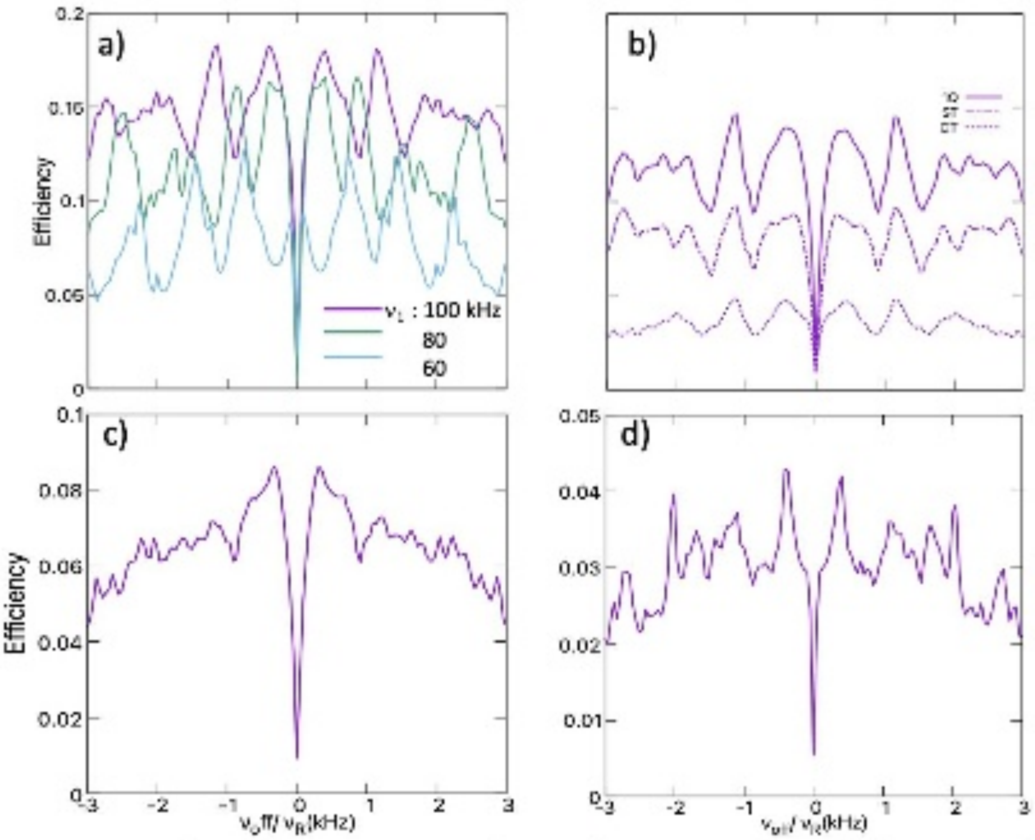

Fig.11. Simulated ^{1}H-{^{35}Cl} T-HMQC efficiency versus the ν_{off}/ν_R ratio with: (a) 1Q + 3Q (two-step phase cycling with ν_1 = 60, 80 or 100 kHz), (b) 1Q-(CT+ST), 1Q-CT and 1Q-ST, (c) 2Q-ST (four-step phase cycling), (d) 3Q (six-step phase cycling). For the simulations of panels b-d, ν_1 = 100 kHz. B_0 = 18.8 T, ν_R = 62.5 kHz, $|b_{1H\text{-}35Cl}|/(2\pi)$= 0.58, C_Q = 1950 kHz, η_Q = 0.66 and τ_{mix} = 1.7 ms.

IV. Experimental demonstrations

IV-1. *Samples and experimental conditions*

Cisplatin, transplatin and L-histidine·HCl·H_2O (referred to as "histidine" hereafter) were purchased from Merck. An equimolar mechanical mixture of cis- and transplatin was prepared and packed into a 1.3 mm rotor, which was stored in the air during three years [62]. We chose this aged mixture, in order to demonstrate the possibility to resolve using ^{1}H-{^{195}Pt} T-HMQC experiment the ^{195}Pt resonances of cis- and trans-platin as well as impurities. Owing to the robustness of the T-HMQC sequence to rf-field inhomogeneity, the sample volume in the rotor was not restricted with spacers.

All experiments were performed at B_0 = 18.8 T on a Bruker BioSpin Avance NEO spectrometer equipped with a double-resonance ^{1}H/X 1.3 mm MAS probe. The angle between the rotor axis and $\boldsymbol{B}_0$ field was carefully adjusted at the magic angle, whereas the MAS frequency was regulated using a MAS-III pneumatic unit with a standard deviation of 2.45 Hz (Fig.S4).

The ^{1}H rf-field for the π/2 and π pulses was set to ν_{1H} = 208 kHz. A pre-saturation consisting of five π/2 pulses was applied on the ^{1}H channel in order to use recycling delays shorter than five times the longitudinal relaxation time of protons T_1(^{1}H).

The ^{1}H isotropic chemical shifts were referenced to tetramethylsilane (TMS) using the signal of the CH_2 group of adamantane at 1.85 ppm as a secondary reference. The ^{195}Pt isotropic chemical shifts were indirectly referenced using the previously published relative NMR frequencies [87].

The aged mixture of cisplatin and transplatin was spun at ν_R = 62 and 64 kHz. The ^{1}H-{^{195}Pt} T-HMQC 2D spectra were recorded using two identical rectangular pulses with τ_{mix} = 516 μs and ν_1 = 186 kHz applied with a ^{195}Pt carrier frequency corresponding to a shift of δ_{off} = −1810 or −1850 ppm. The other experimental parameters, including the number of t_1 increments, N_1, the number of scans, NS, the recycling delay, τ_{RD}, the spectral width of the indirect dimension, SW_1, and the total experimental time, T_{exp}, are listed in the Table 1.

The histidine sample was spun at ν_R = 50 kHz. The ^{1}H-{^{14}N} T-HMQC spectra result from the averaging of NS = 8 transients, for each of N_1 = 128 t_1 increments in the case of 2D spectra, with $SW_1 = \nu_R = \nu_1$ = 50 kHz, τ_{RD} = 1 s, τ_{mix} = 540 µs and ν_1 = 50 kHz.

Table 1. Experimental parameters (N_1, τ_{RD}, NS, ν_R, SW$_1$) of the ^{1}H-{^{195}Pt} T-HMQC 2D spectra along with the intensity of the cross-peak between δ_{1H} = 4 ppm and δ_{195Pt} = −1795 ppm and the root-mean-square (rms) amplitude of the noise.

Fig.	N_1	τ_{RD} /s	NS	ν_R /kHz	SW_1 /kHz	T_{exp} /min	Intensity[a]	Noise[b]	$\frac{\text{Intensity}}{\text{Noise}}$
12a	60	20	16	64	64	322	1	1	1
12b	60	1	288	64	64	324	1.5	4	0.375
14a	240	10	8	64	256	321	0.66	0.7	0.94
14b	40[c]	16	16	62	62	172	0.77	0.5	1.54

[a] Normalized with respect to the cross-peak intensity in Fig.12a. [b] Measured in the F_1 slices devoid of signal with δ_{1H} = 32 ppm and normalized with respect to that in Fig.12a. [c] Selected using a bi-exponentially decaying sampling [88].

IV-2. ^{1}H-{^{195}Pt} T-HMQC

The ^{1}H-{^{195}Pt} T-HMQC experiment was tested on a mixture of cis- and transplatin, for which we recorded three years ago the ^{1}H-{^{195}Pt} *D*-HMQC spectra [68]. In these square planar complexes, the ^{195}Pt nuclei are subject to a CSA ≈ 1.5 MHz at 18.8 T and a dipolar coupling $|b_{1H\text{-}195Pt}|/(2\pi)$ = 2 kHz [59,89].

The carrier frequency on the ^{195}Pt channel was applied at a frequency close to the centerband of the cisplatin and the first spinning sideband of transplatin since according to simulations of Fig.2, these conditions are expected to result in a maximal efficiency. We optimized both the τ_{mix} and ν_1 parameters (Fig.S5). As the T_2' values of cis- and trans-platin are equal to 1.6 ms, recoupling conditions corresponding to long recoupling time and low rf-power, such as τ_{mix} ≈ 3 ms and ν_1 ≈ 50 kHz, yielded a poor efficiency, as predicted by simulations of Fig.4d and we had to use a short recoupling time and hence a high rf-power. The ^{1}H-{^{195}Pt} T-HMQC 2D spectra of Figs. 12 and 14 were recorded using τ_{mix} = 516 µs and ν_1 = 186 kHz.

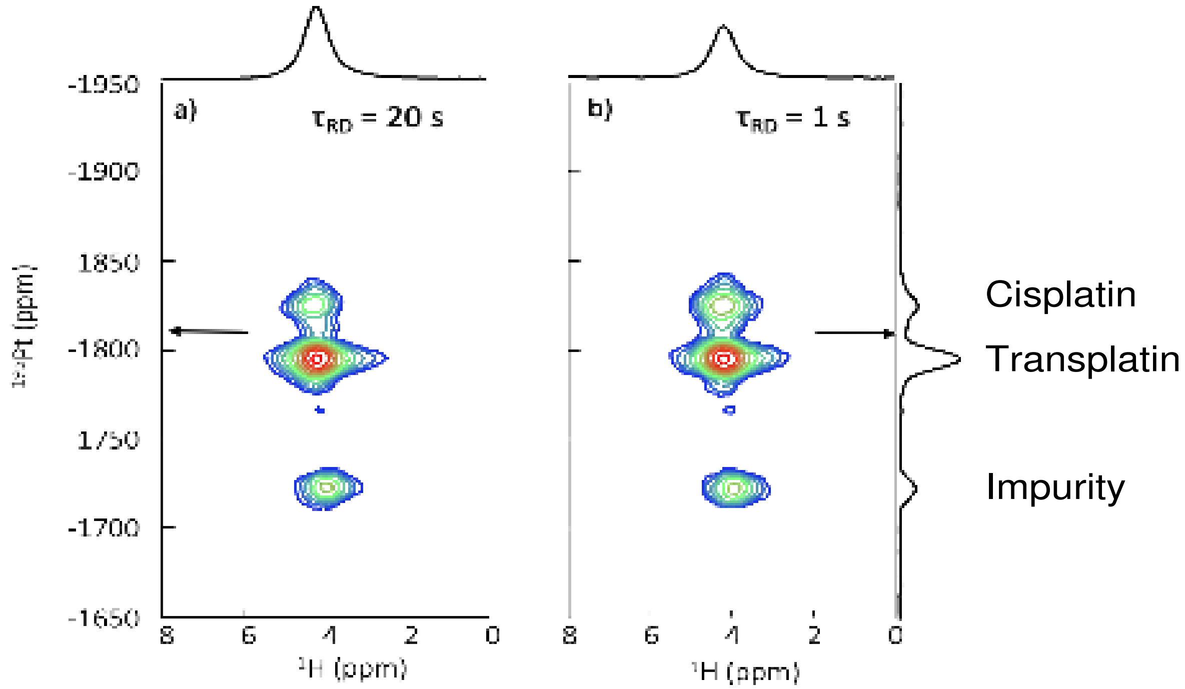

Fig.12. ^{1}H-{^{195}Pt} T-HMQC 2D spectra of an aged mixture of cis- and transplatin recorded at 18.8 T with ν_R = 64 kHz, δ_{off} = = −1810 ppm (indicated with arrows), $SW_1 = \nu_R$ and τ_{RD} = (a) 20 or (b) 1 s.

The $T_1(^1H)$ constants of cis- and trans-platin are equal to 12 and 17 s, respectively [59]. We recorded the ^1H-{^{195}Pt} T-HMQC 2D spectrum with $SW_1 = \nu_R$ and $\tau_{RD} = 20$ s corresponding to $1.2T_1(^1H)$ for cisplatin (Fig.12a). This recycling delay is close to that yielding maximal sensitivity when the thermal noise is dominating [90]. We also recorded the same spectrum with $\tau_{RD} = 1$ s since $\tau_{RD} < T_1(^1H)$ limits the t_1-noise, which is proportional to the signal intensity (Fig.12b) [41]. Nevertheless, the 2D spectra of Fig.12 do not exhibit significant t_1-noise in agreement with the previously reported ^1H-{^{14}N} T-HMQC 2D spectra [51] and the largest SNR and sensitivity were obtained for $\tau_{RD} = 20$ s.

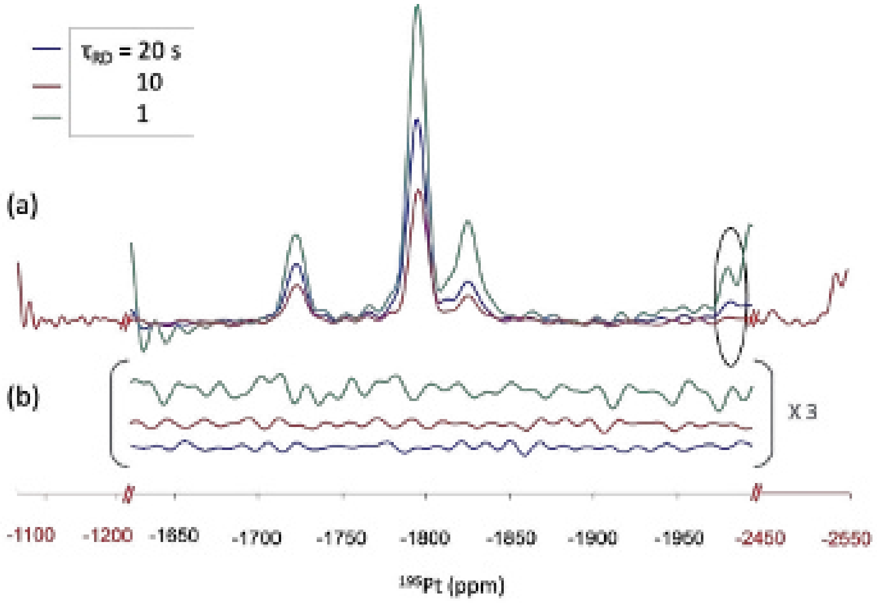

Fig.13. 1D F_1 slices at $\delta_{1H} = 4$ (a) or 32 (b) ppm of the 2D ^1H-{^{195}Pt} T-HMQC spectra shown in Figs.12 and 14 of an aged mixture of cis- and transplatin recorded at 18.8 T with $\nu_R = 64$ kHz and $\delta_{off} = -1810$ ppm. The thermal noise has been scaled up by a factor of three in (b). The red slice in (a) is extracted from the 2D spectrum of Fig.14a with $SW_1 = 4\nu_R$, and hence, additional regions corresponding to the edges of the spectra are also displayed to show the axial peaks. The oval indicates the region containing the impurity signal at –1990 ppm.

The cross-peaks detected on the 2D spectra of Fig.12 demonstrate that T-HMQC can be used for the indirect detection of spin-1/2 nuclei subject to large CSA, such as ^{195}Pt. Three peaks are resolved at the shifts –1723, –1795 and –1825 ppm. Furthermore, as seen in Fig.13, axial peaks, which do not evolve under ^{195}Pt isotropic chemical shifts, are detected at the edges of the T-HMQC 2D spectra. These axial peaks, which are rejected at the edges of the 2D spectra by the States-TPPI procedure [91], stem from the evolution under the Bloch-Siegert shift (Eq. 9). Indeed, the amplitude of this term is constant, and as its phase does not depend of that of the rf pulse, these peaks cannot be eliminated by the phase cycling.

The isotropic chemical shifts of the different signals, δ_{iso}, were determined by recording two T-HMQC spectra at two slightly different MAS frequencies, $\nu_{R,1}$ and $\nu_{R,2}$,

$$\delta_{\text{iso}} = \delta(\nu_{R,i}) - \frac{10^6 n \nu_{R,i}}{\nu_0} \tag{35}$$

where $\delta(\nu_{R,i})$ is the shift measured at $\nu_{R,i}$, and n the order of the spinning sideband, which can be determined as

$$n = \nu_0 \frac{\delta(\nu_{R,1}) - \delta(\nu_{R,2})}{10^6(\nu_{R,1} - \nu_{R,2})}\,. \tag{36}$$

The δ_{iso} values measured from the T-HMQC 2D spectra acquired at $\nu_R = 62$ and 64 kHz are listed in Table 2. The shifts –1825 and –2167 ppm are assigned to cis- and transplatin complexes, respectively [59,68,89]. Additional ^{195}Pt resonances with $\delta_{iso} = -1990$ and –2095 ppm are detected. They are assigned to impurities formed during the aging of the mixture. The resonance with $\delta_{iso} = -1990$ ppm is better seen in the spectrum acquired at $\nu_R = 62$ kHz since it partly overlaps with the axial peak at $\nu_R = 64$ kHz (compare Figs.13a and 14b). As seen in Fig.15, the signal with δ_{iso} = –2095 ppm is more intense than that with δ_{iso} = –1990 ppm. Therefore, these impurities with δ_{iso} = –1990 and –2095 ppm could tentatively be assigned to mono-aquated cis- and transplatin complexes, $[PtCl(NH_3)_2(H_2O)]^+$ [92].

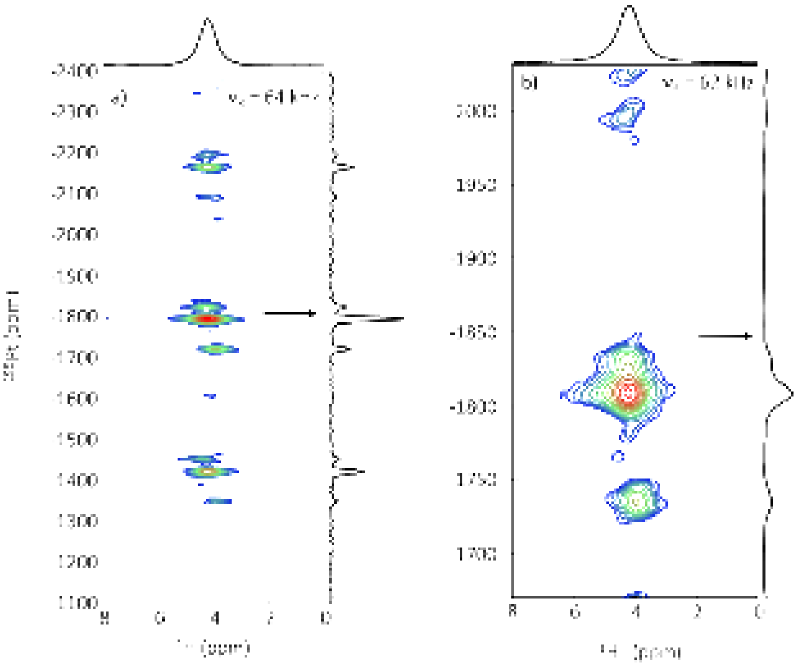

Fig.14. ^{1}H-{^{195}Pt} T-HMQC 2D spectra of an aged mixture of trans- and cis-platin recorded at 18.8 T with (a) ν_R = 64 kHz, δ_{off} = –1810 ppm, $SW_1 = 4\nu_R$ and τ_{RD} = 10 s, and (b) ν_R = 62 kHz , δ_{off} = –1850 ppm, $SW_1 = \nu_R$ and τ_{RD} = 16 s.

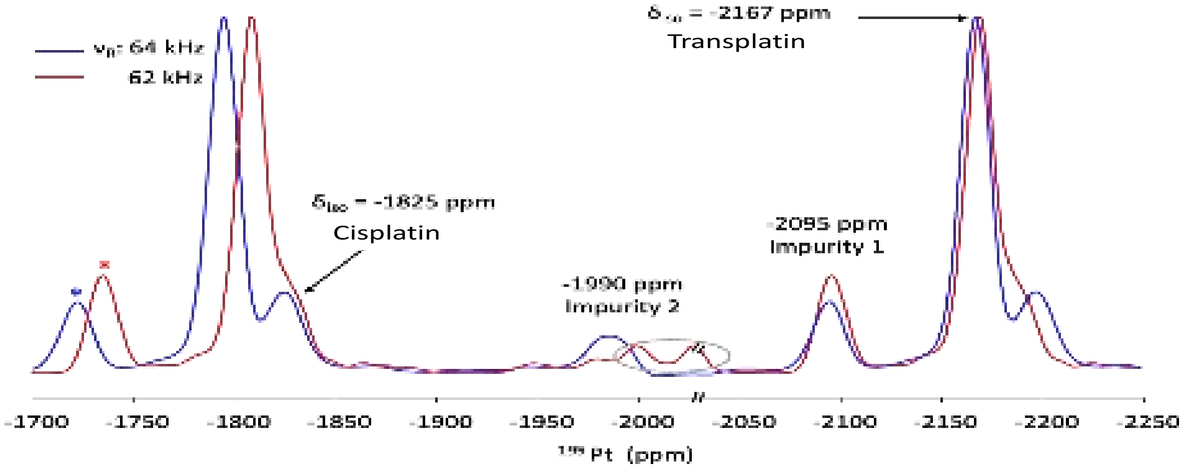

Fig.15. 1D F_1 slices at δ_{1H} = 4 ppm duplicated over $2\nu_R$ of the 2D ^{1}H{^{195}Pt} T-HMQC spectra shown in Figs.**12a** and **14b** of an aged mixture of cis- and transplatin recorded at 18.8 T with ν_R = 64 and 62 kHz and δ_{off} = –1810 or –1850 ppm, respectively. The centerbands are identified by their δ_{iso} values, and the symbol * denotes the spinning sidebands. The oval indicates the axial peak on the edge of the spectrum.

Table 2. Shifts of ^{195}Pt resonances along the F_1 dimension of the ^{1}H-{^{195}Pt} T-HMQC 2D spectra of an aged mixture of cis- and transplatin acquired at ν_R = 62 and 64 kHz along with the δ_{iso} values calculated with Eq.35.

Species	δ(64 kHz) /ppm	δ(62 kHz) /ppm	δ_{iso} /ppm
impurity-1	–1723	–1735	–2095
transplatin	–1795	–1807	–2167
cisplatin	–1825	–1825	–1825
impurity-2	–1990	–1990	–1990

IV-3. *^{1}H-{^{14}N} T-HMQC*

Fig.16a and b show the ^{1}H-{^{14}N^{1Q}} and ^{1}H-{^{14}N^{2Q}} T-HMQC 2D spectra of histidine. Fig.16c-e compare the ^{14}N slices of these 2D spectra for the three nitrogen sites, NH_3^+, N$^{\tau}$ and N$^{\pi}$, which are subject to similar quadrupole interactions, {C_Q (MHz), η_Q} = {1.25, 0.35}, {1.29, 0.94} and {1.56, 0.26} [93]. The ^{14}N^{2Q} frequencies were divided by a factor of two and no line broadening was applied to facilitate the comparison of the resolution with ^{14}N^{1Q}. The ^{14}N^{2Q} resonances are slightly narrower than the ^{14}N^{1Q} ones in spite of the high stability of the MAS frequency and the careful set-up of the magic angle. This result indicates that the ^{1}H-{^{14}N^{2Q}} T-HMQC 2D spectra benefit from a slightly improved resolution because they are not subject to H_{Q1} interaction.

The efficiency of the ^{1}H-{^{14}N^{1Q}} and ^{1}H-{^{14}N^{2Q}} T-HMQC experiments was optimized by adjusting τ_{mix} and ν_1 parameters, as shown in Fig.S6. The ^{14}N^{2Q} version requires a higher rf-field than the ^{14}N^{1Q} one. This difference could stem from the contribution of the third-order Hamiltonian to the creation of 2Q coherences. In practice, we used the highest rf-field on the ^{14}N channel compatible with the probe specifications. Under this condition, the experimental signal intensities of the ^{1}H-{^{14}N^{1Q}} and ^{1}H-{^{14}N^{2Q}} T-HMQC experiments are comparable (Figs.16c-e), whereas simulations predicted higher transfer efficiencies for the former technique. The decreased signal intensity of the ^{1}H-{^{14}N^{1Q}} T-HMQC experiment can stem from its higher sensitivity to instabilities of the MAS frequency and the magic angle.

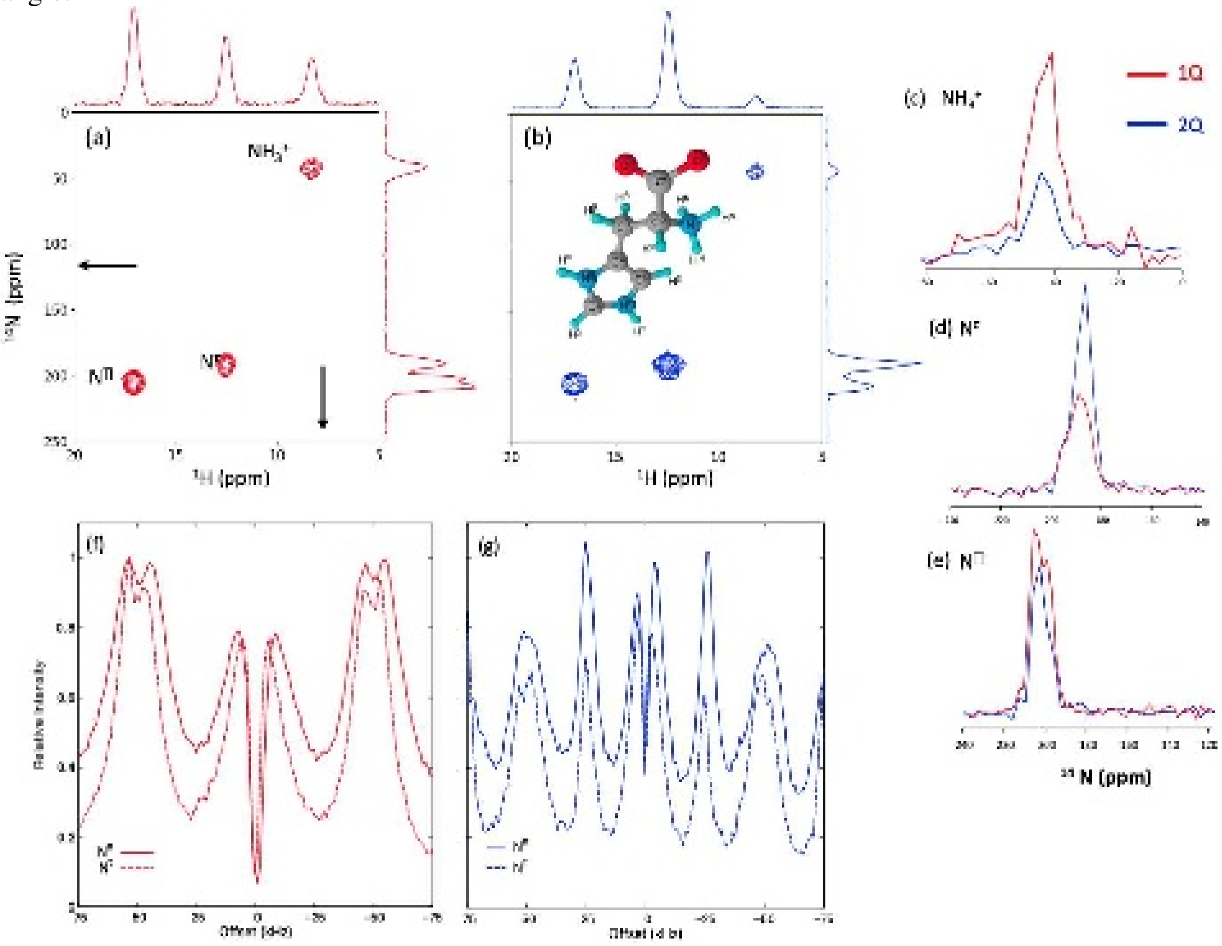

Fig.16. (a,f) ^{1}H-{^{14}N^{1Q}} and (b,g) ^{1}H-{^{14}N^{2Q}} T-HMQC data on histidine at B_0 = 18.8 T with ν_R = 50 kHz and τ_{mix} = 540 µs. (a) ^{1}H-{^{14}N^{1Q}} and (b) ^{1}H-{^{14}N^{2Q}} 2D spectra along with their ^{1}H and ^{14}N sum projections. The carrier frequencies are shown in (a) with arrows. (c-e) ^{14}N slices of these 2D spectra for (c) NH_3^+, (d) N$^{\tau}$ and (e) N$^{\pi}$ sites without line-broadening. For the sake of comparison, the ^{14}N^{2Q} frequencies are divided by 2. (f,g) Efficiency of (f) ^{1}H-{^{14}N^{1Q}} and (g) ^{1}H-{^{14}N^{2Q}} T-HMQC 1D experiments versus ν_{off} for N$^{\pi}$ and N$^{\tau}$ sites.

The offset profiles of the ^{1}H-{^{14}N^{1Q}} and ^{1}H-{^{14}N^{2Q}} T-HMQC experiments shown in Figs.16f and g, respectively, agree with the simulated ones of Figs.5 and 8. They exhibit a trough for the irradiation of the centerband. For the $^{14}N^{1Q}$ version, the maximal intensity is obtained when irradiating near the spinning sidebands. Nevertheless, local minima for the on-resonance irradiation of the spinning sidebands are detected since this condition favors the creation of ^{14}N 2Q coherences by the third-order Hamiltonian. In the case of the $^{14}N^{2Q}$ experiment, a maximal intensity is achieved at the frequencies of the spinning sidebands and their midpoints.

IV-4. *^1H-{^{35}Cl} T-HMQC*

Fig.17 displays the ^1H-{$^{35}Cl^{1Q+3Q}$} T-HMQC 2D spectra of histidine, which contains a single ^{35}Cl site with C_Q = 1.95 MHz and η_Q = 0.66 [61]. The two-step phase cycling of one of the TRAPDOR pulse selects the 1Q-CT, 1Q-ST and 3Q coherences during the t_1 period [62]. These transitions can be distinguished by changing the offset since the dependence of the resonance frequency of 3Q coherences with the offset, ν_{off}, is 4-fold larger than for the 1Q coherences. This 'strange' effect comes from the States-TPPI acquisition used here with a phase shift of 90°. This corresponds to an effective rotation of 270° = -90° for the 3Q coherence in the rotating frame, and hence to a negative frequency shift of $-\nu_{off}$. Therefore, the combined effects make the position of the 3Q coherence shifting by $4\nu_{off}$.

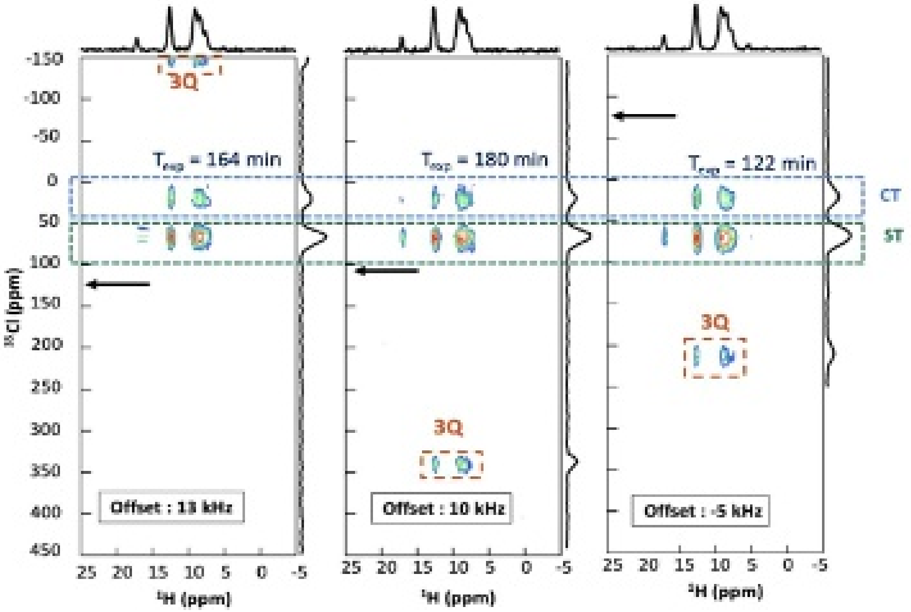

Fig.17. ^1H-{$^{35}Cl^{1Q+3Q}$} T-HMQC 2D spectra of histidine at B_0 = 18.8 T with ν_R = 50 kHz and different ^{35}Cl carrier frequencies indicated by arrows.

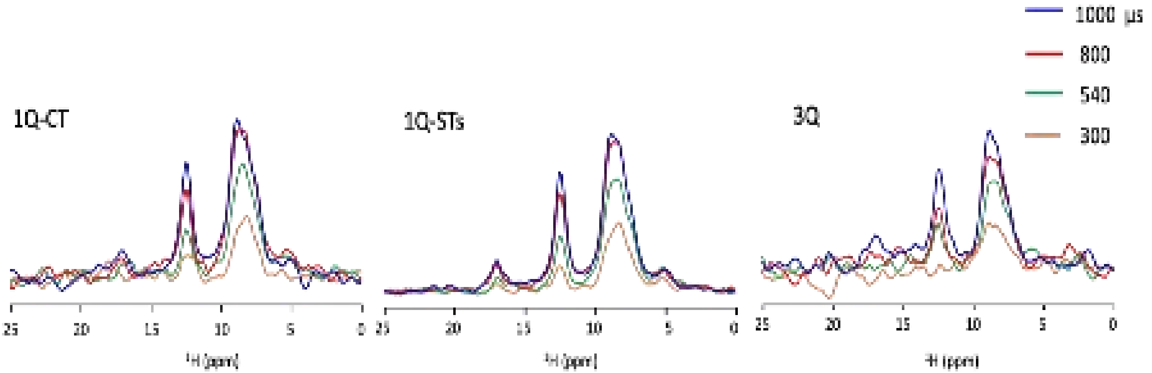

Fig.18. ^1H-{$^{35}Cl^{1Q+3Q}$} T-HMQC spectra of histidine at B_0 = 18.8 T with ν_R = 50 kHz and υ_{off} = −5 kHz. For each detected coherence, we show five ^1H slices corresponding to τ_{mix} = 300, 500, 800 and 1000 µs (as indicated).

Fig.18 shows similar build-up for the three resonances with an optimal recoupling time $\tau_{mix} \approx 900$ µs. In agreement with the simulations, 1Q-CT and 3Q resonances exhibit similar intensities. Theoretically, these intensities should be two-fold lower than that of 1Q-ST (Fig.11b). However, they all present similar experimental intensities, because the intensity of the 1Q-ST strongly depends on the adjustment of the magic angle.

V. Conclusion

We have demonstrated for the first time the possibility to detect via protons the signal of spin-1/2 nuclei subject to large CSA using the T-HMQC sequence. We have shown that this experiment allows the indirect observation of ^{14}N 2Q coherences, which is more robust than that of 1Q coherences, which are broadened by the first-order quadrupole interaction. In practice, the ^{1}H-{^{14}N^{2Q}} T-HMQC technique benefits from a better resolution than the ^{14}N^{1Q} variant, whereas both experiments offer similar sensitivities. We have also introduced effective Hamiltonians to describe the spin dynamics during the ^{1}H-{I} T-HMQC sequences with $I = 1/2$, 1 and 3/2. These Hamiltonians (i) explain the importance of the adiabaticity parameter for the TRAPDOR and T-HMQC experiments, and (ii) highlight the contribution of terms with order higher than two, notably for the creation of multiple-quantum coherences. Using high MAS frequencies, ν_R, is beneficial for these ^{1}H-{I} T-HMQC experiments derived from the ^{1}H spin echo sequence. Indeed, on one hand the efficiency is inverse proportional to $\sqrt{\nu_R}$, but on the other hand high MAS frequencies enhance the ^{1}H resolution and lengthen the T_2' value. Moreover, the small rotor diameters associated to high MAS frequencies allow using larger rf-fields which increase the efficiency proportionally.

Actually, from the experiments presented in this article, and from others not shown, we have always observed experimentally similar efficiencies with *D*- and T-HMQC experiments, whatever the MAS spinning speed: moderate of fast.

Author's contribution. All authors contributed equally to this work.

Supplementary Material. Third-order effective Hamiltonian for I = 1 (Eq. S1 and S2); Simulated ^{1}H-{^{14}N} T-HMQC build-up curves; MAS frequency distribution; Experimental optimization of ^{1}H-{^{195}Pt} and ^{1}H-{^{14}N} T-HMQC 2D experiments.

Acknowledgments. Chevreul Institute (FR 2638), Ministère de l'Enseignement Supérieur, de la Recherche et de l'Innovation, Hauts-de-France Region, and FEDER are acknowledged for supporting and funding partially this work. Financial support from the IR-RMN-THC FR-3050 CNRS for conducting the research is gratefully acknowledged. OL and RB acknowledges financial support contract ANR-18-CE08-0015-01 (ThinGlass) and T-UEPEARL-20-005-LAFON-HAMDOUNA (NMR-MECA-DRUG). IH and ZG acknowledge the support by the National Science Foundation through NSF/DMR-1644779 and the State of Florida to the National High Magnetic Field Laboratory.

References

[1] B. Reif, S.E. Ashbrook, L. Emsley, M. Hong, Solid-state NMR spectroscopy, Nat Rev Methods Primers. 1 (2021) 1–23. https://doi.org/10.1038/s43586-020-00002-1.

[2] R.W. Schurko, Acquisition of Wideline Solid-State NMR Spectra of Quadrupolar Nuclei, EMagRes. (2011). https://doi.org/10.1002/9780470034590.emrstm1199.

[3] R.W. Schurko, Ultra-wideline solid-state NMR spectroscopy., Accounts of Chemical Research. 46 (2013) 1985–1995. https://doi.org/10.1021/ar400045t.

[4] A.J. Pell, G. Pintacuda, C.P. Grey, Paramagnetic NMR in solution and the solid state, Progress in Nuclear Magnetic Resonance Spectroscopy. 111 (2019) 1–271. https://doi.org/10.1016/j.pnmrs.2018.05.001.

[5] S.E. Ashbrook, S. Sneddon, New Methods and Applications in Solid-State NMR Spectroscopy of Quadrupolar Nuclei, J. Am. Chem. Soc. 136 (2014) 15440–15456. https://doi.org/10.1021/ja504734p.

[6] I. Hung, A.J. Rossini, R.W. Schurko, Application of the Carr−Purcell Meiboom−Gill Pulse Sequence for the Acquisition of Solid-State NMR Spectra of Spin-1/2 Nuclei, J. Phys. Chem. A. 108 (2004) 7112–7120. https://doi.org/10.1021/jp0401123.

[7] R. Siegel, T.T. Nakashima, R.E. Wasylishen, Application of Multiple-Pulse Experiments to Characterize Broad NMR Chemical-Shift Powder Patterns from Spin-1/2 Nuclei in the Solid State, J. Phys. Chem. B. 108 (2004) 2218–2226. https://doi.org/10.1021/jp031048c.

[8] F.H. Larsen, H.J. Jakobsen, P.D. Ellis, N.Chr. Nielsen, Sensitivity-Enhanced Quadrupolar-Echo NMR of Half-Integer Quadrupolar Nuclei. Magnitudes and Relative Orientation of Chemical Shielding and Quadrupolar Coupling Tensors, The Journal of Physical Chemistry A. 101 (1997) 8597–8606.

[9] K.J. Harris, A. Lupulescu, B.E.G. Lucier, L. Frydman, R.W. Schurko, Broadband adiabatic inversion pulses for cross polarization in wideline solid-state NMR spectroscopy., Journal of Magnetic Resonance (San Diego, Calif. : 1997). 224 (2012) 38–47. https://doi.org/10.1016/j.jmr.2012.08.015.

[10] K.J. Harris, S.L. Veinberg, C.R. Mireault, A. Lupulescu, L. Frydman, R.W. Schurko, Rapid Acquisition of ^{14}N Solid-State NMR Spectra with Broadband Cross Polarization, Chemistry – A European Journal. 19 (2013) 16469–16475. https://doi.org/10.1002/chem.201301862.

[11] T. Kobayashi, F.A. Perras, T.W. Goh, T.L. Metz, W. Huang, M. Pruski, DNP-Enhanced Ultrawideline Solid-State NMR Spectroscopy: Studies of Platinum in Metal–Organic Frameworks, J. Phys. Chem. Lett. 7 (2016) 2322–2327. https://doi.org/10.1021/acs.jpclett.6b00860.

[12] D.A. Hirsh, A.J. Rossini, L. Emsley, R.W. Schurko, ^{35}Cl dynamic nuclear polarization solid-state NMR of active pharmaceutical ingredients, Phys. Chem. Chem. Phys. 18 (2016) 25893–25904. https://doi.org/10.1039/C6CP04353D.

[13] I. Hung, R.W. Schurko, Solid-State ^{91}Zr NMR of Bis(cyclopentadienyl)dichlorozirconium(IV), J. Phys. Chem. B. 108 (2004) 9060–9069. https://doi.org/10.1021/jp040270u.

[14] L.A. O'Dell, A.J. Rossini, R.W. Schurko, Acquisition of ultra-wideline NMR spectra from quadrupolar nuclei by frequency stepped WURST–QCPMG, Chemical Physics Letters. 468 (2009) 330–335. https://doi.org/10.1016/j.cplett.2008.12.044.

[15] L.A. O'Dell, R.W. Schurko, Fast and simple acquisition of solid-state ^{14}N NMR spectra with signal enhancement via population transfer., Journal of the American Chemical Society. 131 (2009) 6658–6659. https://doi.org/10.1021/ja901278q.

[16] A.W. MacGregor, L.A. O'Dell, R.W. Schurko, New methods for the acquisition of ultra-wideline solid-state NMR spectra of spin-1/2 nuclides., Journal of Magnetic Resonance (San Diego, Calif. : 1997). 208 (2011) 103–13. https://doi.org/10.1016/j.jmr.2010.10.011.

[17] D. Massiot, I. Farnan, N. Gautier, D. Trumeau, a Trokiner, J.P. Coutures, ^{71}Ga and ^{69}Ga nuclear magnetic resonance study of beta-Ga_2O_3: resolution of four- and six-fold coordinated Ga sites in static conditions., Solid State Nuclear Magnetic Resonance. 4 (1995) 241–8.

[18] S. Cavadini, A. Lupulescu, S. Antonijevic, G. Bodenhausen, Nitrogen-14 NMR Spectroscopy Using Residual Dipolar Splittings in Solids, J. Am. Chem. Soc. 128 (2006) 7706–7707. https://doi.org/10.1021/ja0618898.

[19] Z. Gan, Measuring amide nitrogen quadrupolar coupling by high-resolution ^{14}N/^{13}C NMR correlation under magic-angle spinning., Journal of the American Chemical Society. 128 (2006) 6040–6041. https://doi.org/10.1021/ja0578597.

[20] S. Cavadini, S. Antonijevic, A. Lupulescu, G. Bodenhausen, Indirect detection of nitrogen-14 in solids via protons by nuclear magnetic resonance spectroscopy., Journal of Magnetic Resonance (San Diego, Calif. : 1997). 182 (2006) 168–72. https://doi.org/10.1016/j.jmr.2006.06.003.

[21] J.P. Yesinowski, E.A. Hill, Wide-Line ^{14}N NMR in Solids, in: Solid-State NMR Spectroscopy of Inorganic Materials, American Chemical Society, 1999: pp. 358–376. https://doi.org/10.1021/bk-1999-0717.ch013.

[22] S. Antonijevic, N. Halpern-Manners, Probing amide bond nitrogens in solids using ^{14}N NMR spectroscopy., Solid State Nuclear Magnetic Resonance. 33 (2008) 82–87. https://doi.org/10.1016/j.ssnmr.2008.04.006.

[23] S. Cavadini, A. Abraham, G. Bodenhausen, Coherence transfer between spy nuclei and nitrogen-14 in solids., Journal of Magnetic Resonance (San Diego, Calif. : 1997). 190 (2008) 160–164. https://doi.org/10.1016/j.jmr.2007.10.008.

[24] Z. Gan, J.-P. Amoureux, J. Trébosc, Proton-detected ^{14}N MAS NMR using homonuclear decoupled rotary resonance, Chemical Physics Letters. 435 (2007) 163–169. https://doi.org/10.1016/j.cplett.2006.12.066.

[25] S. Cavadini, A. Abraham, G. Bodenhausen, Proton-detected nitrogen-14 NMR by recoupling of heteronuclear dipolar interactions using symmetry-based sequences, Chemical Physics Letters. 445 (2007) 1–5. https://doi.org/10.1016/j.cplett.2007.07.060.

[26] A. Brinkmann, A.P.M. Kentgens, Proton-Selective ^{17}O-^{1}H Distance Measurements in Fast Magic-Angle-Spinning Solid-State NMR Spectroscopy for the Determination of Hydrogen Bond Lengths, J. Am. Chem. Soc. 128 (2006) 14758–14759.

[27] O. Lafon, Q. Wang, B. Hu, F. Vasconcelos, J. Trébosc, S. Cristol, F. Deng, J.-P. Amoureux, Indirect Detection via Spin-1/2 Nuclei in Solid State NMR Spectroscopy: Application to the Observation of Proximities between Protons and Quadrupolar Nuclei, J. Phys. Chem. A. 113 (2009) 12864–12878. https://doi.org/10.1021/jp906099k.

[28] M. Shen, J. Trébosc, O. Lafon, Z. Gan, F. Pourpoint, B. Hu, Q. Chen, J.-P. Amoureux, Solid-state NMR indirect detection of nuclei experiencing large anisotropic interactions using spinning sideband-selective pulses, Solid State Nuclear Magnetic Resonance. 72 (2015) 104–117. https://doi.org/10.1016/j.ssnmr.2015.09.003.

[29] M. Shen, J. Trébosc, L.A. O'Dell, O. Lafon, F. Pourpoint, B. Hu, Q. Chen, J.-P. Amoureux, Comparison of various NMR methods for the indirect detection of nitrogen-14 nuclei via protons in solids, Journal of Magnetic Resonance. 258 (2015) 86–95. https://doi.org/10.1016/j.jmr.2015.06.008.

[30] A.G.M. Rankin, J. Trébosc, P. Paluch, O. Lafon, J.-P. Amoureux, Evaluation of excitation schemes for indirect detection of ^{14}N via solid-state HMQC NMR experiments, Journal of Magnetic Resonance. 303 (2019) 28–41. https://doi.org/10.1016/j.jmr.2019.04.004.

[31] V. Vitzthum, M.A. Caporini, S. Ulzega, G. Bodenhausen, Broadband excitation and indirect detection of nitrogen-14 in rotating solids using Delays Alternating with Nutation (DANTE)., Journal of Magnetic Resonance (San Diego, Calif. : 1997). 212 (2011) 234–239. https://doi.org/10.1016/j.jmr.2011.06.013.

[32] Y. Li, J. Trébosc, B. Hu, M. Shen, J.-P. Amoureux, O. Lafon, Indirect detection of broad spectra in solid-state NMR using interleaved DANTE trains, Journal of Magnetic Resonance. 294 (2018) 101–114. https://doi.org/10.1016/j.jmr.2018.07.005.

[33] A.J. Pell, K.J. Sanders, S. Wegner, G. Pintacuda, C.P. Grey, Low-power broadband solid-state MAS NMR of ^{14}N, The Journal of Chemical Physics. 146 (2017) 194202. https://doi.org/10.1063/1.4983220.

[34] R. Aleksis, A.J. Pell, Low-power synchronous helical pulse sequences for large anisotropic interactions in MAS NMR: Double-quantum excitation of 14N, J. Chem. Phys. 153 (2020) 244202. https://doi.org/10.1063/5.0030604.

[35] Y. Nishiyama, M. Malon, Z. Gan, Y. Endo, T. Nemoto, Proton – nitrogen-14 overtone two-dimensional correlation NMR spectroscopy of solid-sample at very fast magic angle sample spinning, Journal of Magnetic Resonance. 230 (2013) 160–164. https://doi.org/10.1016/j.jmr.2013.02.015.

[36] L.A. O'Dell, R. He, J. Pandohee, Identifying H–N proximities in solid-state NMR using 14N overtone irradiation under fast MAS, CrystEngComm. 15 (2013) 8657–8667. https://doi.org/10.1039/C3CE40967H.

[37] M. Shen, Q. Chen, J.-P. Amoureux, B. Hu, Broad-band excitation in indirectly detected ^{14}N overtone spectroscopy with composite pulses, Solid State Nuclear Magnetic Resonance. 78 (2016) 5–8. https://doi.org/10.1016/j.ssnmr.2016.05.001.

[38] R. Tycko, S.J. Opella, High-resolution nitrogen-14 overtone spectroscopy: an approach to natural abundance nitrogen NMR of oriented and polycrystalline systems, J. Am. Chem. Soc. 108 (1986) 3531–3532. https://doi.org/10.1021/ja00272a071.

[39] M. Shen, S. Wegner, J. Trébosc, B. Hu, O. Lafon, J.P. Amoureux, Minimizing the t_1-noise when using an indirect ^{1}H high-resolution detection of unlabeled samples, Solid State Nuclear Magnetic Resonance. 87 (2017) 111–116. https://doi.org/10.1016/j.ssnmr.2017.06.008.

[40] A. Venkatesh, X. Luan, F.A. Perras, I. Hung, W. Huang, A.J. Rossini, t_1-Noise eliminated dipolar heteronuclear multiple-quantum coherence solid-state NMR spectroscopy, Phys. Chem. Chem. Phys. 22 (2020) 20815–20828. https://doi.org/10.1039/D0CP03511D.

[41] F.A. Perras, M. Pruski, Reducing t_1 noise through rapid scanning, Journal of Magnetic Resonance. 298 (2019) 31–34. https://doi.org/10.1016/j.jmr.2018.11.008.

[42] Z. Gan, Measuring multiple carbon-nitrogen distances in natural abundant solids using R-RESPDOR NMR., Chemical Communications (Cambridge, England). (2006) 4712–4714. https://doi.org/10.1039/b611447d.

[43] L. Chen, Q. Wang, B. Hu, O. Lafon, J. Trébosc, F. Deng, J.-P. Amoureux, Measurement of hetero-nuclear distances using a symmetry-based pulse sequence in solid-state NMR., Physical Chemistry Chemical Physics. 12 (2010) 9395–9405. https://doi.org/10.1039/b926546e.

[44] X. Lu, O. Lafon, J. Trébosc, J.-P. Amoureux, Detailed analysis of the S-RESPDOR solid-state NMR method for inter-nuclear distance measurement between spin-1/2 and quadrupolar nuclei., Journal of Magnetic Resonance. 215 (2012) 34–49. https://doi.org/10.1016/j.jmr.2011.12.009.

[45] N.T. Duong, Z. Gan, Y. Nishiyama, Selective ^{1}H-^{14}N Distance Measurements by ^{14}N Overtone Solid-State NMR Spectroscopy at Fast MAS, Front. Mol. Biosci. 8 (2021). https://doi.org/10.3389/fmolb.2021.645347.

[46] B.A. Atterberry, S.L. Carnhahan, Y. Chen, A. Venkatesh, A.J. Rossini, Double Echo Symmetry-Based REDOR and RESPDOR Pulse Sequences for the Improved Proton Detected Measurement of Heteronuclear Dipolar Coupling Constants, (2021). https://doi.org/10.5281/zenodo.5745945.

[47] H. Nagashima, A.S. Lilly Thankamony, J. Trébosc, F. Pourpoint, O. Lafon, J.P. Amoureux, γ-Independent through-space hetero-nuclear correlation between spin-1/2 and quadrupolar nuclei in solids, Solid State Nuclear Magnetic Resonance. 84 (2017) 216–226. https://doi.org/10.1016/j.ssnmr.2017.06.002.

[48] J.A. Jarvis, I.M. Haies, P.T.F. Williamson, M. Carravetta, An efficient NMR method for the characterisation of ^{14}N sites through indirect ^{13}C detection., Physical Chemistry Chemical Physics : PCCP. 15 (2013) 7613–7620. https://doi.org/10.1039/c3cp50787d.

[49] J.A. Jarvis, I. Haies, M. Lelli, A.J. Rossini, I. Kuprov, M. Carravetta, P.T.F. Williamson, Measurement of ^{14}N quadrupole couplings in biomolecular solids using indirect-detection ^{14}N solid-state NMR with DNP, Chem. Commun. 53 (2017) 12116–12119. https://doi.org/10.1039/C7CC03462H.

[50] J.A. Jarvis, M. Concistre, I.M. Haies, R.W. Bounds, I. Kuprov, M. Carravetta, P.T.F. Williamson, Quantitative analysis of ^{14}N quadrupolar coupling using ^{1}H detected ^{14}N solid-state NMR, Phys. Chem. Chem. Phys. 21 (2019) 5941–5949. https://doi.org/10.1039/C8CP06276E.

[51] I. Hung, P. Gor'kov, Z. Gan, Efficient and sideband-free ^{1}H-detected ^{14}N magic-angle spinning NMR, J. Chem. Phys. 151 (2019) 154202. https://doi.org/10.1063/1.5126599.

[52] E.R.H. van Eck, R. Janssen, W.E.J.R. Maas, W.S. Veeman, A novel application of nuclear spin-echo double-resonance to aluminophosphates and aluminosilicates, Chemical Physics Letters. 174 (1990) 428–432. https://doi.org/10.1016/S0009-2614(90)87174-P.

[53] C.P. Grey, W.S. Veeman, The detection of weak heteronuclear coupling between spin 1 and spin 1/2 nuclei in MAS NMR; ^{14}N/^{13}C/^{1}H triple resonance experiments, Chemical Physics Letters. 192 (1992) 379–385. https://doi.org/10.1016/0009-2614(92)85486-T.

[54] C.P. Grey, A.J. Vega, Determination of the Quadrupole Coupling Constant of the Invisible Aluminum Spins in Zeolite HY with ^{1}H-^{27}Al TRAPDOR NMR, J. Am. Chem. Soc. 117 (1995) 8232–8242.

[55] D. Carnevale, X. Ji, G. Bodenhausen, Double cross polarization for the indirect detection of nitrogen-14 nuclei in magic angle spinning NMR spectroscopy, J. Chem. Phys. 147 (2017) 184201. https://doi.org/10.1063/1.5000689.

[56] S.V. Sajith, S. Jayanthi, A. Lupulescu, Effective Hamiltonian and ^{1}H-^{14}N cross polarization/double cross polarization at fast MAS, Journal of Magnetic Resonance. 320 (2020) 106832. https://doi.org/10.1016/j.jmr.2020.106832.

[57] J. Trebosc, B. Hu, J.P. Amoureux, Z. Gan, Through-space R^3-HETCOR experiments between spin-1/2 and half-integer quadrupolar nuclei in solid-state NMR, Journal of Magnetic Resonance. 186 (2007) 220–227. https://doi.org/10.1016/j.jmr.2007.02.015.

[58] A. Wong, D. Laurencin, R. Dupree, M.E. Smith, Two-dimensional ^{43}Ca–^{1}H correlation solid-state NMR spectroscopy, Solid State Nuclear Magnetic Resonance. 35 (2009) 32–36. https://doi.org/10.1016/j.ssnmr.2008.11.002.

[59] A.J. Rossini, M.P. Hanrahan, M. Thuo, Rapid acquisition of wideline MAS solid-state NMR spectra with fast MAS, proton detection, and dipolar HMQC pulse sequences, Phys. Chem. Chem. Phys. 18 (2016) 25284–25295. https://doi.org/10.1039/C6CP04279A.

[60] M.K. Pandey, H. Kato, Y. Ishii, Y. Nishiyama, Two-dimensional proton-detected ^{35}Cl/^{1}H correlation solid-state NMR experiment under fast magic angle sample spinning: application to pharmaceutical compounds, Phys. Chem. Chem. Phys. 18 (2016) 6209–6216. https://doi.org/10.1039/C5CP06042G.

[61] A. Venkatesh, M.P. Hanrahan, A.J. Rossini, Proton detection of MAS solid-state NMR spectra of half-integer quadrupolar nuclei, Solid State Nuclear Magnetic Resonance. 84 (2017) 171–181. https://doi.org/10.1016/j.ssnmr.2017.03.005.

[62] I. Hung, Z. Gan, High-Resolution NMR of S = 3/2 Quadrupole Nuclei by Detection of Double-Quantum Satellite Transitions via Protons, J. Phys. Chem. Lett. (2020) 4734–4740. https://doi.org/10.1021/acs.jpclett.0c01236.

[63] Z. Gan, Isotropic NMR Spectra of Half-Integer Quadrupolar Nuclei Using Satellite Transitions and Magic-Angle Spinning, J. Am. Chem. Soc. 122 (2000) 3242–3243. https://doi.org/10.1021/ja9939791.

[64] C. Huguenard, F. Taulelle, B. Knott, Z. Gan, Optimizing STMAS, Journal of Magnetic Resonance. 156 (2002) 131–137. https://doi.org/10.1006/jmre.2002.2548.

[65] S.E. Ashbrook, S. Wimperis, Satellite-Transition MAS NMR of Spin I=3/2, 5/2, 7/2, and 9/2 Nuclei: Sensitivity, Resolution, and Practical Implementation, Journal of Magnetic Resonance. 156 (2002) 269–281. https://doi.org/10.1006/jmre.2002.2557.

[66] J.-P. Amoureux, C. Huguenard, F. Engelke, F. Taulelle, Unified representation of MQMAS and STMAS NMR of half-integer quadrupolar nuclei, Chemical Physics Letters. 356 (2002) 497–504. https://doi.org/10.1016/S0009-2614(02)00398-6.

[67] F.A. Perras, A. Venkatesh, M.P. Hanrahan, T.W. Goh, W. Huang, A.J. Rossini, M. Pruski, Indirect detection of infinite-speed MAS solid-state NMR spectra, Journal of Magnetic Resonance. 276 (2017) 95–102. https://doi.org/10.1016/j.jmr.2017.01.010.

[68] P. Paluch, A.G.M. Rankin, J. Trébosc, O. Lafon, J.-P. Amoureux, Analysis of HMQC experiments applied to a spin ½ nucleus subject to very large CSA, Solid State Nuclear Magnetic Resonance. 100 (2019) 11–25. https://doi.org/10.1016/j.ssnmr.2019.03.001.

[69] A. Venkatesh, A. Lund, L. Rochlitz, R. Jabbour, C.P. Gordon, G. Menzildjian, J. Viger-Gravel, P. Berruyer, D. Gajan, C. Copéret, A. Lesage, A.J. Rossini, The Structure of Molecular and Surface Platinum Sites Determined by DNP-SENS and Fast MAS 195Pt Solid-State NMR Spectroscopy, J. Am. Chem. Soc. 142 (2020) 18936–18945. https://doi.org/10.1021/jacs.0c09101.

[70] A. Venkatesh, F.A. Perras, A.J. Rossini, Proton-detected solid-state NMR spectroscopy of spin-1/2 nuclei with large chemical shift anisotropy, Journal of Magnetic Resonance. 327 (2021) 106983. https://doi.org/10.1016/j.jmr.2021.106983.

[71] B.E.G. Lucier, K.E. Johnston, W. Xu, J.C. Hanson, S.D. Senanayake, S. Yao, M.W. Bourassa, M. Srebro, J. Autschbach, R.W. Schurko, Unravelling the Structure of Magnus ’ Pink Salt, J. Am. Chem. Soc. 136 (2014) 1333–1351.

[72] X. Lu, O. Lafon, J. Trébosc, G. Tricot, L. Delevoye, F. Méar, L. Montagne, J.P. Amoureux, Observation of proximities between spin-1/2 and quadrupolar nuclei: which heteronuclear dipolar recoupling method is preferable?, The Journal of Chemical Physics. 137 (2012) 144201. https://doi.org/10.1063/1.4753987.

[73] P. Caravatti, G. Bodenhausen, R.R. Ernst, Selective Pulse Experiments in High-Resolution Solid State NMR, J. Magn. Reson. 55 (1983) 88–103.

[74] A. Brinkmann, M.H. Levitt, Symmetry principles in the nuclear magnetic resonance of spinning solids: Heteronuclear recoupling by generalized Hartmann-Hahn sequences, J. Chem. Phys. 115 (2001) 357–384.

[75] A.J. Pell, G. Kervern, L. Emsley, M. Deschamps, D. Massiot, P.J. Grandinetti, G. Pintacuda, Broadband inversion for MAS NMR with single-sideband-selective adiabatic pulses., The Journal of Chemical Physics. 134 (2011) 024117. https://doi.org/10.1063/1.3521491.

[76] F. Bloch, A. Siegert, Magnetic Resonance for Nonrotating Fields, Phys. Rev. 57 (1940) 522–527. https://doi.org/10.1103/PhysRev.57.522.

[77] M. Leskes, P.K. Madhu, S. Vega, Floquet theory in solid-state nuclear magnetic resonance., Progress in Nuclear Magnetic Resonance Spectroscopy. 57 (2010) 345–80. https://doi.org/10.1016/j.pnmrs.2010.06.002.

[78] M.H. Levitt, Why do spinning sidebands have the same phase?, Journal of Magnetic Resonance (1969). 82 (1989) 427–433. https://doi.org/10.1016/0022-2364(89)90050-4.

[79] A. Jerschow, From nuclear structure to the quadrupolar NMR interaction and high-resolution spectroscopy, Progress in Nuclear Magnetic Resonance Spectroscopy. 46 (2005) 63–78. https://doi.org/10.1016/j.pnmrs.2004.12.001.

[80] H. Kao, C. Grey, INEPT experiments involving quadrupolar nuclei in solids, Journal of Magnetic Resonance (San Diego, Calif. : 1997). 133 (1998) 313–23. https://doi.org/10.1006/jmre.1998.1455.

[81] N. Müller, G. Bodenhausen, R.R. Ernst, Relaxation-induced violations of coherence transfer selection rules in nuclear magnetic resonance, Journal of Magnetic Resonance (1969). 75 (1987) 297–334. https://doi.org/10.1016/0022-2364(87)90038-2.

[82] M. Bak, J.T. Rasmussen, N.C. Nielsen, SIMPSON: a general simulation program for solid-state NMR spectroscopy., Journal of Magnetic Resonance. 147 (2000) 296–330. https://doi.org/10.1006/jmre.2000.2179.

[83] M. Bak, N.Chr. Nielsen, REPULSION, A Novel Approach to Efficient Powder Averaging in Solid-State NMR, Journal of Magnetic Resonance (San Diego, Calif. : 1997). 125 (1997) 132–139.

[84] S.R. Rabbani, D.T. Edmonds, P. Gosling, M.H. Palmer, Measurement of the ^{14}N quadrupole coupling constants in glycine, diglycine, triglycine, and tetraglycine and a comparison with calculation, Journal of Magnetic Resonance (1969). 72 (1987) 230–237. https://doi.org/10.1016/0022-2364(87)90285-X.

[85] R.E. Stark, R.A. Haberkorn, R.G. Griffin, ^{14}N NMR determination of NH bond lengths in solids, J. Chem. Phys. 68 (1978) 1996–1997. https://doi.org/10.1063/1.435879.

[86] K. Mao, J.W. Wiench, V.S.-Y. Lin, M. Pruski, Indirectly detected through-bond chemical shift correlation NMR spectroscopy in solids under fast MAS: Studies of organic–inorganic hybrid materials, Journal of Magnetic Resonance. 196 (2009) 92–95. https://doi.org/10.1016/j.jmr.2008.10.010.

[87] R.K. Harris, E.D. Becker, S.M. Cabral de Menezes, R. Goodfellow, P. Granger, NMR nomenclature . Nuclear spin properties and conventions for chemical shifts, Pure and Applied Chemistry. 73 (2001) 1795–1818.

[88] A. Sasaki, J. Trébosc, J.-P. Amoureux, Accelerating the acquisition of high-resolution quadrupolar MQ/ST-HETCOR 2D spectra under fast MAS via 1H detection and through-space population transfers, Journal of Magnetic Resonance. 333 (2021) 107093. https://doi.org/10.1016/j.jmr.2021.107093.

[89] B.E.G. Lucier, A.R. Reidel, R.W. Schurko, Multinuclear solid-state NMR of square-planar platinum complexes — Cisplatin and related systems, Can. J. Chem. 89 (2011) 919–937. https://doi.org/10.1139/v11-033.

[90] M. Pons, M. Feliz, E. Giralt, Steady-State DQF-COSY Spectra Using a Variable Relaxation Delay, J. Magn. Reson. 78 (1988) 314–320.

[91] D. Marion, M. Ikura, R. Tschudin, A. Bax, Rapid recording of 2D NMR spectra without phase cycling. Application to the study of hydrogen exchange in proteins, Journal of Magnetic Resonance (1969). 85 (1989) 393–399. https://doi.org/10.1016/0022-2364(89)90152-2.

[92] D. Corinti, C. Coletti, N. Re, S. Piccirillo, M. Giampà, M.E. Crestoni, S. Fornarini, Hydrolysis of cis- and transplatin: structure and reactivity of the aqua complexes in a solvent free environment, RSC Adv. 7 (2017) 15877–15884. https://doi.org/10.1039/C7RA01182B.

[93] M.J. Hunt, A.L. Mackay, Deuterium and nitrogen pure quadrupole resonance in amino acids. II, Journal of Magnetic Resonance (1969). 22 (1976) 295–301. https://doi.org/10.1016/0022-2364(76)90304-8.

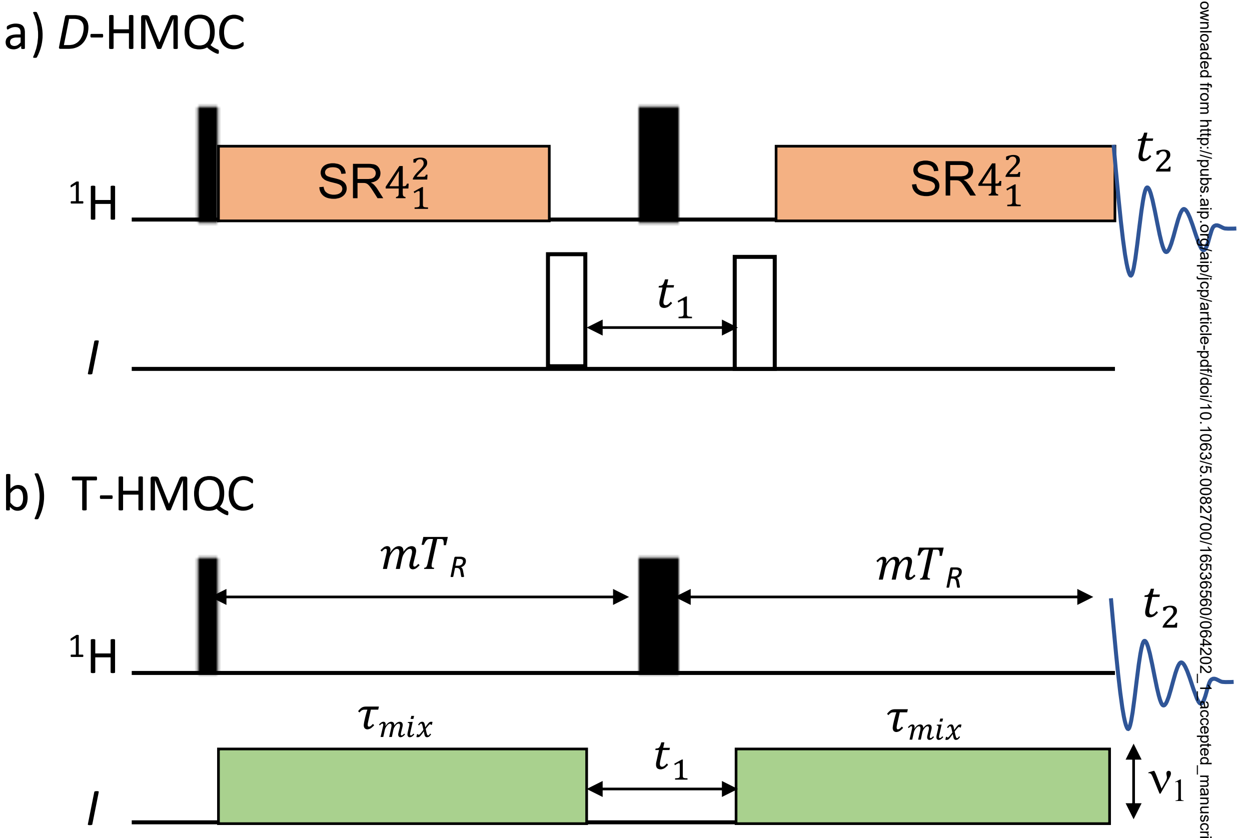

a) *D*-HMQC

b) T-HMQC

^{1}H
SR4_1^2
SR4_1^2
t_2
I
t_1
^{1}H
mT_R
mT_R
t_2
I
τ_{mix}
τ_{mix}
t_1
ν_1

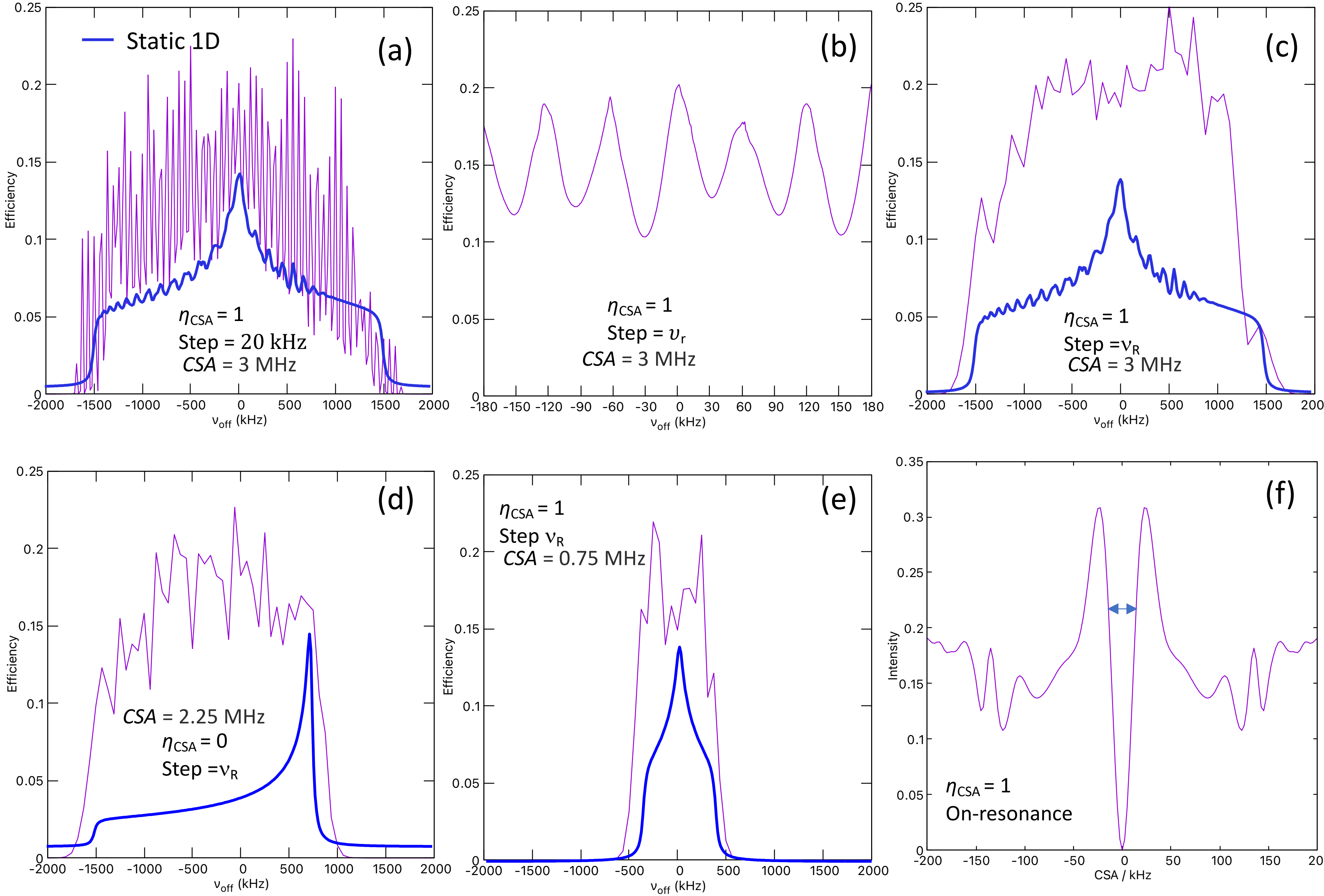
(a)
Static 1D
η_{CSA} = 1
Step = 20 kHz
CSA = 3 MHz
Efficiency
ν_{off} (kHz)
(b)
η_{CSA} = 1
Step = υ_r
CSA = 3 MHz
Efficiency
ν_{off} (kHz)
(c)
η_{CSA} = 1
Step = ν_R
CSA = 3 MHz
Efficiency
ν_{off} (kHz)
(d)
CSA = 2.25 MHz
η_{CSA} = 0
Step = ν_R
Efficiency
ν_{off} (kHz)
(e)
η_{CSA} = 1
Step ν_R
CSA = 0.75 MHz
Efficiency
ν_{off} (kHz)
(f)
η_{CSA} = 1
On-resonance
Intensity
CSA / kHz

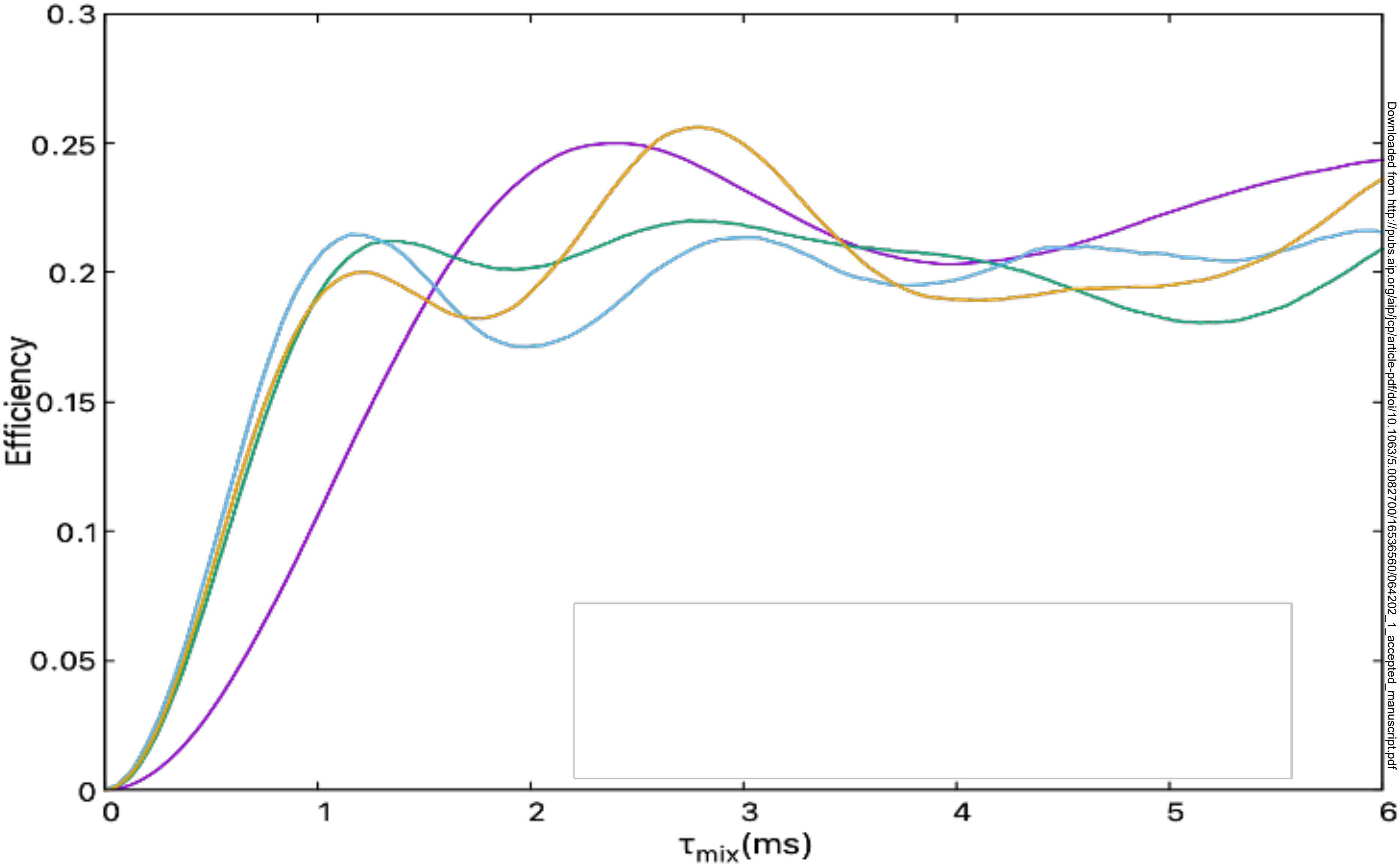
Efficiency
0.3
0.25
0.2
0.15
0.1
0.05
0
0
1
2
3
4
5
6
τ_{mix}(ms)

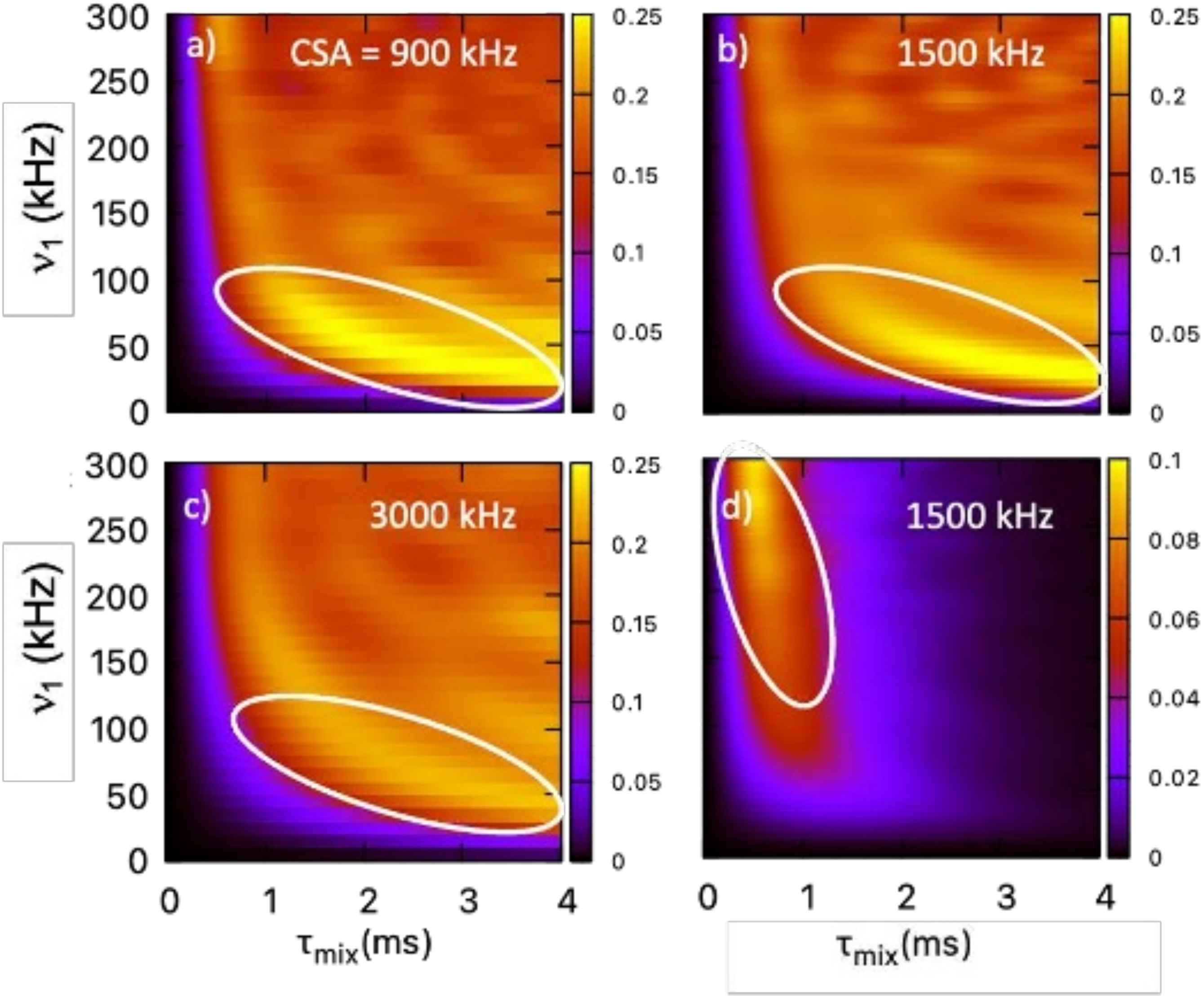
a)
CSA = 900 kHz
b)
1500 kHz
c)
3000 kHz
d)
1500 kHz
ν1 (kHz)
τmix(ms)
300
250
200
150
100
50
0
1
2
3
4
0.25
0.2
0.15
0.1
0.05
0.08
0.06
0.04
0.02

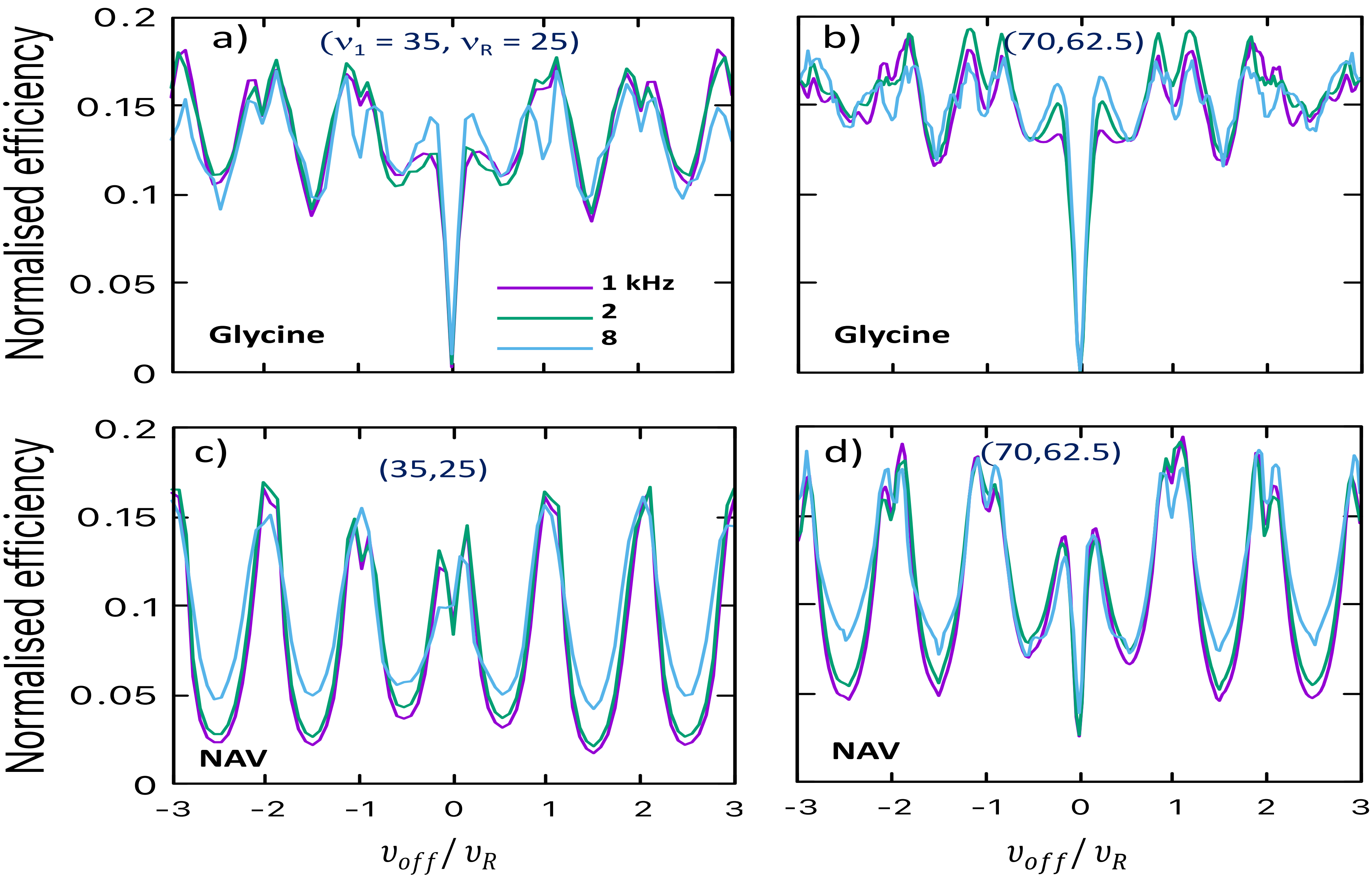
Normalised efficiency
0.2
0.15
0.1
0.05
0
a)
(ν_1 = 35, ν_R = 25)
1 kHz
2
8
Glycine
b)
(70,62.5)
Glycine
c)
(35,25)
NAV
d)
(70,62.5)
NAV
-3
-2
-1
0
1
2
3
$\upsilon_{off} / \upsilon_R$

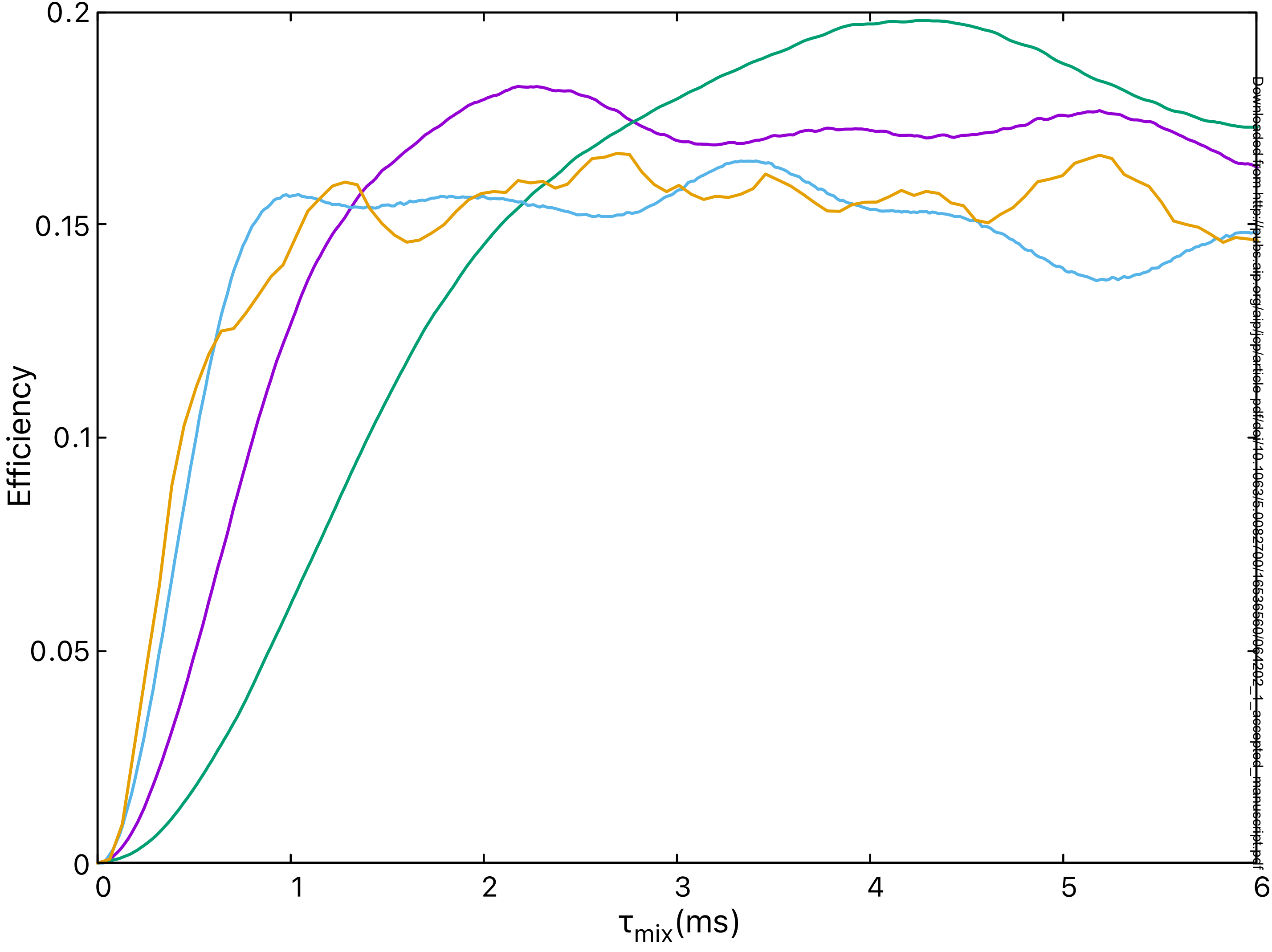
0.2
0.15
0.1
0.05
0
Efficiency
0
1
2
3
4
5
6
τ_{mix}(ms)

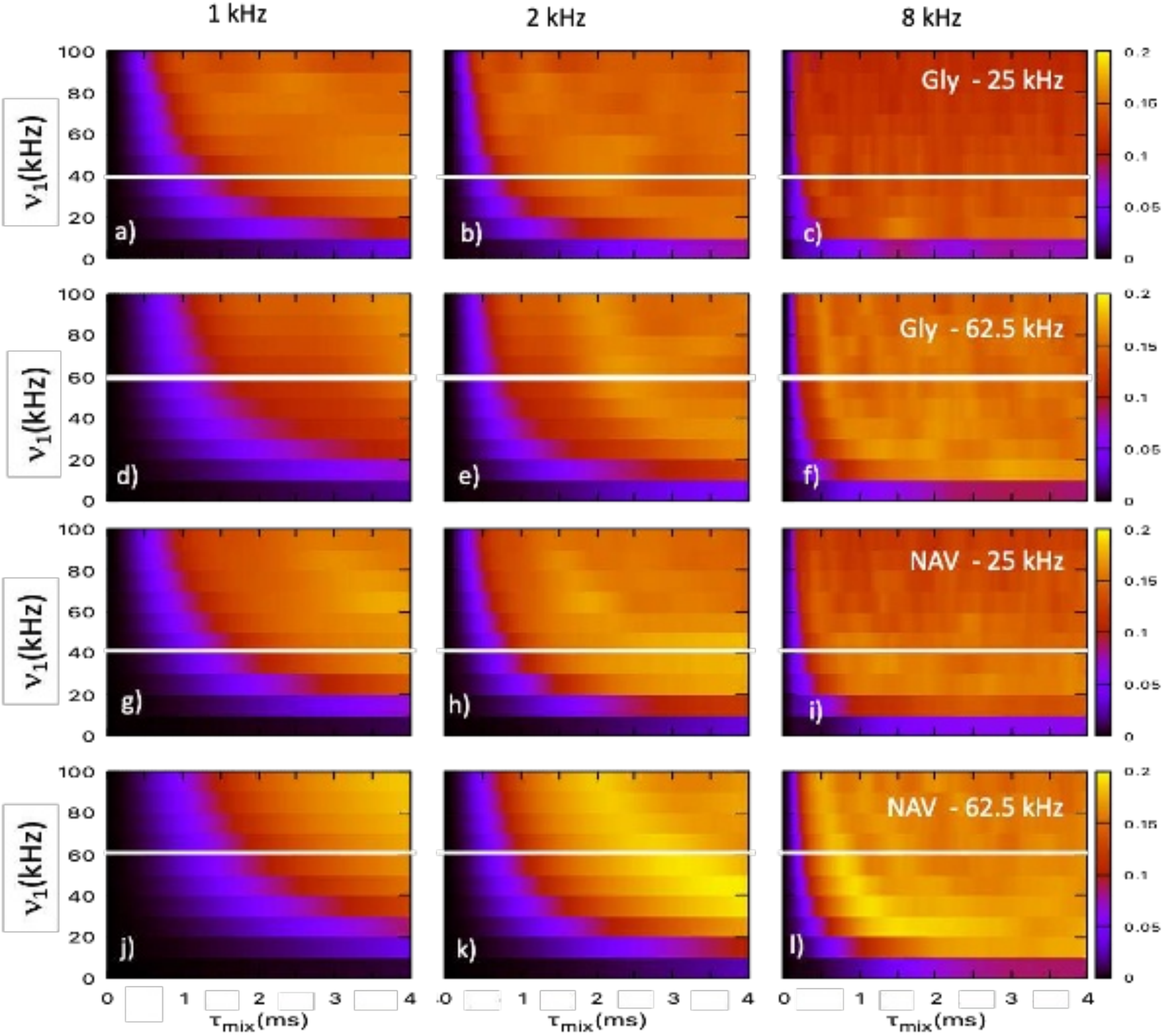
1 kHz
2 kHz
8 kHz
Gly - 25 kHz
Gly - 62.5 kHz
NAV - 25 kHz
NAV - 62.5 kHz
ν_1(kHz)
0
20
40
60
80
100
a)
b)
c)
d)
e)
f)
g)
h)
i)
j)
k)
l)
0
0.05
0.1
0.15
0.2
0
1
2
3
4
τ_{mix}(ms)

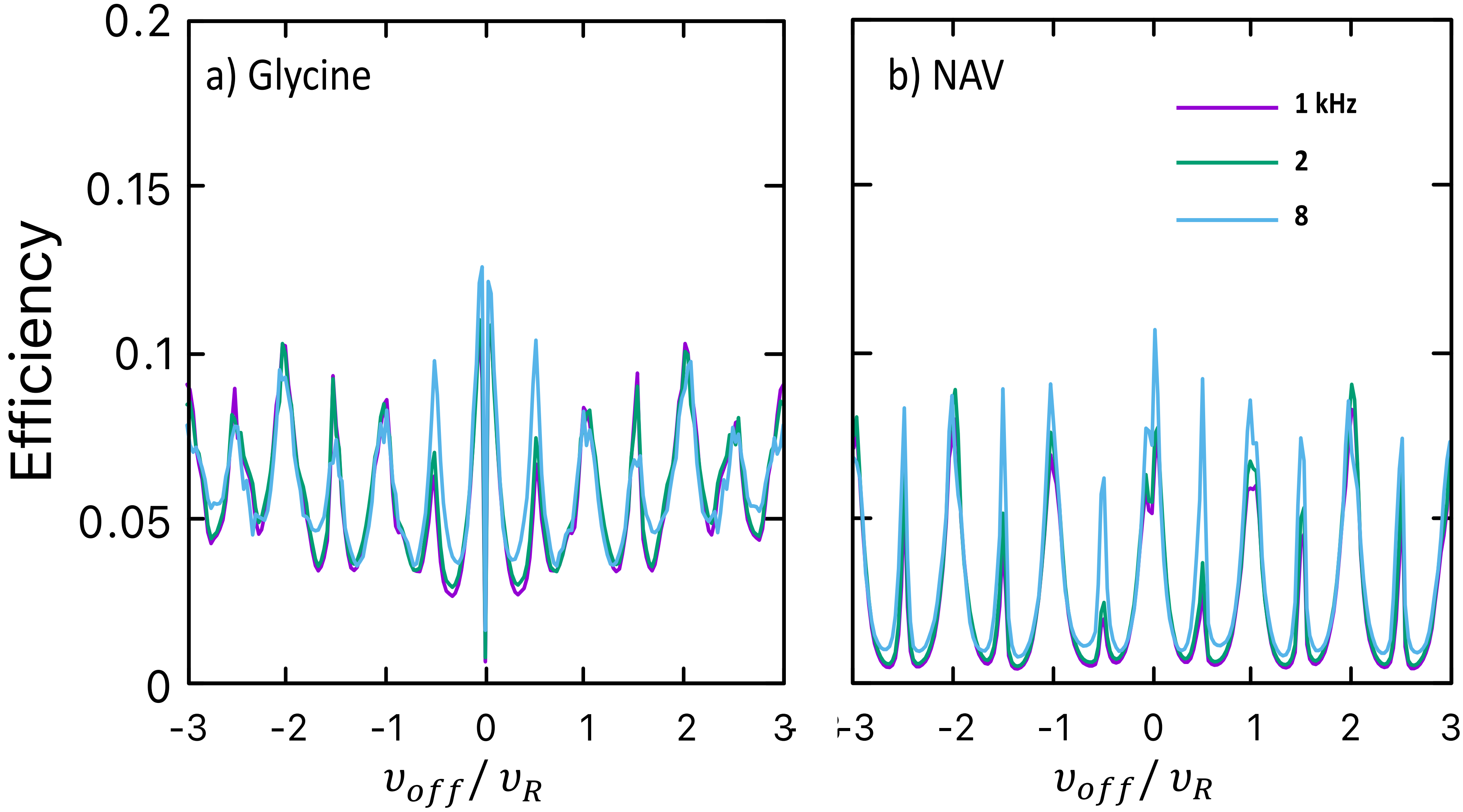
Efficiency
0.2
0.15
0.1
0.05
0
a) Glycine
b) NAV
1 kHz
2
8
-3
-2
-1
0
1
2
3
$\upsilon_{off} / \upsilon_R$

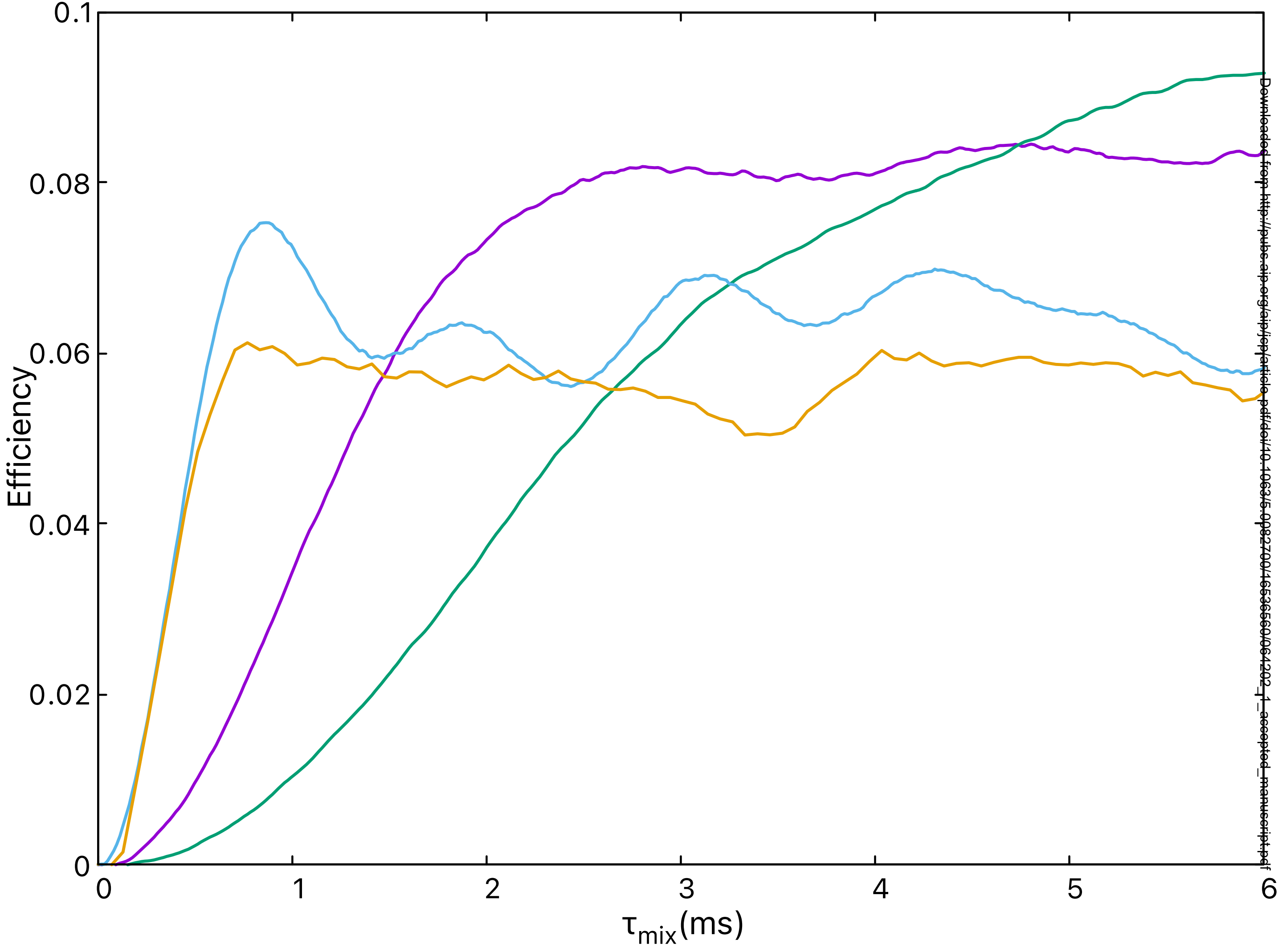
0.1
0.08
0.06
0.04
0.02
0
Efficiency
0
1
2
3
4
5
6
τ_{mix}(ms)

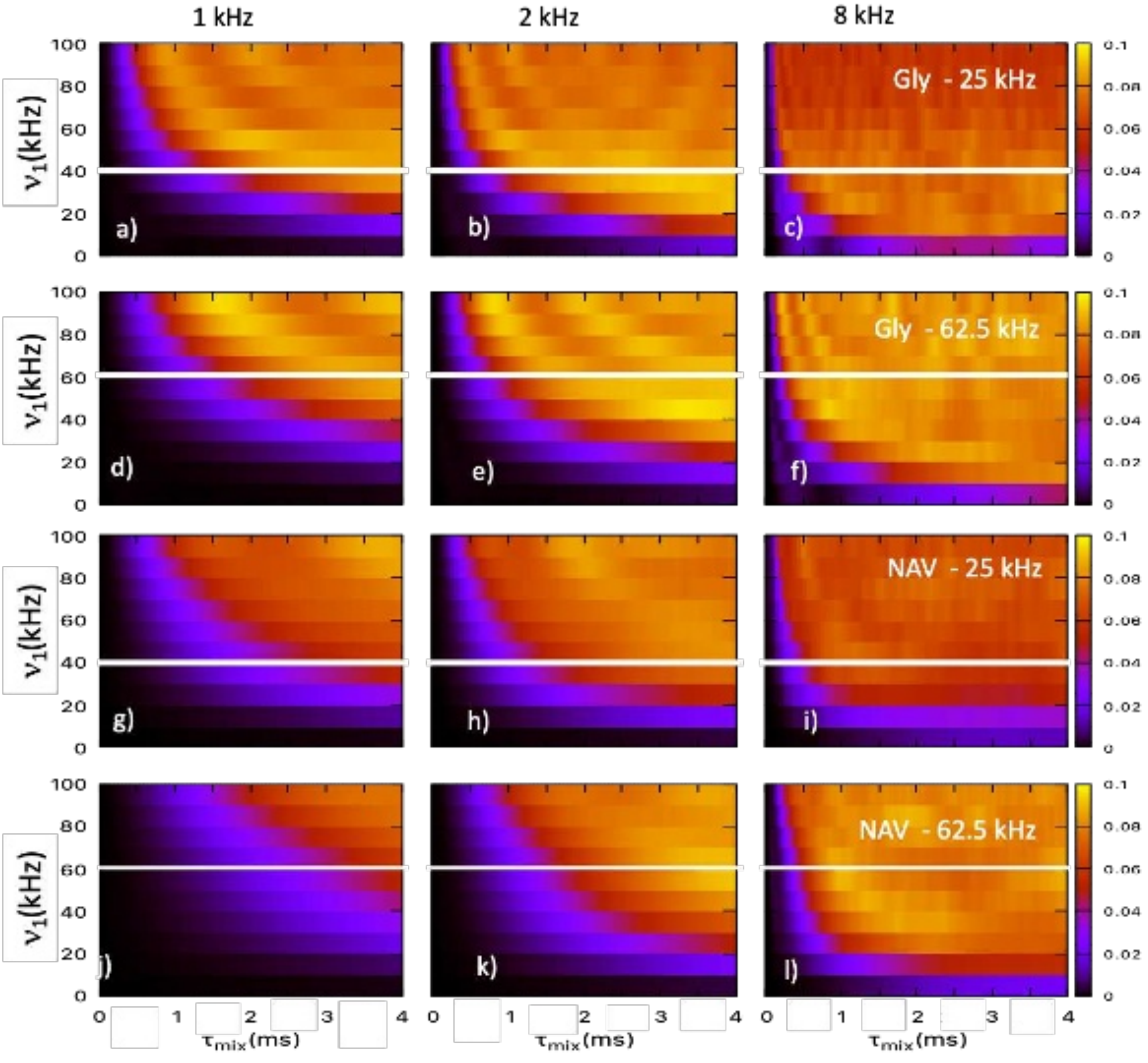
1 kHz
2 kHz
8 kHz
Gly - 25 kHz
Gly - 62.5 kHz
NAV - 25 kHz
NAV - 62.5 kHz
a)
b)
c)
d)
e)
f)
g)
h)
i)
j)
k)
l)
ν_1(kHz)
0
20
40
60
80
100
τ_{mix}(ms)
0
1
2
3
4
0
0.02
0.04
0.06
0.08
0.1

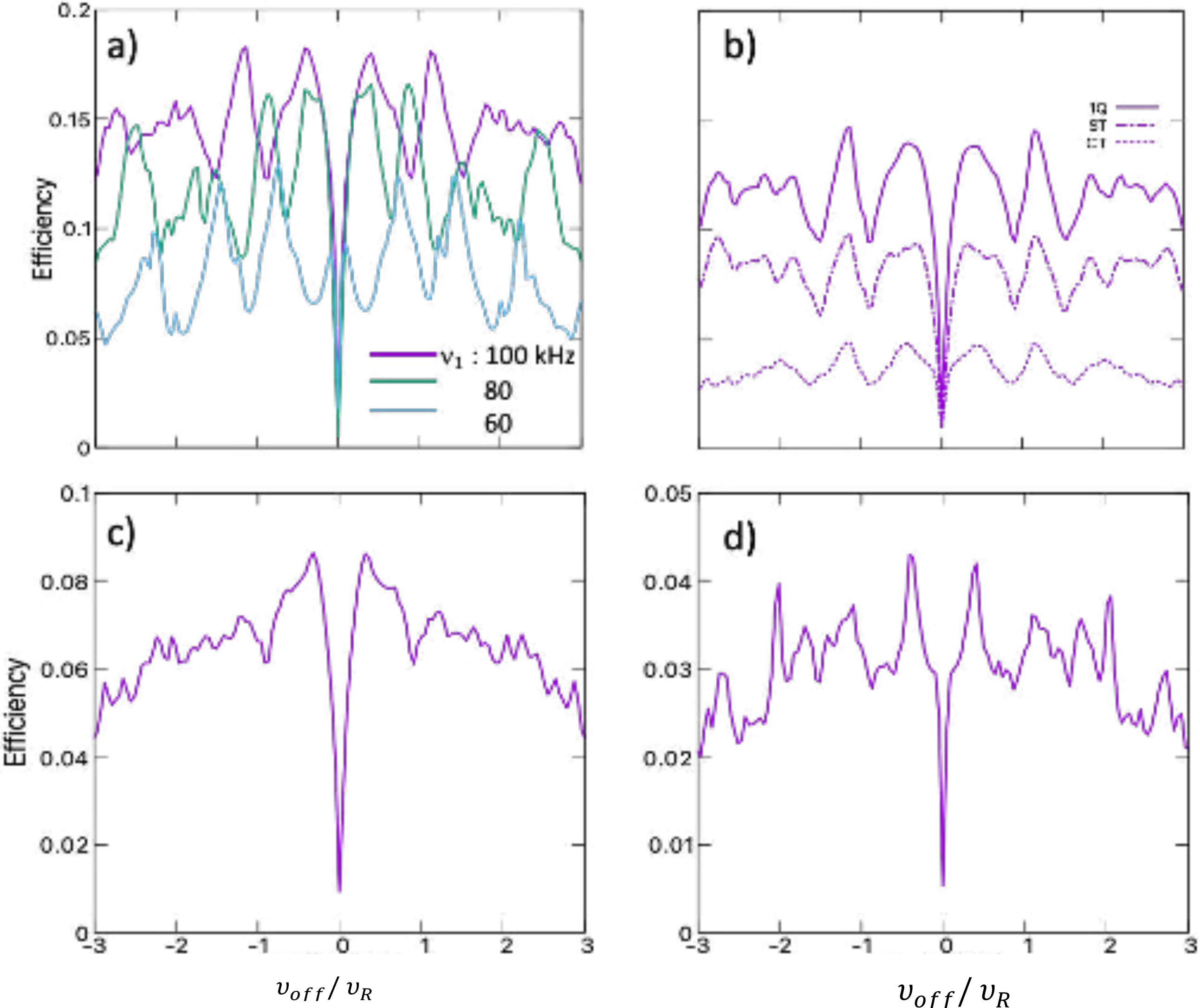
a)
b)
c)
d)
Efficiency
Efficiency
ν_1 : 100 kHz
80
60
1Q
ST
CT
0.2
0.15
0.1
0.05
0
0.1
0.08
0.06
0.04
0.02
0
0.05
0.04
0.03
0.02
0.01
0
-3
-2
-1
0
1
2
3
$\upsilon_{off} / \upsilon_R$
$\upsilon_{off} / \upsilon_R$

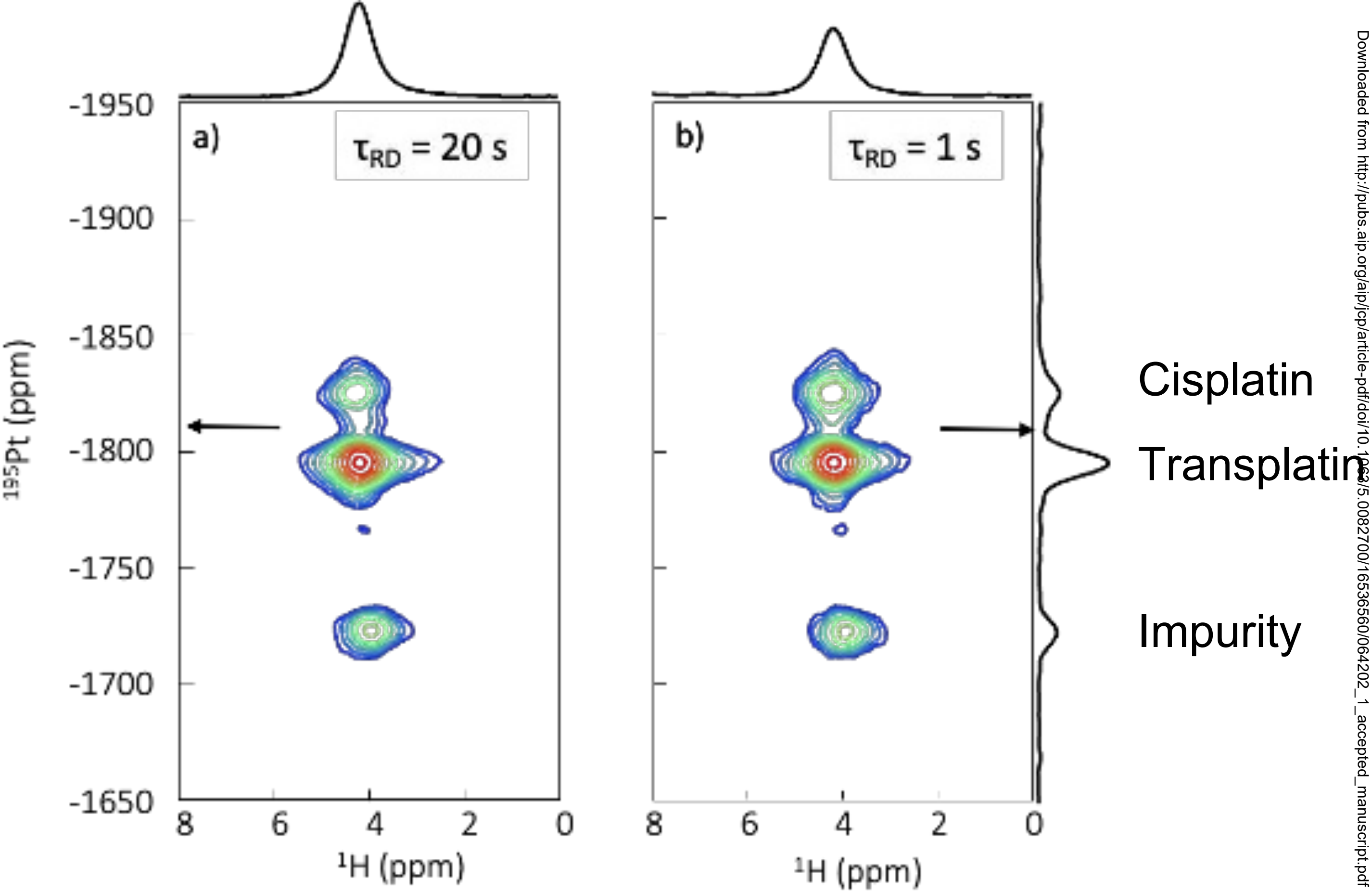

a)
τ_{RD} = 20 s
b)
τ_{RD} = 1 s
^{195}Pt (ppm)
-1950
-1900
-1850
-1800
-1750
-1700
-1650
^{1}H (ppm)
8
6
4
2
0
Cisplatin
Transplatin
Impurity

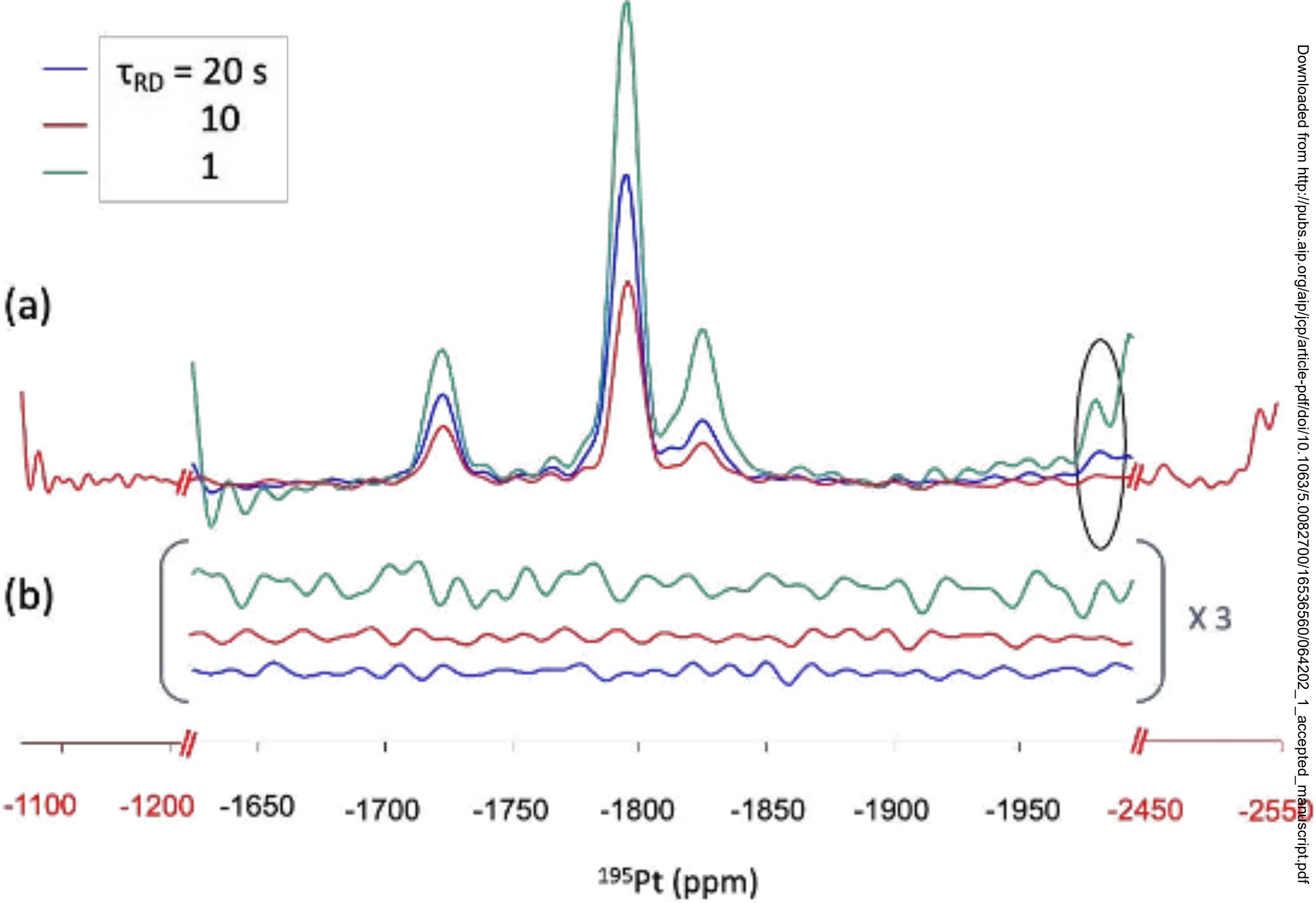
τRD = 20 s
10
1
(a)
(b)
X 3
-1100
-1200
-1650
-1700
-1750
-1800
-1850
-1900
-1950
-2450
-2550
195Pt (ppm)

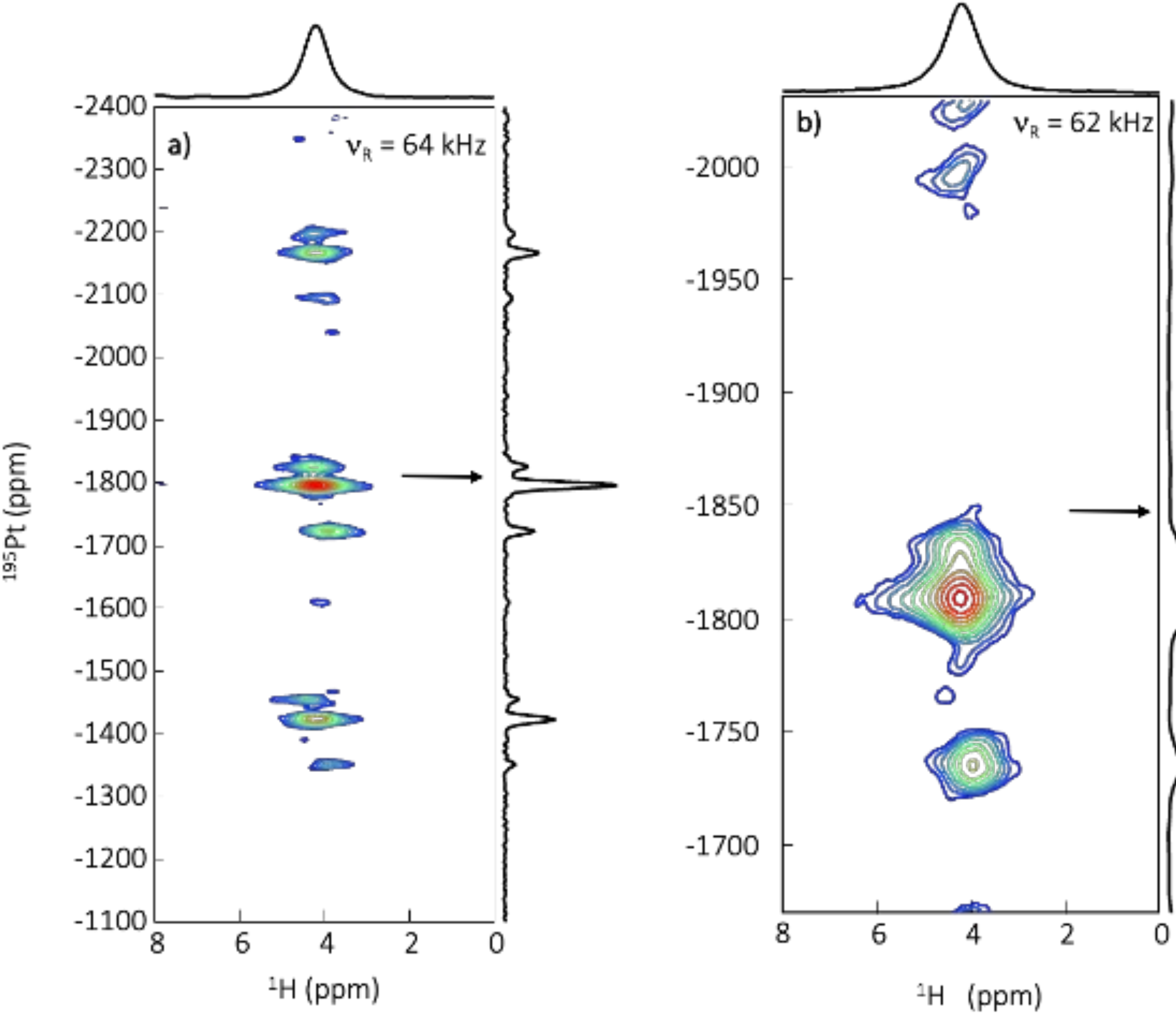
a)
ν_R = 64 kHz
-2400
-2300
-2200
-2100
-2000
-1900
-1800
-1700
-1600
-1500
-1400
-1300
-1200
-1100
^{195}Pt (ppm)
8
6
4
2
0
^{1}H (ppm)
b)
ν_R = 62 kHz
-2000
-1950
-1900
-1850
-1800
-1750
-1700
8
6
4
2
0
^{1}H (ppm)

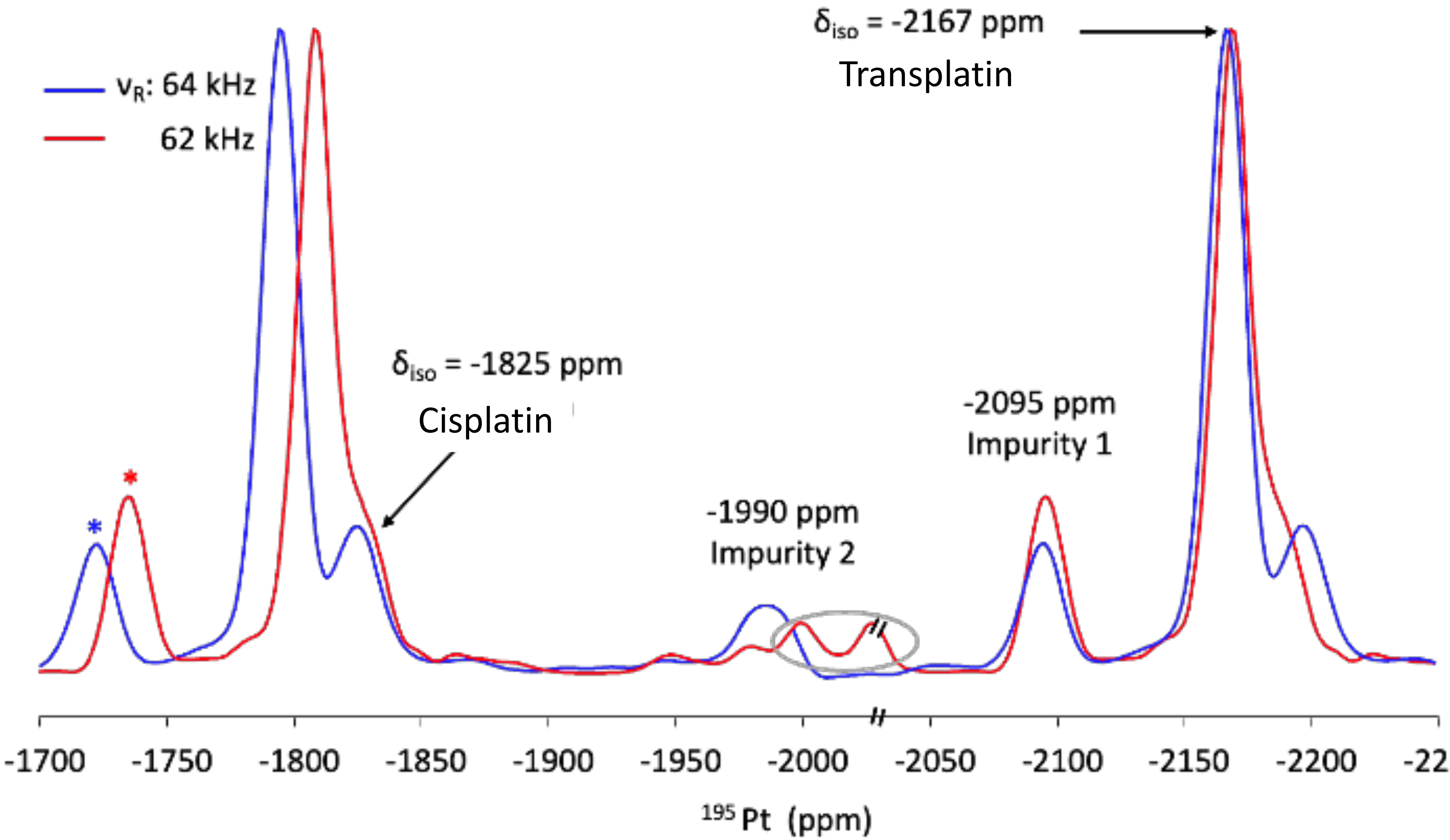

ν_R: 64 kHz
62 kHz
*
*
δ_{iso} = -1825 ppm
Cisplatin
-1990 ppm
Impurity 2
-2095 ppm
Impurity 1
δ_{iso} = -2167 ppm
Transplatin
//
//
-1700
-1750
-1800
-1850
-1900
-1950
-2000
-2050
-2100
-2150
-2200
-2250
^{195}Pt (ppm)

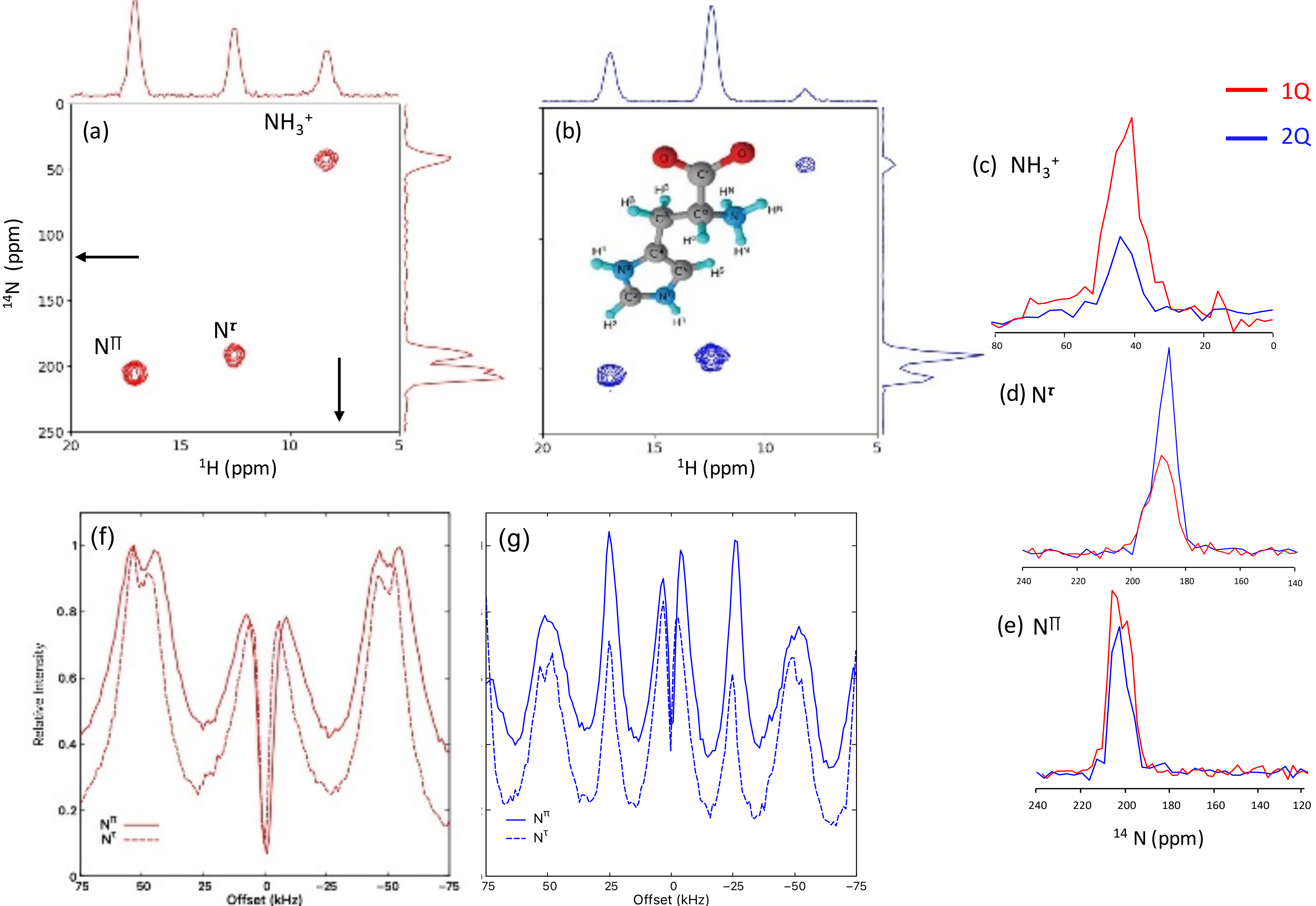
(a)
NH$_3^+$
N$^\pi$
N$^\tau$
^{14}N (ppm)
0
50
100
150
200
250
20
15
10
5
^{1}H (ppm)
(b)
^{1}H (ppm)
1Q
2Q
(c) NH$_3^+$
80
60
40
20
0
(d) N$^\tau$
240
220
200
180
160
140
(e) N$^\pi$
120
^{14} N (ppm)
(f)
Relative Intensity
1
0.8
0.6
0.4
0.2
0
75
50
25
0
-25
-50
-75
Offset (kHz)
N$^\pi$
N$^\tau$
(g)
N$^\pi$
N$^\tau$
Offset (kHz)

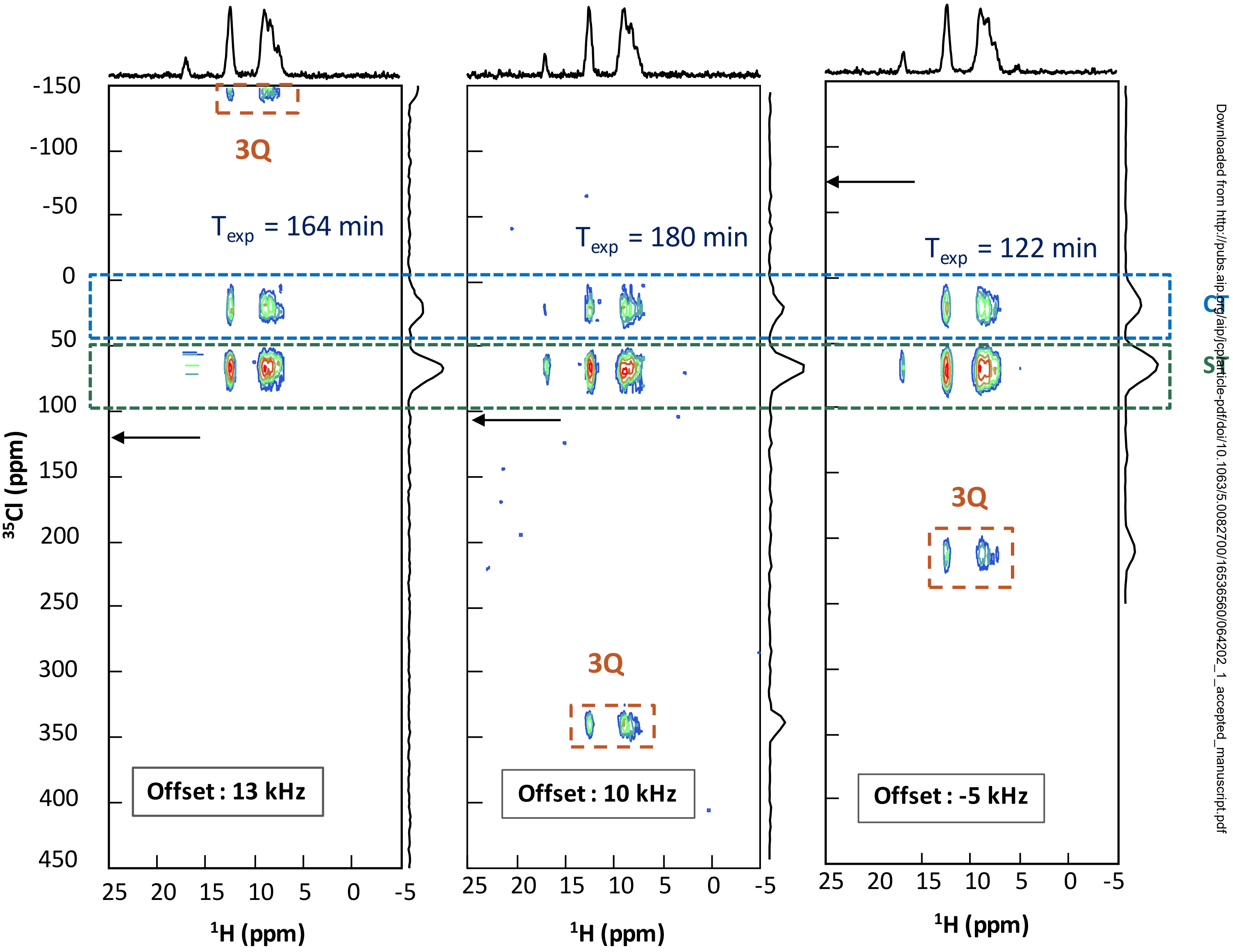

-150
-100
-50
0
50
100
150
200
250
300
350
400
450
^{35}Cl (ppm)
3Q
T_{exp} = 164 min
T_{exp} = 180 min
T_{exp} = 122 min
3Q
3Q
CT
ST
Offset : 13 kHz
Offset : 10 kHz
Offset : -5 kHz
25 20 15 10 5 0 -5
^{1}H (ppm)
25 20 15 10 5 0 -5
^{1}H (ppm)
25 20 15 10 5 0 -5
^{1}H (ppm)

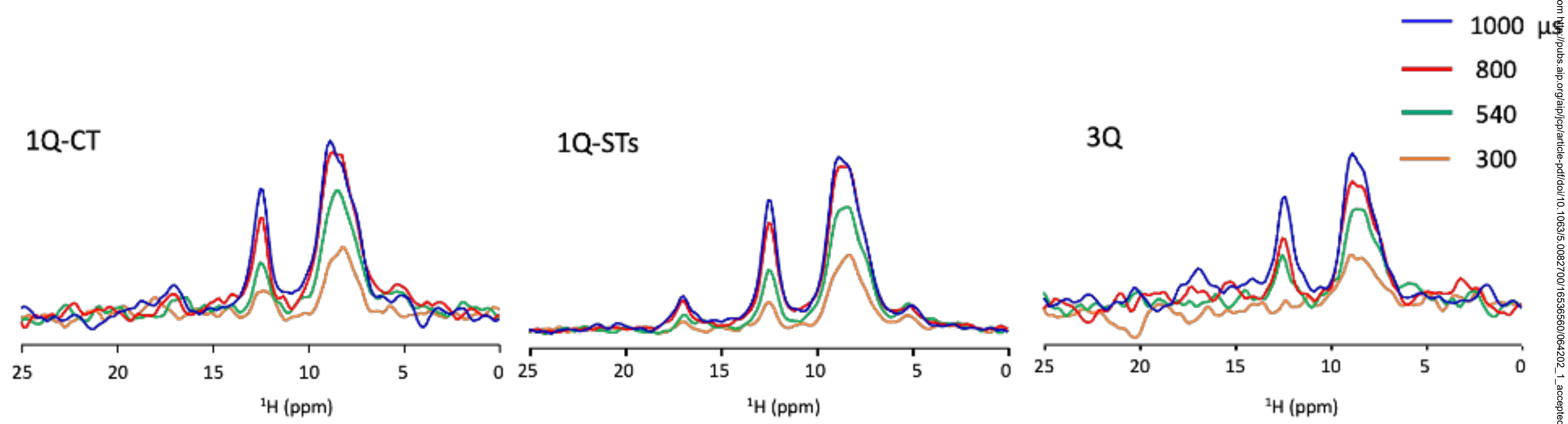
1Q-CT
1Q-STs
3Q
1000 μs
800
540
300
25
20
15
10
5
0
^{1}H (ppm)

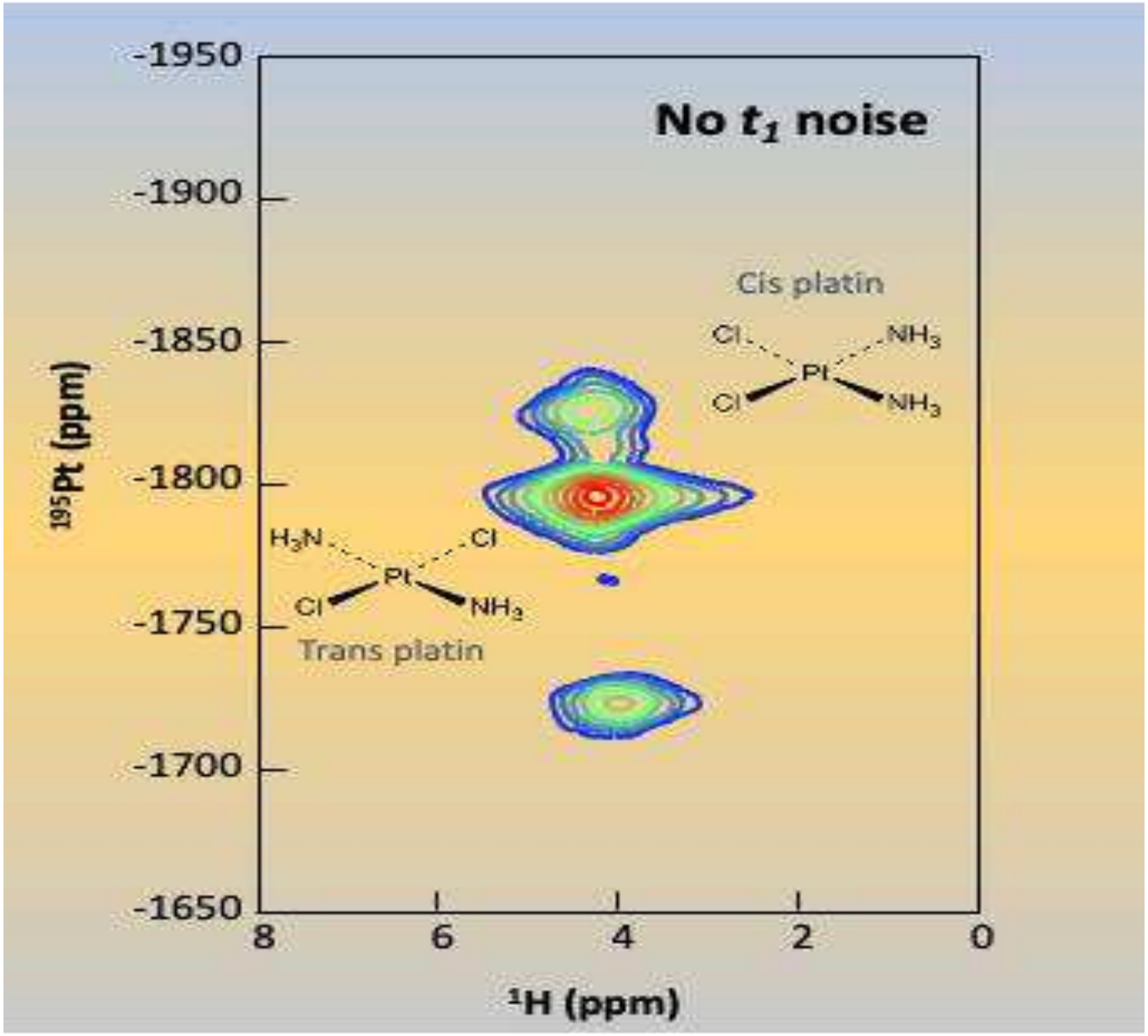

^{1}H-{^{195}Pt} *T*-HMQC 2D spectra of an aged mixture of trans- and cisplatin (18.8 T, 64 kHz MAS).